Comparative study of polar cap electron density measurements and E-CHAIM modeling

A Thesis Submitted to the College of
Graduate and Postdoctoral Studies in
Partial Fulfillment of the Requirements
for the Degree of Master of Science in the
Department of Physics and Engineering Physics
University of Saskatchewan
Saskatoon

By

Bion Larson

Permission to use

In presenting this thesis in partial fulfillment of the requirements for a Postgraduate degree from the University of Saskatchewan, I agree that the Libraries of this University may make it freely available for inspection. I further agree that permission for copying of this thesis in any manner, in whole or in part, for scholarly purposes may be granted by the professor or professors who supervised my thesis work or, in their absence, by the Head of the Department or the Dean of the College in which my thesis work was done. It is understood that any copying or publication or use of this thesis or parts thereof for financial gain shall not be allowed without my written permission. It is also understood that due recognition shall be given to me and to the University of Saskatchewan in any scholarly use which may be made of any material in my thesis.

Requests for permission to copy or to make other use of material in this thesis in whole or part should be addressed to:

Head of the Department of Physics and Engineering Physics
Physics Building
116 Science Place
University of Saskatchewan
Saskatoon, Saskatchewan S7N 5E2
Canada

Dean
College of Graduate and Postdoctoral Studies
University of Saskatchewan
116 Thorvaldson Building, 110 Science Place
Saskatoon, Saskatchewan S7N 5C9
Canada

Abstract

The electron density in the Earth's topside ionosphere has been studied with ground-based incoherent scatter radars (ISRs), Langmuir Probes (LP) placed on low-altitude satellites and many other instruments and techniques. These measurements have been continuously digested into statistical models of the electron density distribution. These models are used for forecasting of radio wave propagation in the ionosphere. The success of ionospheric models depends on the overall coverage by instruments and quality of their measurements. Joint observations with multiple instruments, however, have been rarely considered while it is important to assess whether they report consistently comparable values of the electron density. One example of a concern is an early suspicion in the LP experimentation in space that an underestimation effect can occur because of the contamination of the current-collecting surfaces.

This thesis addresses several aspects of the electron density measurements in the ionosphere with two instruments, ISRs and LP instruments onboard Swarm satellites, and modelling with the recently developed Empirical Canadian High Arctic Ionospheric Model (E-CHAIM). The study focuses on the Resolute Bay (Nunavut, Canada) area, located at extreme high latitudes where the ionosphere is very dynamic and poorly investigated.

The first objective of the work was to evaluate the consistency of LP instruments on the Swarm A and C satellites flying one after another at the same altitude with a time separation of 7-10 seconds and spatial separation of ~100 km. Occasional inconsistencies between the reported values were identified, and those were related to the occurrence of patches with enhanced electron density (polar cap patches). It was concluded that the polar cap patches are more frequent in the night sector, especially in summer and winter.

Secondly, the long-term trends in the electron density reported by the satellites at two flight heights of ~450 km (Swarm A and C) and ~510 km (Swarm B) were investigated. A strong solar cycle effect was identified, in agreement with predictions by the E-CHAIM model. Comparison of the model output with the Swarm data showed typically larger values, up to 30%.

To further assess the electron densities measured by the Swarm LP instruments, a point-by-point comparison with ISR measurements of the electron density was performed for about 200 conjunction points. It was shown that Swarm values are lower than those measured by the radars by ~35%, on average. The agreement between the satellite-radar data is better for the electron densities between 5×10^{10} m^{-3} and 40×10^{10} m^{-3}. The conclusion on the electron density underestimation for Swarm LP instruments is, overall, consistent with that reported for middle latitudes in the past, but the effect is much stronger at high latitudes. Moreover,

at high latitudes, the underestimation effect becomes progressively stronger as the electron density increases.

Finally, predictions of the E-CHAIM model electron densities over Resolute Bay were compared with measurements by the ISR radars with the goal of assessing the quality of model predictions at various heights. It was shown that for the middle part of the F layer, around its maximum, E-CHAIM shows reasonable agreement with measurements. The ratio of the predicted density to the observed density was mostly between 0.5 and 1.5, with 1.0 indicating perfect agreement. The best agreement was found in the summer. At the topside altitudes, the model was found to underestimate electron densities, particularly in the summer season. The worst agreement between the model and measurements was found for the ionospheric bottomside where the model often shows 2-3 times larger electron densities, especially in winter and spring.

At the end of the thesis, suggestions for future research have been outlined.

Acknowledgements

First, I would like to thank Dr. Alexander Koustov for offering me an opportunity to complete a Master's degree, as well as for his enormous effort supervising and guiding me through my project. Without his offer and guidance I would have not have been able to attempt or finish this degree. I would also like to thank Dr. Alexey Shevyakov and Dr. Artur Sowa in Math for convincing me to consider a Master's degree. Without their encouragement that I consider a Master's degree I likely would have turned Dr. Koustov's offer down.

For their invaluable suggestions and input on my paper in Chapter 4, I would like to thank Dr. Ashton Reimer, Dr. Gillies, Dr. Kouznetsov, and Dr. Lomidze. Extra thanks goes to Dr. Reimer for his assistance understanding RISR data and ensuring all the data were properly calibrated.

I would like to thank Dr. David Themens, the primary developer of E-CHAIM, for adding me as co-author to his paper, and, more importantly, for his interest in my work with E-CHAIM. Dr. Themens, Dr. Reimer and Dr. Knudsen all proved welcoming and encouraging at DASP 2019. Dr. Themens also deserves extra thanks for his assistance with using E-CHAIM.

I would like to thank fellow students Sydney Ullrich, Adam Lozinsky and Whitney Curtis for providing peer support, programming and debugging help and interesting conversation. I would also like to thank Dr. Ashanthi Maxworth, who I shared a cubicle with, for making my first office job a pleasant experience with her interest in my project and her cheerful conversation. I would also like to thank Keith Kotyk and Marina Schmidt for technical support and programming advice.

I would like to thank the Dr. Koustov, the Department of Physics and Engineering Physics, the CREATE program, the Institute of Space and Atmospheric Studies and Natural Sciences and Engineering Research Council of Canada for providing funding directly and indirectly. Without financial assistance I would not have been able to complete this thesis.

Finally, I would like to thank my friends and family, who encouraged and supported me in too many ways to list.

E-CHAIM is supported under Defence Research and Development Canada contract number W7714-186507/001/SS and is maintained by the Canadian High Arctic Ionospheric Network (CHAIN) with operations support from the Canadian Space Agency. Versions 2.2 (Chapter 3) and 3.21 (Chapter 5) of E-CHAIM were used in this thesis.

Contents

Contents iv

List of tables vii

List of figures viii

1 Introduction 1

1.1 The Earth's Ionosphere . . . 3

1.1.1 Vertical structure and dynamics . . . 3

1.1.2 Dynamics of the ionosphere . . . 5

1.1.3 Effects of particle precipitation . . . 8

1.1.4 Dependence on solar activity . . . 8

1.2 Formation of the Ionosphere . . . 10

1.2.1 Chemical processes at F region heights . . . 10

1.2.2 Chapman theory . . . 11

1.2.3 F1 Layer . . . 13

1.2.4 F2 Layer . . . 13

1.2.5 Topside Ionosphere . . . 14

1.2.6 Winter Anomaly . . . 14

1.3 E-CHAIM model of the electron density in the high-latitude ionosphere . . . 15

1.4 Objective of the thesis work . . . 16

1.5 Thesis Outline . . . 17

2 Instrumentation 18

2.1 Incoherent Scatter Radars . . . 18

2.1.1 Principles of ISR . . . 19

2.1.2 Resolute Bay ISRs (RISR radars) . . . 20

2.1.3 Data Source . . . 24

2.2 Principles of Swarm LP operation . . . 25

2.2.1 General introduction . . . 25

2.2.2 IV curve and density/electron temperature derivation . . . 25

2.2.3 Swarm specific features of LP probes . . . 30

2.2.4 Data Source . . . 32

2.3 Summary . . . 32

3 Topside electron density over Resolute Bay as measured by the Swarm satellites and predicted by the E-CHAIM ionospheric model 33

3.1 Geometry of Swarm satellite trajectories over the Resolute Bay area . . . 34
3.2 Comparisons of Swarm A and Swarm C electron densities . . . 36
3.3 Long term trends in the ionosphere above Resolute Bay: Swarm data and E-CHAIM predictions . . . 41
3.4 Summary . . . 48

4 Topside electron density over Resolute Bay as measured by Swarm satellites and incoherent scatter radars 49

4.1 Introduction . . . 50
4.2 Instruments . . . 52
4.3 Example of Swarm-RISR comparison, the event of 12 October 2016 . . . 54
4.4 Results for multiple events . . . 61
4.4.1 Statistics for the ratio of electron density measured by Swarm and RISR radars . . . 62
4.4.2 Trends in the relationship of Swarm and ISR radar measured electron densities . . . 64
4.5 Discussion . . . 67
4.6 Summary and major conclusions . . . 71

5 Electron density in the ionosphere over Resolute Bay as measured by RISR-C and predicted by the E-CHAIM statistical model 72

5.1 Introduction . . . 72
5.2 Average ionospheric electron density distribution over Resolute Bay . . . 73
5.3 Comparison of RISR-C data and E-CHAIM model output . . . 77
5.3.1 Model-measurement comparison for the electron density peak . . . 77
5.3.2 Model-measurement comparison for various heights . . . 78
5.3.3 Diurnal and seasonal changes in the ratio predicted-to-measured electron densities at various heights . . . 79
5.4 Discussion of the results . . . 82
5.5 Summary and conclusions . . . 84

6 Summary of the results, conclusions and suggestions for future work 86

6.1 Summary . . . 86
6.1.1 Differences of electron density measured by Swarm A and Swarm C . 86
6.1.2 Assessing electron density variations and comparison with E-CHAIM 88

6.1.3 Swarm and RISR electron density comparison 88
6.1.4 Validation of the E-CHAIM ionospheric model with RISR data 89
6.2 Suggestions for future research 89
6.2.1 Further assessment work for Swarm LP instruments 90
6.2.2 Detection of polar cap patches with two Swarm satellites 91
6.2.3 Study of long-term trends in the topside ionosphere 91
6.2.4 Further validation work for the E-CHAIM ionospheric model 92
References **93**
A Supplementary Plot **105**
B Rights to Chapter 4 **106**

List of Tables

4.1 The median value μ and the standard deviation σ for a histogram distribution of the ratio $R = N_e^{Swarm}/N_e^{RISR}$ for the point-to-point satellite-radar data comparison (data set 1) and the comparison that used the height-fitted RISR electron density profiles (data set 2). Also presented is the number of points for each distribution. 63

4.2 The median value μ and the standard deviation σ for a histogram distribution of ratio $R = N_e^{Swarm}/N_e^{RISR}$ for the point-to-point satellite-radar data comparison (data set 1) and the comparison that used the fitted RISR electron density profiles (data set 2). Also presented is the number of points for each distribution. Data for all three Swarm satellites were considered. 63

4.3 Coefficients of a linear fit $N_e^{Swarm} = a \cdot N_e^{RISR} + b$ to a scatter plot of electron density measured by Swarm versus electron density measured by RISR-C/N radars for data sets 1 and 2. Also presented are the number of points (N) for each plot and the Pearson correlation coefficient (r). Values of b are given in units of $10^{10}\mathrm{m}^{-3}$. 66

List of Figures

1.1 Typical electron density profiles of the ionosphere of the Earth. Electron density in number of electrons per cubic meter is given along the x axis and altitude in kilometers is given along the y axis. The approximate altitude ranges of the D, E and F regions of the ionosphere are given along the right y axis. Profiles for low solar activity are dotted while profiles for high solar activity are solid. Image source Papon et al. (2010). 4

1.2 Global distribution of peak electron density (in geographic coordinates) according to the empirical model by Themens et al. (2017) for 16 UT. The pattern is the model-predicted average pattern for April 2013. The electron density is characterized by the critical frequency that is related to the electron density through the relationship $f_0F2[\text{MHz}]=9\times10^{-6}\sqrt{N_mF2}[\text{m}^{-3}]$. Adapted from Themens et al. (2017) by extracting subplot, rescaling and combining with frequency scale. 5

1.3 A sketch showing the formation of polar cap patches propagating from the dayside to the night side following the general plasma flow. Magnetic local time (MLT) is shown along the angular axis and radius is latitude. The top of the plot is the dayside and the bottom is the night side. A clockwise flow cell is shown on the left side of the graph, while a counter clockwise flow cell is shown on the right. The auroral oval (Feldstein, 2016) is shown in yellow. . 7

1.4 Electron density at Resolute Bay, Nunavut as modelled by E-CHAIM (Themens et al., 2017). Colour indicates the electron density. The hour of the day is in magnetic local time (MLT). The plot is courtesy of Sydney Ullrich. 9

1.5 A depiction of a generic Chapman production function for various solar zenith angles. Along the x axis normalized ion production is shown. Production $q(x)$ is normalized to the maximum q_{mo} at 0° solar zenith angle. The y axis shows altitude as reduced height, which is found using $\frac{z-z_{m0}}{H}$, where z is the altitude, z_{mo} is the altitude of maximum production for zero solar zenith angle and H is the scale height. Adapted from Brekke (2013). 12

2.1 Sketch of a typical spectrum of a signal received by ISRs (solid line). Dashed line depicts a spectrum without Doppler shift. Image courtesy of A. Koustov. 19
2.2 Panoramic view of the Resolute Bay RISR-N (left) and RISR-C (right) radar transmit-receive panels. The image is taken from https://aurora.phys.ucalgary.ca/resu/index.html on 28 October 2021. 21
2.3 The field of views of the RISR-C and RISR-N incoherent scatter radars. The diamonds represent the locations of the ionospheric pierce points at 300 km. All beams of the systems are considered. North of ~75° latitude are RISR-N points while south of ~75° are RISR-C points. The diagram was produced by Dr. Gillies, University of Calgary. 22
2.4 The standard RISR plot of the electron density at various ionospheric heights versus universal time (UT) as measured by the RISR-C radar in beam 5 in the Word Day experiment mode run between 05 and 07 March 2016. Image credit: Donovan (2016). 23
2.5 (a) Scatter plot of errors in RISR-C measurements of the electron density versus absolute value of measured electron density. The entire database of joint Swarm A/C and RISR-C observations in the World Day mode (see details in Chapter 4) were considered. (b) The same as (a) except for relative errors in RISR-C measurements (error/value). 24
2.6 Schematic of a biased spherical Langmuir probe with Debye sheath indicated. Image adapted from (Bhattarai & Mishra, 2017). 26
2.7 Probe current as a function of probe bias, with the three current regions indicated. The point at which electron temperature can be measured is indicated by T_e. (Adapted from Schunk & Nagy, 2009). 27
2.8 Langmuir Probe installation on a Swarm satellite ("EFI instrument - Swarm - ESA Earth Explorer Missions - Earth Online - ESA", 2020). Top Left: an image of a Langmuir probe used on a Swarm satellite, adapted from Knudsen et al., 2017. 31

3.1 Daily mean pass altitude of the Swarm satellites for the period of 2014-2019. Note that during the first quarter of 2014, the satellites were still manoeuvring from launch orbits into mission orbits. 35

3.2 a) and b) Footprints of the Swarm A and C satellites at the height of 450 km as they travel over the Resolute Bay zenith (green circle) on 06 June 2015 (daytime) and 09 June 2015 (nighttime). The colored bars across the tracks reflect measured electron density. The electron density is given in units of 1×10^{10} m^{-3}. The scale is given by a vector in the top-left corner. c) and d) Comparison of the electron density medians computed in 0.2 ° bins of geographic latitude along the tracks, for the daytime and nighttime passes, respectively. Vertical and horizontal bars are standard deviations of data in each data bin. Presented also are the expressions for the linear fit lines assuming either Swarm C (green) or Swarm A (purple) values are known precisely. 37
3.3 Pearson correlation coefficient for Swarm A - Swarm C electron density monthly datasets collected over the Resolute Bay area during 2014-2018. Data in all time sectors were considered. Red curve is a smoothed variation obtained by applying a car box filter with 3 consecutive values. 39
3.4 Pearson correlation coefficient distributions for joint Swarm A - Swarm C electron density data collected over the Resolute Bay area during 2014 (starting from April)-2018. Each distribution includes 350-400 points. Panels a)-c) are for daytime measurements (16-23 UT) while panels d) - f) are for nighttime measurements (02-10 UT). 41
3.5 Electron density over Resolute Bay (RB, Nunavut, Canada)) in coordinates "local time-year" a) according to the E-CHAIM model (Themens et al., 2017) and b) Swarm A and C measurements. The E-CHAIM data are for the height, location and time of Swarm measurements (see the text). 43
3.6 Electron density near the Resolute Bay zenith as predicted by the E-CHAIM model (Themens et al., 2017) and measured on Swarm A and C satellites for 2014-2018. Time sectors were introduced as follows: dawn (3:00 to 9:00 LT), day (9:00 to 15:00 LT), dusk (15:00 to 21:00 LT), and night (21:00 to 3:00 LT). The model values (lines) are medians of all values available for a specific time sector. 44
3.7 The same as in Figure 3.5 but for Swarm B measurements and corresponding E-CHAIM predictions. 46
3.8 Scatter plots of the electron density predicted by the E-CHAIM model for the height and time of a) Swarm A and b) Swarm B measurements near Resolute Bay (for criteria of co-location see the text). The data are binned in steps of 1×10^{10} m^{-3}. 47

4.1 Swarm A and Swarm C satellite tracks (two lines across the diagram) and the ionospheric locations at the altitude of ~450 km (colored circles) where the electron density was measured by the Resolute Bay (black square) incoherent scatter radars. The event of 12 October 2016 is considered. Circles to the North-East of the square are locations for the RISR-North radar measurements while circles to the South-West of the square are locations for the RISR-Canada radar measurements. The electron density is given in units of 10^{10} m^{-3} according to the color bar shown on the right. Individual points of radar measurements "collocated" with Swarm A tracks (with separation of <200 km) are emphasized by black circles. 55

4.2 Electron density measured by Swarm A and Swarm C as they travel near Resolute Bay, Nunavut on 12 October 2016 and electron density measured by the RISR incoherent scatter radars. (a) Electron density according to Swarm A (blue) and C (red) plotted versus geographic latitude. (b) The same data as in (a) but presented as a scatter plot of individual measurements taken as the median value in a bin of 0.2° latitude. The red line is the bisector of perfect agreement. (c) Scatter plot of the electron density measured by Swarm A against ISR electron density at the conjunction points for the selected pass. The horizontal bar for each point is the error in ISR measurement while the vertical bar for each point is the standard deviation in each bin of Swarm data. (d) The same as (c) but for the Swarm C satellite. 57

4.3 (a), (c)-(e) Electron density profiles as measured by the Resolute Bay incoherent scatter radars (ISR), solid beige circles with horizontal bars representing the error of measurements, and the electron density according to Swam Langmuir Probe measurements at closest locations (less than 200 km separation) best matching ISR measurement interval in time (blue circles). The median value of the Swarm measurements is marked by a red vertical bar. The black line is the best fit line to the RISR electron density profile, as described in the text. 60

4.4 Data on the occurrence of conjunctions between Swarm (for all three satellites) and (a) RISR-North and (b) RISR-Canada incoherent scatter radar measurements. 61

4.5 Distributions of the ratio $R = N_e^{Swarm}/N_e^{RISR}$ for the (a) Swarm A, (b) Swarm C and (c) Swarm B satellites for all radar-satellite conjunctions (2014-2019) while point-by-point comparison (data set 1) is made. Each histogram is characterized by the median value (μ) and the standard deviation value (σ). The values for μ and σ are reported in the upper right corner. 62

4.6 Electron density measured onboard the Swarm satellites versus electron density measured by the Resolute Bay incoherent scatter radars RISR-C/N at close locations and at close time. The left, center and right panels are for Swarm A, C and B, respectively. The top row panels are the direct point-by-point comparisons (data set 1) while the bottom row panels are comparisons by considering RISR electron density height profiles fitted by a curve (data set 2). 64

4.7 Electron density measured onboard Swarm C satellite (N_e^{Swarm}) versus electron density measured by the Resolute Bay incoherent scatter radars RISR-C/N (N_e^{RISR}) at close locations and at close time. Data set 1 was considered (see the text). (a) All available conjunctions are considered. Red dots are medians of N_e^{Swarm} (Swarm C) in bins of N_e^{RISR}. Vertical bars are standard deviations of N_e^{Swarm} in each bin of N_e^{RISR}. (b) The same data as in (a) but filtered by applying the median absolute deviation technique (see the text). 65

5.1 Hourly number of points of RISR-C WD mode measurements in various months of observations in 2016-2018. Measurements presented are filtered by relative error ($\leq 50\%$), by elevation angle of the radar beam ($> 45^\circ$) and by measurement altitude (between 100 and 500 km). 74

5.2 Electron density distribution in the ionosphere over Resolute Bay according to RISR-C observations in 2016-2018. Presented are hourly median values of Ne in 25-km height bins. 75

5.3 (a) Scatter plot of the peak electron density N_mF2 inferred from E-CHAIM model versus RISR-based peak electron density N_mF2 for matched moments. 5-min RISR-C data in the World Day mode of operation in 2016-2018 were considered. The total number of available points N is shown in the top left corner of each panel. The number of points in each pixel of the plot is coded according to the color bar to the right. (b) The same as (a) but for the height of the electron density maximum h_mF2. 78

5.4 Scatter plot of the electron density inferred from E-CHAIM model versus RISR-based electron density for matched moments and heights. 5-min RISR-C data in the World Day mode of operation in 2016-2018 were considered. The number of points in each pixel of the plot is coded according to the color bar to the right. The total number of available points N is shown at the top left corner of each panel. (a), (b) and (c) are for the height of 200 km, 300 km and 450 km. 79

5.5 The ratio of E-CHAIM predicted to RISR measured electron density for all events available in 2016-2018. The data have been binned according to season, as indicated. 80
5.6 Histogram distributions for the ratio of E-CHAIM predicted to RISR measured electron density at three different ranges of heights and for four seasons. Each histogram is characterized by the median value (μ) and the standard deviation value (σ), reported in the upper right corner. Also presented is the number of points N for each distribution. 82

A.1 Scatter plot of the electron density inferred from E-CHAIM model versus RISR-based electron density for matched moments and heights. 5-min RISR-C data in the World Day mode of operation in 2016-2018 were considered. The number of points in each pixel of the plot is coded according to the color bar to the right. The total number of available points N is shown at the top left corner of each panel. 105

Abbreviations by order of appearance

IMF	Interplanetary Magnetic Field
HF	High Frequency
LEO	Low Earth Orbit
E-CHAIM	Empirical Canadian High Arctic Ionospheric Model
MLT	Magnetic Local Time
IRI	International Reference Ionosphere
AACGM	Altitude-Adjusted Corrected Geomagnetic
RO	Radio Occultation
DoY	Day of Year
UT	Universal Time
ISR	Incoherent Scatter Radar
LP	Langmuir Probe
SuperDARN	Super Dual Auroral Network
GPS	Global Positioning Satellite
VHF	Very High Frequency
UHF	Ultra High Frequency
ACF	Autocorrelation function
RISR	Resolute Bay Incoherent Scatter Radar
RISR-N	RISR-North
RISR-C	RISR-Canada
FoV	Field of view
WD	World Day
I-V	Current-voltage
PCC	Pearson's correlation coefficient
LT	Local time
CHAMP	Challenging Minisatellite Payload
COSMIC	Constellation Observing System for Meteorology, Ionosphere, and Climate
CADI	Canadian Advanced Digital Ionosonde
DMSP	Defense Meteorological Satellite Program

Symbols by order of appearance

The subscripts e and i are used to indicate electrons and ions respectively, while the subscript α is used to indicate either species of particle.

$N_m F2$	Peak electron density of the F2 layer
$h_m F2$	Altitude of the peak electron density of the F2 layer
$f_0 F2$	Critical frequency of the ionosphere
m_α	Charged particle mass
q_α	Charged particle charge
$\vec{v}_\alpha$	Charged particle velocity
$\vec{u}_n$	Neutral particle velocity
$\nu_{\alpha n}$	The collision frequency of charged particles with neutral particles
Ω_α	Particle gyro frequency
v_E	Charged particle speed from electric and magnetic fields only
$\vec{E}$	Electric field vector
$\vec{B}$	Magnetic field vector
n	Particle density
n_0	Reference particle density
z	Altitude
H	Scale height
k_B	Boltzmann constant
T	Particle temperature
m	Particle mass
g	Gravitational acceleration in the near Earth environment
X, Y, Z	Generic chemical species
h	Planck's constant
ν	Frequency
e	Free electron, elemental charge
L	Recombination rate
α_r	Alpha recombination coefficient
n_e	Electron density
n_i	Ion density
β_r	Beta recombination coefficient
q	Production rate
q_{m0}	Production at zero solar zenith angle
z_{m0}	Altitude of maximum production at zero solar zenith angle

V_f	Floating voltage of a Langmuir probe
V_p	Plasma potential
V_b	Langmuir probe bias voltage
λ_D	Debye length
ϵ_0	Permittivity of free space
T_e	Electron temperature
$I_{\alpha s}$	Saturation current
$v_{\alpha,th}$	Particle thermal velocity
A	Probe surface area
T_i	Ion temperature
E_i	Collision energy of ions
Y	Admittance
V	Voltage
A_c	Cross sectional area of Langmuir probe
I_{ret}	Langmuir probe current in electron retarding region
I_{acc}	Langmuir probe current in electron accelerating region
V_{ret}	Langmuir probe voltage in electron retarding region
V_{acc}	Langmuir probe voltage in electron accelerating region
N_e^{SwarmA}	Density measured by Swarm A
N_e^{SwarmC}	Density measured by Swarm C
N_e^{RISR}	Density measured by RISR
k_1	Constant fitting coefficient
k_2	Exponential fitting coefficient
R	Ratio of N_e^{SwarmA}/N_e^{RISR}
μ	Distribution median
σ	Distribution standard deviation
f_p	Plasma frequency
a	Linear fit coefficient
b	Linear fit constant
r	Pearson's correlation coefficient
$N_{200}^{E-CHAIM}$	Density as predicted by E-CHAIM at 200 km altitude
N_{200}^{RISR}	Density as measured by RISR-C at 200 km altitude
$R_{p/m}$	Ratio $N_{200}^{E-CHAIM}/N_{200}^{RISR}$

Chapter 1

Introduction

The Earth's ionosphere is defined as the region of the upper atmosphere where ionized atmospheric gases and free electrons exist but the bulk of the particles are neutral. The charged particles form what is called plasma, which is a state of matter defined as an ionized gas for which the long-range forces of a collection of particles control the dynamics of individual ions and electrons (Kivelson & Russell, 1995).

The ionosphere begins at approximately 60 kilometres above the surface of the Earth and extends up to 1000 km or farther. At the upper limit the atmosphere becomes fully ionized, with the major species being protons and electrons. The fully ionized plasma around the Earth extends into the plasma that exists in the interplanetary space within the solar system and beyond.

The lower regions of the ionosphere are formed from ionization of ionospheric gases such as O_2, N_2 and NO, caused by incoming solar radiation. The precipitation of energetic particles from the Earth's near space environment, driven by the interaction of the solar wind with the magnetic field of the Earth, also contributes to the formation of the ionosphere at high latitudes. The effect of these precipitating particles is most readily seen as aurora. The upper regions of the ionosphere are formed from a more complex combination of ionization from solar radiation and diffusion processes.

The plasma in the ionosphere is a very dynamic medium. Plasma gets redistributed across the globe by the action of neutral winds and electric fields that are particularly strong at high latitudes. Electric fields are present in the ionosphere as a result of complex interactions between the magnetic field of the Earth and the interplanetary magnetic field (IMF), which originates at the Sun.

Although the fundamental processes of the creation and dynamics of the Earth's ionosphere have been identified, many of their details are still unknown. Quantitative description of these processes is far from the point where reasonable predictions of the near-space parameters, the so-called Space Weather, would be as routine as those for the meteorological weather (Kutiev et al., 2013; National Research Council (U.S.), 2013; Schunk & Nagy, 2009).

Understanding and quantifying the ionosphere is important because many practical engineering systems are impacted by the ionosphere. The ionosphere can refract and reflect radio waves of various frequencies due to the highly conductive nature of the ionospheric plasma. The high frequency (HF) band is one of the frequencies at which these effects occur regularly. Thus, communications at HF, used, for example, by the military for over-the-horizon radar installations and air traffic control systems in civilian aviation are among others that are sensitive to changes in the ionosphere (Davis, 1990; Hunsucker, 1991; Rawer, 2013). Global navigation satellite systems are also affected by ionospheric conditions. Another impact on human activities occurs because the electric fields in the ionosphere create strong electric currents, and those currents affect the corrosion processes in pipelines (Knudsen et al., 2017; Pirjola et al., 2000). Consequently, the prediction of violent ionospheric events has environmental and economic merit, which in turn imparts value to the study of the ionosphere.

The experimental study of the ionosphere can be conducted using both ground-based and space-based instruments. Ground-based observation systems have provided the bulk of information on the ionosphere. However, these observations are often limited in spatial coverage and are difficult to coordinate for concurrent global coverage. Space-based observations became possible in the 1960s with the advent of high-altitude rockets and satellites. Observation from satellite platforms can provide superior spatial resolution along specific trajectories. Observation with satellite-based instruments has become increasingly common, however, the expense and limited lifetimes of space missions have been factors limiting their use. A recent trend in ionospheric studies is to combine ground-based and space-based observations.

Satellites are particularly critical in the study of the region of the ionosphere commonly referred to as the topside. The topside ionosphere is so named because it is above the plasma electron density peak, which is at ~300 km in altitude. For many ground-based radio systems, their radio waves cannot penetrate through the layer of high density, thus preventing measurements of the topside of the ionosphere. Rockets can only provide data on a single location for a very short time period, and rockets seldom reach the height of the electron density peak. Consequently, rockets do not present a practical method for observing more than a single point in time and space. However, satellites in a low Earth orbit (LEO) are well suited to observations of the ionosphere, including its topside.

This thesis is focused on the investigation of the high-latitude ionosphere in the Canadian sector of the Arctic by combining data from ground-based radars and in-situ measurements on satellites crossing the radars' field of view. Before proceeding with formulation of the goals of the work, a short introduction to the main concepts of ionospheric physics is presented.

1.1 The Earth's Ionosphere

The following description of the ionosphere is based on the books "*Physics of the Upper Polar Atmosphere*" (Brekke, 2013), "*The Earth's Ionosphere*" (Kelley, 2009), "*Introduction to Space Physics*" (Kivelson & Russell, 1995) and "*The Solar-Terrestrial Environment*" (Hargreaves, 1992).

1.1.1 Vertical structure and dynamics

Although the ionosphere does not have definitive physical boundaries, it is divided into regions. These regions are sometimes referred to as layers. The regions are loosely defined but are generally assigned to altitude ranges derived from typical ionosphere electron density profiles. Figure 1.1 presents the various regions and typical electron density profiles for differing seasons and times of day.

The lowest region, the D region, extends from the bottom of the ionosphere at ~60 km to ~90 km. The electron density of the D region is nominally 10^{10} electrons per m^{-3} and increases rapidly with altitude. The next region, the E region, extends from ~90 km up to 120-130 km, with peak density of 1×10^{11} m^{-3}. The E region is characterized by the presence of a peak, where the increase in electron density with altitude slows to zero and then decreases at larger heights. The next highest layer is called the F layer and it has two peaks where the electron density experiences a local maximum. The lower peak, the F1 peak, is generated by solar ionization and normally vanishes at night. The second, or F2, peak does not disappear at night. The typical altitude of the F2 peak is 300 km. The F2 peak is a commonly used reference point in ionosphere models, which reference the peak electron density as N_mF2 and the altitude of the peak as h_mF2. The F2 peak is the densest point in the ionosphere, with a typical electron density value of 1×10^{12} m^{-3}. The region above the F2 peak is known as the topside ionosphere and is characterized by a gradual, close to exponential, decrease in electron density as the atmosphere itself fades into space. Typical electron density profiles for daytime and nighttime as well as for high and low solar activity are shown in Figure 1.1. This thesis is focused on electron density distribution at the F region heights, and discussions below tacitly assume the F region heights. The ionosphere below the F2 peak, comprised of the D and E layers, is often called the bottomside.

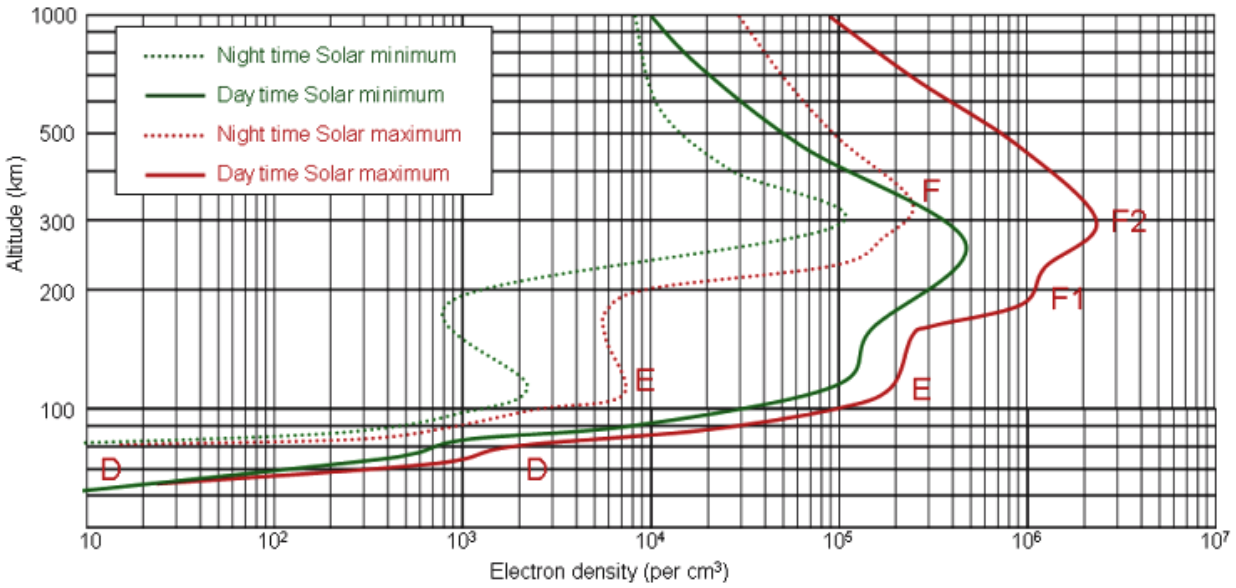

Figure 1.1: Typical electron density profiles of the ionosphere of the Earth. Electron density in number of electrons per cubic meter is given along the x axis and altitude in kilometers is given along the y axis. The approximate altitude ranges of the D, E and F regions of the ionosphere are given along the right y axis. Profiles for low solar activity are dotted while profiles for high solar activity are solid. Image source Papon et al. (2010).

The ionosphere has a three-dimensional structure. In addition to structure related to altitude, it also has a structure along both the latitude and the longitude directions. An example 2-D distribution of the peak electron density in the ionosphere is given in Figure 1.2. The shown distribution is the Empirical Canadian High Arctic Ionospheric Model (E-CHAIM) predictions for the month of April 2013 at 16:00 UT. The electron density is characterized by the so called critical frequency of the layer which is related to the electron density through the relationship (Hargreaves, 1992; Kivelson & Russell, 1995)

$$f_0F2[\text{MHz}] = 9 \times 10^{-6}\sqrt{N_mF2}[\text{m}^{-3}] \tag{1.1}$$

At 16 UT, the local noon is located in the Greenland sector. An enhanced electron density, shown in red in Figure 1.2, stretches from Central Canada to Europe at latitudes ~50-60° North. Here the electron densities are ~2.4×10^{11} m^{-3} (f_0F2=7 MHz). There is a clear decrease of the electron density toward the north, with values in the North Pole area on the order of 2.1×10^{11} m^{-3} (f_0F2=5.5 MHz). At a lower latitude on the nightside, in the Japanese sector, the density reaches its minimum value of ~1.3×10^{11} m^{-3}(f_0F2=2 MHz). The pattern of the electron density decreasing toward midnight is generally asymmetric longitudinally. It should be noted that the pattern presented is highly averaged but still shows 2-D structuring

in a clear way.

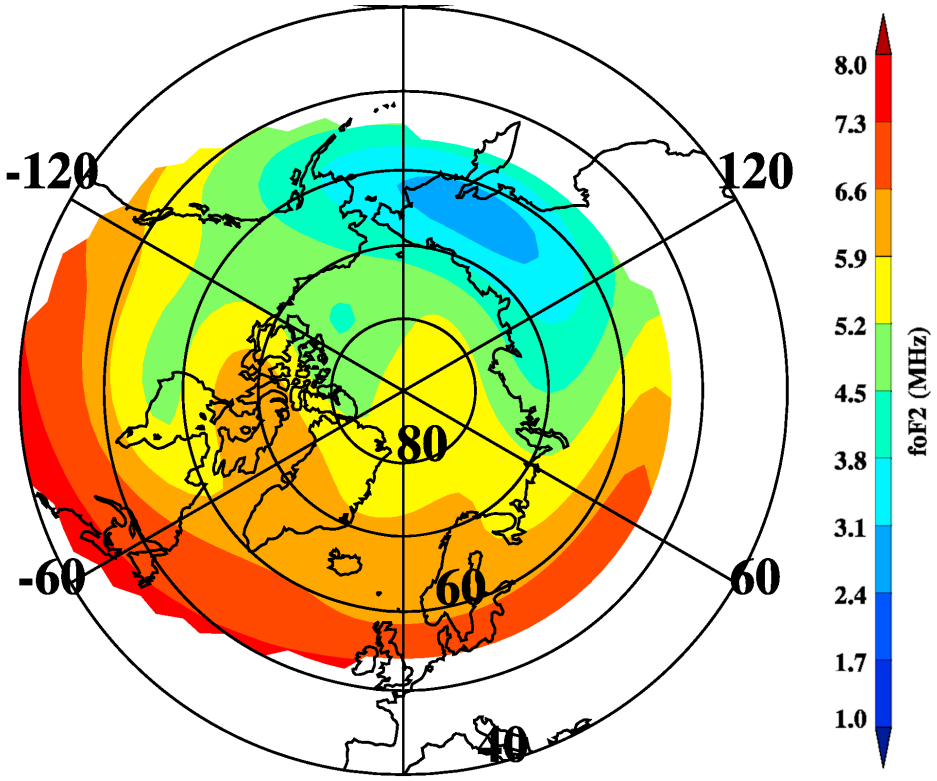

Figure 1.2: Global distribution of peak electron density (in geographic coordinates) according to the empirical model by Themens et al. (2017) for 16 UT. The pattern is the model-predicted average pattern for April 2013. The electron density is characterized by the critical frequency that is related to the electron density through the relationship $f_0F2[\text{MHz}]=9\times10^{-6}\sqrt{N_mF2}[\text{m}^{-3}]$. Adapted from Themens et al. (2017) by extracting subplot, rescaling and combining with frequency scale.

1.1.2 Dynamics of the ionosphere

Observations show that the electron density in the ionosphere changes on timescales ranging from minutes to hours and days. The slow processes of the electron density redistribution can be related to the solar illumination that ionizes the atmosphere. Solar illumination produces warm, dense plasma on the dayside of the Earth. This plasma is pushed to other parts of the ionosphere, globally, due to the pressure gradient force. Faster dynamic changes are related to the effects of neutral particle motion (winds) and plasma drift due to electric and magnetic fields.

Electric fields in the high-latitude ionosphere are established due to continuous plasma flow, the solar wind. Such plasma carries embedded IMF around the Earth's magnetosphere, the region of space around the Earth that is dominated by the Earth's magnetic field (e.g.,

Hargreaves, 1992; Kivelson & Russell, 1995). Two major processes have been identified, the quasi-viscous interaction of the solar wind plasma and the magnetospheric plasma at the outer boundary of the magnetosphere and merging/reconnection processes between the IMF and magnetic field lines of the Earth's dipole (e.g., Hargreaves, 1992; Kivelson & Russell, 1995). The merging can occur on the front side of the magnetosphere or at its high-latitude lobes, depending on the orientation of the IMF. It has been established that about 75% of the time, the large-scale electric field in the ionosphere is directed from dawn to dusk (Brekke, 2013; Kelley, 2009).

To explain how neutral winds and electric fields control plasma motions in the ionosphere one must consider the fluid equation of motion for electrons and ions in the ionosphere (Kelley, 2009). Considering the case of the cold plasma approximation (neglecting temperature and thus pressure) and neglecting the effect of gravity, the equation of motion is given by

$$m_\alpha \frac{d\vec{v}_\alpha}{dt} = q_\alpha(\vec{E} + \vec{v}_\alpha \times \vec{B}) - m_\alpha \nu_{\alpha n}(\vec{v}_\alpha - \vec{u}_n) \tag{1.2}$$

where α represents the species, ions or electrons, m_α and q_α are the mass and charge of the species respectively, $\vec{v}_\alpha$ is the velocity, $\nu_{\alpha n}$ is the species collision frequency with neutrals, $\vec{u}_n$ is the neutral wind velocity, and $\vec{E}$ and $\vec{B}$ are the electric and magnetic field vectors respectively.

For steady state conditions ($\frac{d}{dt} = 0$), the fluid species velocity $\vec{v}_\alpha$ from Equation 1.2 can be rewritten such that the velocity component due to electric field and the velocity component from neutral wind can be written separately,

$$\vec{v}_{0\alpha}(E\ Field) = \frac{\Omega_\alpha \nu_{\alpha n}}{\Omega_\alpha^2 + \nu_{\alpha n}^2} v_E \frac{\vec{E}}{|\vec{E}|} + \frac{\Omega_\alpha^2}{\Omega_\alpha^2 + \nu_{\alpha n}^2} v_E \frac{\vec{E} \times \vec{B}}{|\vec{E} \times \vec{B}|} \tag{1.3}$$

$$\vec{v}_{0\alpha}(wind) = \frac{\nu_{\alpha n}^2}{\Omega_\alpha^2 + \nu_{\alpha n}^2} \vec{u}_n + \frac{\Omega_\alpha \nu_{\alpha n}}{\Omega_\alpha^2 + \nu_{\alpha n}^2} \vec{u}_n \times \frac{\vec{B}}{|\vec{B}|} \tag{1.4}$$

where Ω_α is the particle gyro frequency given by $\Omega_\alpha = \frac{q_\alpha \vec{B}}{m_\alpha}$ and $v_E = \frac{E}{B}$ is the collisionless plasma speed of motion in crossed electric and magnetic fields, which can be derived from Equation 1.2 by assuming no collisions.

In Equations 1.3 and 1.4, the first terms on the right hand side describe particle fluid motion along the direction of electric field and neutral wind, respectively, and the second terms describe particle motion along the $\vec{E} \times \vec{B}$ and $\vec{u}_n \times \vec{B}$ directions, respectively. In both cases, only motions in a plane perpendicular to the magnetic field were considered.

The effect of the electric field in the F-region, where $\nu_{\alpha n} << \Omega_\alpha$, is that both electrons

and ions are primarily moving along the $\vec{E} \times \vec{B}$ direction at the same speed $v_E = \frac{E}{B}$. Such common drift is often referred to as the plasma convection. Typical speeds of $\vec{E} \times \vec{B}$ drift in the high-latitude ionosphere are 300-500 m/s.

Because of the neutral wind, ions are slowly moving in the $\vec{u}_n \times \vec{B}$ direction while electrons are moving in the opposite direction (electrons have a negative gyro frequency due to their charge), but the speed of ions is greater. A typical speed of neutral winds is 100 m/s (Brekke, 2013; Kivelson & Russell, 1995) implying that electric fields, on average, are an important factor in understanding the dynamics of plasma motions at the F region heights. The effects of neutral winds are more critical for the middle latitude and equatorial ionosphere and will not be discussed in this thesis.

The global-scale electric field, oriented from dawn to dusk, applied to the high-latitude ionosphere drives plasma over the Pole area from dayside on the nightside, Figure 1.3. In Figure 1.3, the lines of plasma flow are represented by contours of constant electric potential. It can be seen that plasma arriving at the night sector at latitudes ~70° is "deflected" to flow back toward daytime along much lower latitudes. This return flow, in combination with the anti-sunward transpolar flow, makes two distinct cells, and for this reason, this (most typical) pattern of global plasma circulation is called the two-cell convection pattern (Kelley, 2009; Kivelson & Russell, 1995). With typical differences between the contours of 10 kV in Figure 1.3, the total potential difference between the centers of the two cells is 60-80 kV (Chisham et al., 2007; Kelley, 2009).

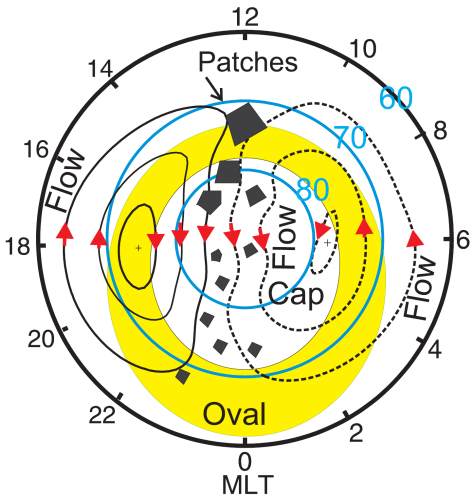

Figure 1.3: A sketch showing the formation of polar cap patches propagating from the dayside to the night side following the general plasma flow. Magnetic local time (MLT) is shown along the angular axis and radius is latitude. The top of the plot is the dayside and the bottom is the night side. A clockwise flow cell is shown on the left side of the graph, while a counter clockwise flow cell is shown on the right. The auroral oval (Feldstein, 2016) is shown in yellow.

1.1.3 Effects of particle precipitation

Aside from ionization from incoming solar illumination, the ionization of the atmospheric molecules and atoms also occurs when energetic particles precipitate into the upper atmosphere. The processes of particle accumulation in the magnetospheric tail and radiation belts and their acceleration into the upper atmosphere is an area of active research (Brekke, 2013; Kelley, 2009; Kivelson & Russell, 1995). It is important to realize that precipitations most frequently occur in the auroral oval region (Feldstein, 2016), indicated in yellow in Figure 1.3. The auroral oval is asymmetric and is shifted to lower latitudes on the nightside. Although originally the oval was introduced as a region of the most frequent occurrence of auroral arcs, the subsequent measurements by satellites confirmed that the auroral oval does reflect the overall precipitation pattern and thus has a more broad application. It should be noted that the oval depends on the level of solar activity, which is routinely characterized by magnetic perturbations detected by magnetometers on the ground. When solar and magnetic activity increases, the oval becomes thicker and it expands to lower latitudes (Brekke, 2013). Peak electron densities are typically the largest at latitudes of the auroral oval.

The plasma density poleward of the auroral oval is usually depleted, especially in winter. This region is referred to as the polar cap. Despite the depletion, high peak electron densities in the polar cap are still often observed. The current theory is that blobs of high electron density plasma are detached from the main bulk of the plasma at middle latitudes and are $\vec{E} \times \vec{B}$ driven along the two cell circulation pattern from the dayside to the nightside. Such blobs are referred to as polar cap patches. Formation of polar cap patches is a field of active research (Jin et al., 2019; Moen et al., 2007; Spicher et al., 2015).

1.1.4 Dependence on solar activity

Because ionosphere dynamics and precipitation processes are driven by the Sun, the electron density varies with time of the day, season and solar cycle. Seasonal trends in the ionosphere are also produced in response to changes in the tilt in the axis of rotation of the Earth with respect to the orbital plane. As a result of the tilt, in the Northern Hemisphere ionization generally decreases in winter and increases in summer. In the Southern Hemisphere, the reverse happens.

Solar activity shows cyclic variations and produces similar cyclical variations in the ionosphere on the scale of years. High solar activity is correlated with increased plasma electron density, see Figure 1.1 for an example. The effect of solar activity is shown in Figure 1.4, which shows the electron density values, at 450 km altitude, according to year and time of day above Resolute Bay, Nunavut as modelled by E-CHAIM (Themens et al., 2017). The

gradual decrease in electron density from 2013 to 2018 follows solar activity, which peaked in 2013 and has decayed until the present. Additional seasonal trends are also evident in the increased electron density at the equinoxes. The effect of the time of day can also be seen in the increase of electron density observed pre-noon and extending past noon. The high electron density observed in March 2014, on top of the solar and seasonal trends, shows that additional processes affect the ionosphere.

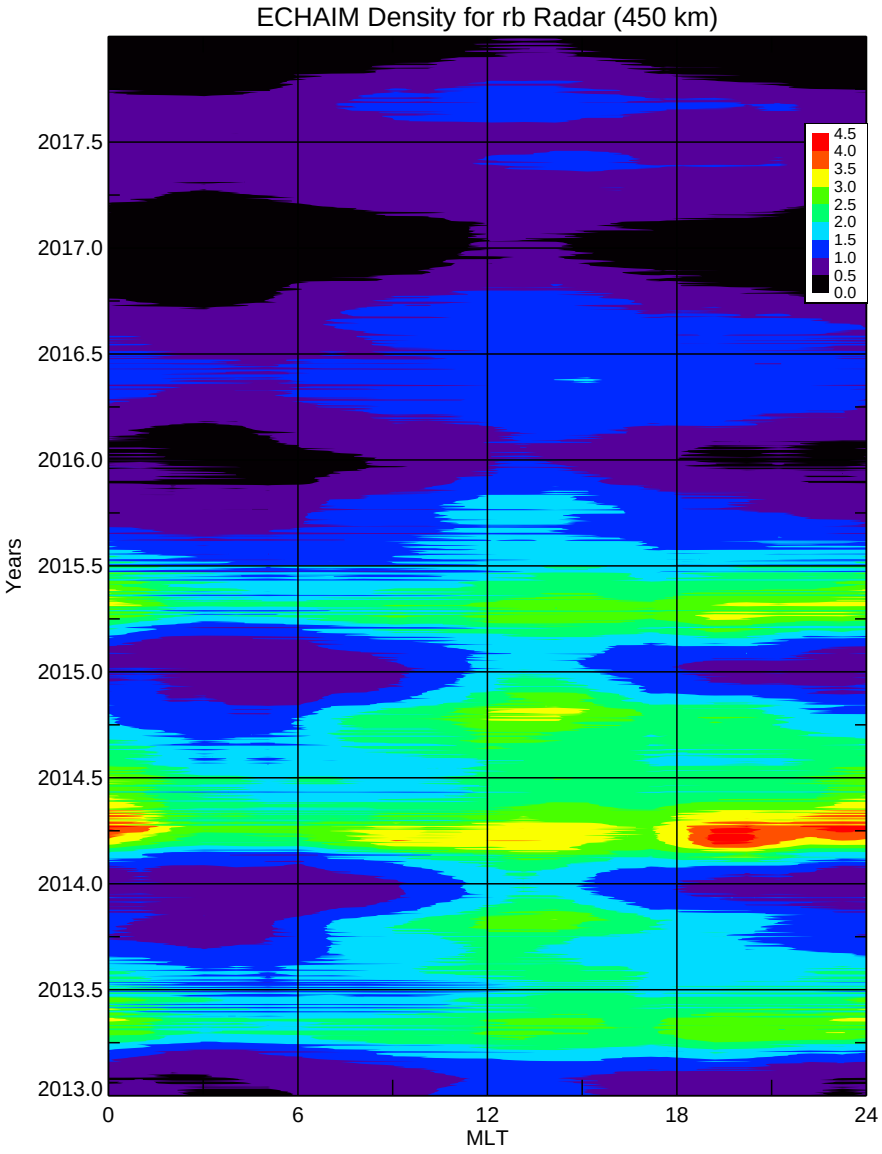

Figure 1.4: Electron density at Resolute Bay, Nunavut as modelled by E-CHAIM (Themens et al., 2017). Colour indicates the electron density. The hour of the day is in magnetic local time (MLT). The plot is courtesy of Sydney Ullrich.

1.2 Formation of the Ionosphere

Aside from acknowledging the sources of ionization, solar illumination and particle precipitation, understanding the formation of the ionosphere requires understanding the typical chemical reactions occurring and how they change with altitude. Since the focus of this thesis is on F region heights, the discussion of ionosphere formation introduced below is limited to F region heights.

1.2.1 Chemical processes at F region heights

Neutral particles, either atoms or molecules, in the ionosphere are distributed according to the exponential law

$$n(z) = n_0 e^{-\frac{z}{H}} \qquad H = \frac{k_B T}{mg} \tag{1.5}$$

where k_B is the Boltzmann constant, z is altitude, T and m are the temperature and mass of particles and g is the gravity constant. The value of the constant H, known as the scale height, depends on the altitude. Below ~100 km, the constituents of the atmosphere are well mixed, and the value of H is the same for all of them. For this region of the atmosphere, the homosphere, H is equal to ~7 km. Above that height, the value of H is different for various constituents, with smaller values for heavier molecules, so that at heights of ~1000 km hydrogen and helium atoms become significant and eventually dominate. At F region heights of ~300 km, the dominating spices are molecules of N_2 and atomic O (Hargreaves, 1992, Fig. 2.3). However, molecules of O_2 and atomic He are also present.

In the simplest case, the electron-ion pairs are produced by solar radiation. The most important process is

$$X + h\nu \rightarrow X^+ + e \tag{1.6}$$

where X is a generic chemical species, h is Plank's constant, ν is the photon frequency and e is a free electron. At high latitudes, the impact of precipitating particles can be more important. In the F region, photo-ionization produces an abundance of O^+, consequently the most abundant ion in the F region is O^+. The created electron-ion pairs can recombine through a number of reactions (Kivelson & Russell, 1995) such as

$$e + X^+ \rightarrow X + h\nu \qquad (\textit{radiative recombination}) \tag{1.7}$$

$$e + XY^+ \rightarrow X + Y \qquad (\textit{dissociative recombination}) \tag{1.8}$$

$$e + Z \rightarrow Z^{-} \qquad (attachement) \tag{1.9}$$

In the E region, the dissociative recombination reaction equation 1.8 is the most important. The recombination occurs at a rate

$$L = \alpha_r n_e n_i \qquad \text{assuming } n_e \approx n_i, \quad L = \alpha_r n_e^2 \tag{1.10}$$

where α_r is the recombination coefficient. For the F region heights above 200 km, atomic O dominates, and the fastest recombination reaction generally follows a two-step process, whereby a chemical reaction occurs prior to recombination. How fast that chemical reaction occurs thus controls the recombination rate. Charge exchange with neutral species, such as that given in reaction Equation 1.9 is most important at F region heights. The rate of recombination in this case is given by

$$L = \beta_r n_e \tag{1.11}$$

where β_r is the recombination coefficient.

1.2.2 Chapman theory

The first description of the processes leading to the formation of the ionosphere was given by Sydney Chapman (Akasofu, 2011; Chapman, 1931), and related functions since then are known as Chapman functions. A full description of the formation of the ionosphere is complex, since the particle density of different species of neutrals drops at different rates, the wavelength required to ionize each species also varies, recombination reactions occur at different rates and the ionization rate depends on solar zenith angle (Brekke, 2013). Additional complexity is added when a particular ion can recombine using multiple pathways. Consequently, simplified models that consider only the dominant ion species and the most likely reactions are used when the focus is not on the details of the production/recombination processes. The profile of a simple Chapman model, which includes only a single species production function and a dependence on solar zenith angle, is shown in Figure 1.5.

Chapman theory is based on an assumption that there is an equilibrium and the electron-ion production rate is matched by the recombination rate such that the continuity equation can be written as

$$\frac{\partial n_e}{\partial t} + \nabla \cdot (n_e \vec{v}_e) = q - L = 0 \tag{1.12}$$

where $\vec{v}_e$ is the velocity of the bulk plasma, q is the electron-ion pair production rate and L is the rate of pairs' losses. The simplest Chapman theory is concerned with deriving the

expression of the q term, where only one ion species is considered. The recombination can generally be of two types, α type and β type, as given in Equations 1.10 and 1.11.

Chapman theory computes the rate of electron-ion pair production when photons, from incident sunlight, pass through the atmosphere. Two effects are considered, the decrease in the neutral particle density of gas with altitude and decrease of photon flux as the photons travel through the gas.

Considering both effects together results in the production rate profiles given in Figure 1.5, where ionization at high altitudes is limited by low atmospheric particle density and increases as altitude decreases and atmospheric particle density rises. The process reaches a maximum after which ionization is limited by the light intensity and decreases as less light reaches lower altitudes.

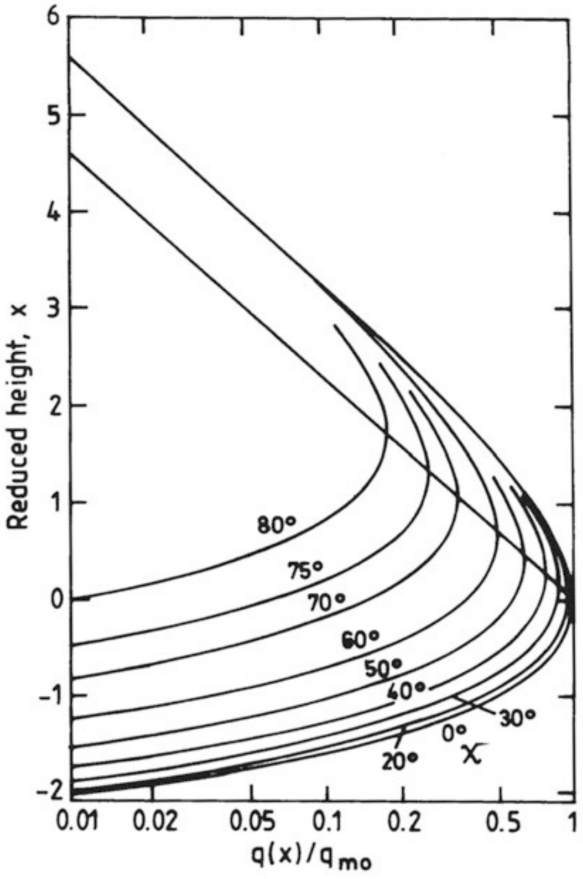

Figure 1.5: A depiction of a generic Chapman production function for various solar zenith angles. Along the x axis normalized ion production is shown. Production $q(x)$ is normalized to the maximum q_{mo} at 0° solar zenith angle. The y axis shows altitude as reduced height, which is found using $\frac{z-z_{m0}}{H}$, where z is the altitude, z_{mo} is the altitude of maximum production for zero solar zenith angle and H is the scale height. Adapted from Brekke (2013).

The decrease in density arises because, in the absence of other external forces, a gas under

gravity naturally decays according to an exponential law as the mass of the atmosphere above a given altitude compresses the gas beneath it.

The decrease in photon flux depends on the distance the solar flux travels which makes it dependent on incidence angle. To understand the dependence of ionization upon incident angle, the theory considers the atmosphere as a series of shells of increasing altitude. Light with a zero incidence angle travels the least distance between shells and as the angle from zenith increases so does the distance travelled between shells. As the distance traversed between shells increases, more light is absorbed thus decreasing the intensity reaching the next shell. Ionization rates depend on both the intensity of light at the required wavelengths and the particle density of the gases present, thus connecting the two effects.

1.2.3 F1 Layer

The F region is further subdivided into layers for study, the first of which is called the F1 layer. The F1 layer is a layer that is commonly present during daytime but is rare during the night. Its creation is related to the photo-ionization of the atmosphere. Although the layer is located at heights of efficient electron-ion pair production, the layer is still weak for the following reason. It is believed that the F1 layer is formed at heights where a transition from alpha type recombination processes to beta type processes occur (Brekke, 2013), Equations 1.10 and 1.11. An F1 layer is seen if the maximum photo-ionization is below the height of this transition between the dominant recombination types. A standard Chapman profile would apply to the heights below the maximum in production, and immediately above it, but eventually, at much larger heights, beta type processes would be faster than the alpha processes, so that electron density would start decreasing. This would indicate occurrence of a "bump" or "ledge" in the electron density profile. If the altitude of the maximum photo-ionization is above the alpha-to-beta type recombination transition region, then no such decrease in the electron density would appear and no "ledge" (F1 layer) would be seen (Brekke, 2013).

Since the altitude of maximum production is dependent on the solar zenith angle (Figure 1.5), such that high solar zenith angles result in higher maximum production altitudes, the F1 layer does not occur at high solar zenith angles. As the solar zenith angle decreases after local noon, the height of maximum production decreases and an F1 layer is formed.

1.2.4 F2 Layer

The F2 layer does not occur at the altitude of the photo-ionization maximum. Instead, the layer is usually above it. The layer occurs owing to a faster reduction in the recombination

rate compared to the reduction in the photo-ionization rate, as both decrease with altitude. The electron density increases almost exponentially with altitude above the F1 layer height until such an altitude where diffusion starts to dominate, producing a subsequent exponential decrease in the electron density with altitude. Thus, it may be stated that the F2 layer is being photo-chemically controlled below the electron density peak and being diffusion-controlled above the electron density peak. The delicate equilibrium required for the F2-layer formation explains why this layer is extremely sensitive to changes in neural particle composition, notably the ratio of atomic oxygen to molecular nitrogen, O/N_2, the major constituents at F region heights.

1.2.5 Topside Ionosphere

In the lower topside, just above the F region peak, O^+ ions dominate and they decay roughly according to the exponential law. However, at larger heights, He^+ and H^+ ions become more important and the electron density starts to decay at a slower rate. This is evident in electron density profiles as "stabilization" of the electron density decay occurs at heights greater than 500 km.

1.2.6 Winter Anomaly

The standard Chapman model of the ionosphere formation expects that the maximum electron density in the ionosphere is achieved at the time of the highest solar zenith angle. At middle latitudes, this would be near noon summer solstice time. However, it has long been known through ionosonde observations that the maximum daytime electron density is achieved in winter and not in summer at middle latitudes (Torr & Torr, 1973; Zou et al., 2000). This is referred to as the winter anomaly. The effect is particularly strong in the North American sector (Yasyukevich et al., 2018). Although the exact reasons for the effect are still under debate, most researchers relate it to seasonal changes in neutral composition (the ratio O/N_2) that are greater in winter than in summer (Yasyukevich et al., 2018). These changes are due to global thermosphere circulation with the strongest downwelling zone being just equatorward of the auroral oval in winter. In the North American sector, the geographic latitude of this zone has larger magnetic latitude, and thus larger cosine of zenith angle, as compared to other sectors, and so the electron density is enhanced. To what extent these processes can affect higher altitude plasma has not been discussed in the literature, to the best of the author's knowledge.

1.3 E-CHAIM model of the electron density in the high-latitude ionosphere

The Empirical Canadian High Arctic Ionospheric Model (E-CHAIM) has been developed with the ultimate goal of replacing the classical International Reference Ionosphere (IRI) model (e.g., Bilitza, 2018) for high latitudes (Themens, 2018; Themens et al., 2017). The model is introduced below following the original description given by the model developer, Dr. D.R. Themens (Themens, 2018).

The model targets latitudes above 50° N geomagnetic latitude. It was created using the Altitude-Adjusted Corrected Geomagnetic (AACGM) coordinates as given by Shepherd (2014), calculated at 350 km altitude. First, the model was developed for the peak electron density N_mF2 and its height h_mF2 (Themens et al., 2017). Then several sub-models were included. They represent the electron density profile above (Themens, 2018) and below the F region peak (Themens, Jayachandran, McCaffrey, et al., 2019) while the peak density and its height act as the anchor points for the model. The dataset for the model consists of ionograms from 81 ionosondes, including those operated in the Canadian sector of the Arctic. Radio Occultation (RO) data were used as well (Themens, 2018).

For the model of N_mF2, over 28 million data points were used in the fitting of the quiet-time portion of the model, spanning seven solar cycles between 1931 and 2016 (Themens, 2018). The data were fitted by multiple linear regression (e.g., ordinary linear least squares) to a spherical cap harmonic function with Gauss coefficients tied to a Fourier expansion in day-of-year (DoY)" (Themens, 2018). The maximum degree and order for the spherical cap harmonic expansion were optimized via trial and error to be five and four, respectively. This selection was based by judging that seasonal variations of the electron density in the polar cap are reproduced, something that was missed in the previous models. This expansion resulted in 488 coefficients.

It should be noted that the fitting procedure also considered the dependence on the solar zenith angle and solar activity level. Solar activity level was represented by the F10.7 cm solar radiation flux and the so-called IG index, which is a monthly ionospheric index derived from a selection of global ionosonde measurements of of critical frequency f_0F2. The IG index monitors differences between the peak electron density at current conditions with respect to a highly-averaged reference map. This index better characterizes solar cycle variations in the electron density (Themens, 2018).

To represent diurnal variability, the model was composed of 24 separate models (e.g. 24 separate sets of spherical cap series) fitted to data binned in UT time. To get N_mF2 at a

given point in time, linear interpolation between the models was used. The series expansion in terms of geomagnetic longitude allows the model to slightly better reflect the variability within each hour of magnetic local time. This variability is not captured by the models that use expansions in geographic coordinates.

Validation of the E-CHAIM model was by building an additional data set from CADI observations at Resolute Bay, Alert, Eilson and Cambridge Bay, all in Canada (Themens et al., 2017). Seasonal variation was found to be well represented. The criterion for assessing improvements was that the standard deviations of the E-CHAIM model from measurements is better than for other models. The E-CHAIM model was later adjusted to reflect magnetic storm effects, in particular at the lowest considered latitudes.

The E-CHAIM model for the heights below and above the F region peak were developed in a similar way with some additional caveats (Themens et al., 2018; Themens, Jayachandran, McCaffrey, et al., 2019).

1.4 Objective of the thesis work

This thesis is aimed at investigation of the electron density distribution in the high-latitude ionosphere and techniques for electron density measurements. The focus is on one specific area in the Canadian Arctic, the vicinity of Resolute Bay, Nunavut. This region was selected because combined studies with ground-based incoherent scatter radars (ISRs) and instruments onboard the Swarm satellites (e.g., Buchert et al., 2015; Knudsen et al., 2017) is possible. It is important to realize that this area is monitored with three coherent scatter Super Dual Auroral Network (SuperDARN) high-frequency radars at Rankin Inlet, Inuvik and Clyde River, providing information on the global-scale $\vec{E} \times \vec{B}$ drift of ionospheric plasma (e.g., Chisham et al., 2007; Nishitani et al., 2019). Electron density distribution in the ionosphere is a major factor affecting the occurrence of HF echoes and thus knowing it is critical for assessing SuperDARN radar performance both as it is collected and for forecasting of future experiments (Ullrich, 2021).

Specific goals of this thesis are as follows:

1. Assessing quality of electron density measurements by Langmuir probes onboard the Swarm satellites and identification of differences in measurements between two of the satellites that are travelling closely in time and space. The measurements were performed in the topside ionosphere, which is a region of the ionosphere poorly understood because measurements at these heights are difficult to perform. Consequently, these heights have not been well studied. One goal is to understand the reasons for minor differences

between the electron density values reported by Swarm A and Swarm C. Another long-standing question is whether one can identify the occurrence of polar cap patches by comparing nearly simultaneous electron density measurements made by the two satellites.

2. Assessing the long-term trends in the variation of the topside electron density by considering measurements with the three Swarm satellites passing close to Resolute Bay. Seasonal and solar cycle variations are targeted. A complementary goal is to establish similarities and differences in the electron density variations with predictions of the E-CHAIM ionospheric model.

3. Comparing the electron density in the topside high-latitude ionosphere as measured by the Swarm satellites and by ISR radars independently monitoring the electron density at comparable heights. Data from two incoherent scatter radars operated at Resolute Bay were to be considered.

4. Establishing the extent to which the E-CHAIM ionospheric model predicts the electron density at various heights, from the bottom to the top, over Resolute Bay by comparing model values and measurements by ISRs locate at Resolute Bay.

1.5 Thesis Outline

The thesis is organized as follows. In Chapter 2, principles of electron density measurements in the ionosphere with ISRs and the Langmuir probes on the Swarm satellites are discussed. Chapter 3 investigates topside electron density measurements with Swarm satellites and compares the Swarm measurements with predictions of the E-CHAIM ionospheric model. Chapter 4 considers nearly simultaneous ISR-Swarm measurements and investigates the compatibility of the instruments in the topside ionosphere. Chapter 5 evaluates the quality of the E-CHAIM ionospheric model predictions for the Resolute Bay area at various heights by comparing with ISR data. Chapter 6 summarizes obtained results and gives suggestions for future work.

Chapter 2

Instrumentation

As outlined in the previous chapter, the main topic of this thesis is the electron density distribution in the high-latitude ionosphere.

The electron density of the ionosphere can be measured using multiple types of instruments. Traditionally used instruments are ionosondes and incoherent scatter radars (Beynon & Williams, 1978; Davis, 1990; Hargreaves, 1992; Hunsucker, 1991; Rawer, 2013). Recently, receivers on the ground detecting signals from global navigation satellite systems such as GPS have became popular (e.g., Huang et al., 2015; Themens et al., 2021). In space, in-situ Langmuir probes have been used successfully (Chartier et al., 2018; Jin et al., 2019; Kakinami et al., 2008; Lebreton et al., 2006; Lee et al., 2013). Over the last two decades, radio occultation measurements from low-orbiting satellites have provided significant information on the global electron density distribution in the ionosphere (e.g., Hocke & Igarashi, 2002). Recently, it was proposed that elevation angle measurements with the SuperDARN HF radars allow estimates of the peak electron density in the ionosphere (e.g., Ullrich, 2021).

In this chapter the principles of operation and details of instruments used in this thesis, an incoherent scatter radar (ISR) and a Langmuir Probe (LP) placed on board Swarm satellites, are described. Further details on specifics for the conditions of observations relevant to this thesis are given in individual Chapters 3 to 5.

2.1 Incoherent Scatter Radars

ISRs are among the most powerful and versatile instruments for diagnostics of the ionospheric plasma (e.g., Beynon & Williams, 1978). Their advantage is their ability to provide data continuously, without interruption, and to cover ionospheric heights between ~100 and ~600 km with spatial resolution from tens of kilometres to hundreds of meters, depending on the mode of operation. The time resolution of modern ISRs is 1 to 5 min. One disadvantage of ISRs is their high cost of operation, although low-resolution modes provide data of good quality for not much expense.

The following description of the operation of ISRs is based the books *The Solar-Terrestrial Environment* (Hargreaves, 1992), *The Earth's Ionosphere* (Kelley, 2009), *Ionospheres : physics, plasma physics, and chemistry* (Schunk & Nagy, 2009) and the Master's thesis "Study of the Polar Cap Plasma Flows With the Clyde River SuperDARN Radar" (Bankole, 2019).

2.1.1 Principles of ISR

ISRs operate by transmitting high-power pulses along narrow beams and analyzing weak signals scattered by the ionosphere. VHF and UHF frequencies are used because narrow beams can be made at such frequencies, which allow angular resolutions as low as ~1° . Range resolution, which is spatial resolution along the beam, is determined by the pulse length of the radar. A standard beam resolution for what are called long pulses is 50 km in range. However, modern ISRs employ frequency modulation or other encoding techniques to improve range resolution independent of pulse length. By integrating any received signals over a time period and using high powered pulses, even weak scatter from thermal fluctuations can be recovered. Individual measurements along a beam path are typically called range-gates.

Multiple pulses received by ISRs are analyzed in the time domain. The autocorrelation function (ACF) of pulses for various time lags is evaluated. The information from ACFs allows one to obtain the full spectrum of returned signals by applying the Fourier transform. Figure 2.1 is a sketch of a spectrum of signals received by ISRs.

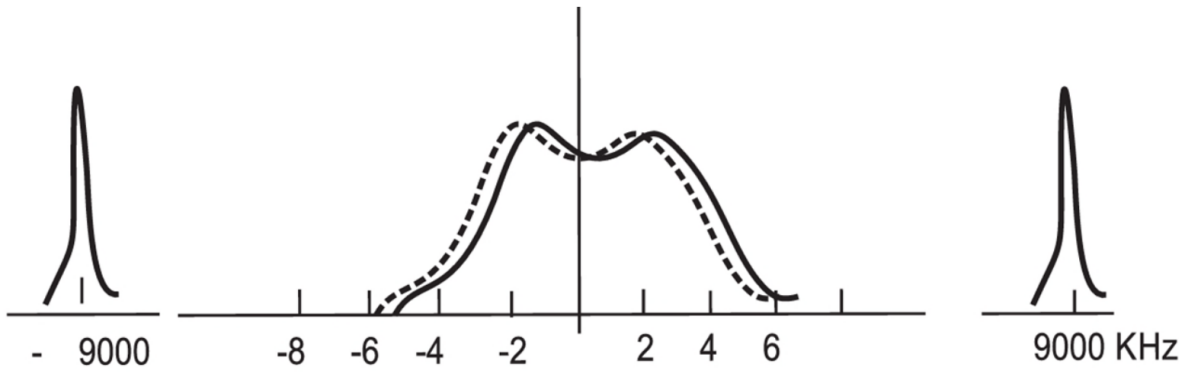

Figure 2.1: Sketch of a typical spectrum of a signal received by ISRs (solid line). Dashed line depicts a spectrum without Doppler shift. Image courtesy of A. Koustov.

The spectrum of the scattered signal has two major components. The first one is related to the motion of electrons at the plasma frequency, which is related to the electron density (Equation 1.1). However, the electron component is often very weak and not detected.

The second component is related to the motion of ions involved in ion-acoustic waves in plasma. This component is termed the ion line. The ion line is routinely analyzed as it is much stronger than the electron component. Because ion-acoustic waves decay quickly and are weak on average, integration times of over a minute are required to obtain a robust, well defined spectrum. The quality of the spectrum determines the errors in measurement. A longer integration time reduces uncertainty at the cost of temporal resolution.

Multiple plasma parameters can be related to the scattered spectrum. Among the parameters that can be determined are the ion-electron temperature ratio, the electron density and Doppler shift.

The ion component of the spectrum spans several kHz, and has double peaks, one on each side of the spectrum's centre. The saddle point between the peaks is related to the ion-electron temperature ratio and, thus, is used to measure the ratio. The power of the spectrum is proportional to the electron density in the scattering volume.

A third plasma parameter that can be found by analyzing the ion line spectrum is the spectrum Doppler shift in frequency. The Doppler velocity of the returned signal is the line-of-sight component of the $\vec{E} \times \vec{B}$ plasma flow in the volume of ionosphere the radar is aimed at. Figure 2.1 shows an un-shifted signal (dashed line) and the received signal (solid line).

By combining data from two or more ISR beams, the plasma velocity vector in the plane perpendicular to the magnetic field can be reconstructed. This allows for remote observation of plasma motion patterns and intensity, which is critical for understanding ionosphere dynamics.

In modern ISR processing software, a non-linear least squares fitting of the ion line is performed to infer all three parameters, electron density, Doppler shift and electron-to-ion temperature ratio, at once. ISRs provide a good measure of the difference in the electron density between various heights but to obtain the absolute value of the electron density the measurement needs to be calibrated. If the electron line spectrum is available the instrument can be self-calibrated. Routinely, however, an independent instrument is used, usually an ionosonde co-located with the ISR.

2.1.2 Resolute Bay ISRs (RISR radars)

Data from two ISR installations at Resolute Bay, Nunavut (Canada) are used in this thesis, RISR-North (RISR-N) and RISR-Canada (RISR-C). Figure 2.2 gives a panoramic view of the radar transmit-receive faces, which are sloped at about 45° with respect to the horizontal plane. Data processing buildings are nearby. The electric power generator is seen to the left

of the maintenance building in between the faces.

Figure 2.2: Panoramic view of the Resolute Bay RISR-N (left) and RISR-C (right) radar transmit-receive panels. The image is taken from https://aurora.phys.ucalgary.ca/resu/index.html on 28 October 2021.

A detailed description of RISR-N and RISR-C is given in Bahcivan et al. (2010) and Gillies et al. (2016), respectively. The RISR radars are modular systems with transmit-receive antennas consisting of 121 sub-panels each being composed of 32 individual antennas ("RISR information", 2016). By phasing the panels, the radar beam can be re-targeted allowing the radar to complete measurements for up to 51 beams in less than a minute.

Figure 2.3 gives the field of view (FoV) of both radars at a height of 300 km. Here the centers of all the possible range-gates are mapped down onto the horizontal plane. RISR-N looks towards the magnetic pole while RISR-C looks in the opposite direction, toward the Canadian mainland. The "maple leaf" pattern of the monitored areas is essential for achieving coverage in both the north-south and east-west directions, which is essential for derivation of 3-D patterns of the electron density distribution and the $\vec{E} \times \vec{B}$ plasma flow vectors.

The radars operate at ~440 MHz, a frequency that gives an index of refraction of close to 1 for typical plasma parameters (Schunk & Nagy, 2009). This allows the radar to avoid problems with the location of the scattering volume due to radio wave refraction in the ionosphere. It also avoids the slowing of the radio waves in the magneto-plasma. Both issues are critical for other radars such as SuperDARN HF radars and for ionosondes (Gillies et al., 2016; Hunsucker, 1991). The radars are capable of transmitting up to 500 Watts from each individual element, resulting in 1-2 MW of total power for each installation. The radars operate on a duty cycle of ~6% when both are working ("RISR information", 2016), with pulses of 330 microseconds (Gillies et al., 2016). The height of measurement depends on

the beam orientation and mode of operation but, in general, it measures from 100 to 600 km. The lower bound of the range does not consistently cover the E region, which presents significant difficulties in using RISR data for E region studies.

The RISR radars can work in several modes, but the most common are World Day (WD) mode and Imaging modes. World day mode takes measurements along 11 beams and Imaging mode uses 51 beams. Raw instrument readings are processed and made available with one minute and five minute integration times. Both data sets are used in this thesis, however, the focus is on the five minute data because longer integration time reduces the uncertainty in the data.

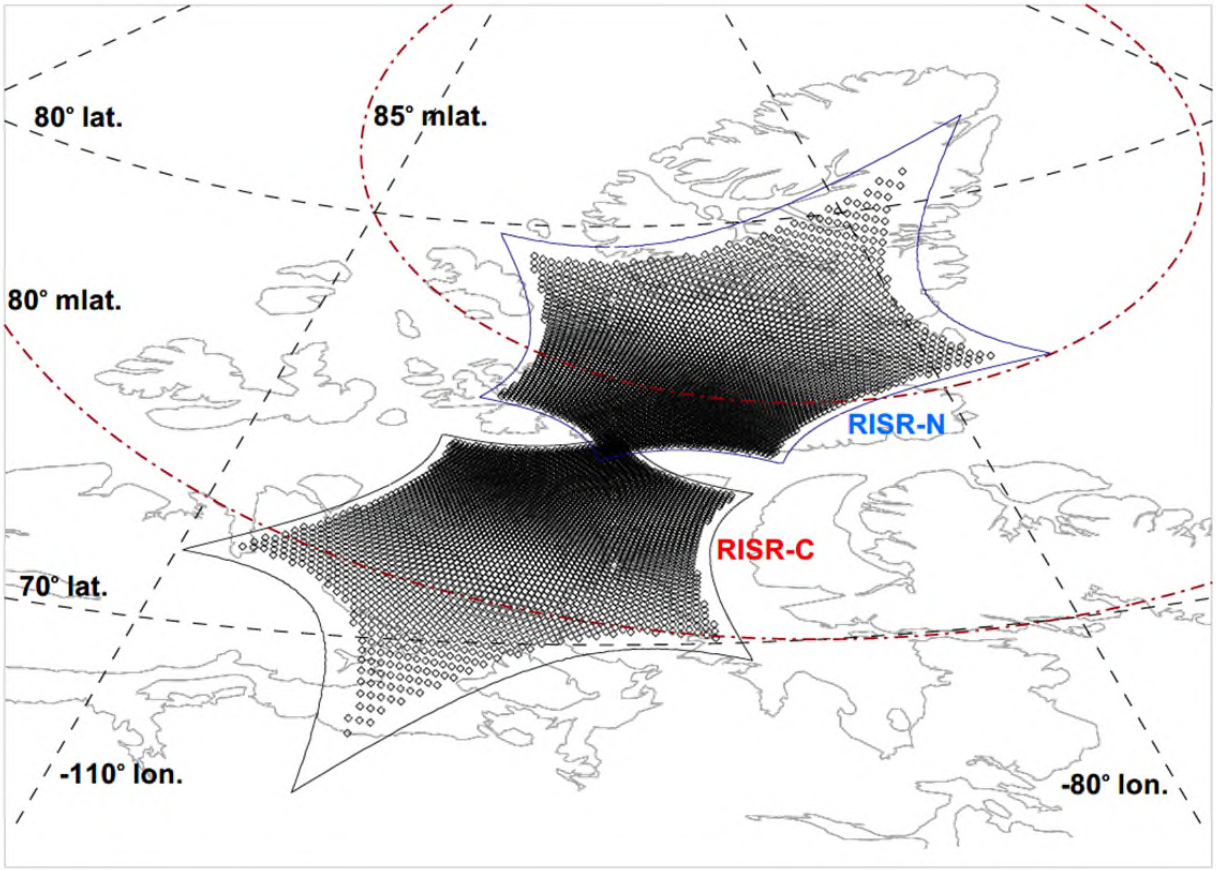

Figure 2.3: The field of views of the RISR-C and RISR-N incoherent scatter radars. The diamonds represent the locations of the ionospheric pierce points at 300 km. All beams of the systems are considered. North of ~75° latitude are RISR-N points while south of ~75° are RISR-C points. The diagram was produced by Dr. Gillies, University of Calgary.

Figure 2.4 gives an example of electron density measurements from the RISR-C radar in a WD experiment mode between 5 -7 March 2016. Records in beam 5 are presented along with the beam number and orientation (azimuth and elevation angles). For Resolute Bay,

local midnight is at 06 UT and local noon is at 18 UT. One can see the electron density decreases toward midnight, while the peak electron density shifts to a larger height. With the sunrise, the electron density recovers to reach maximum densities in the afternoon hours. The midnight to noon profile is rather flat at the heights above 250 km. With the exception of the hours just before and after noon, density decreases sharply below 200-250 km. Several electron density enhancements (separated by ~20 minutes) are seen near the noon hours.

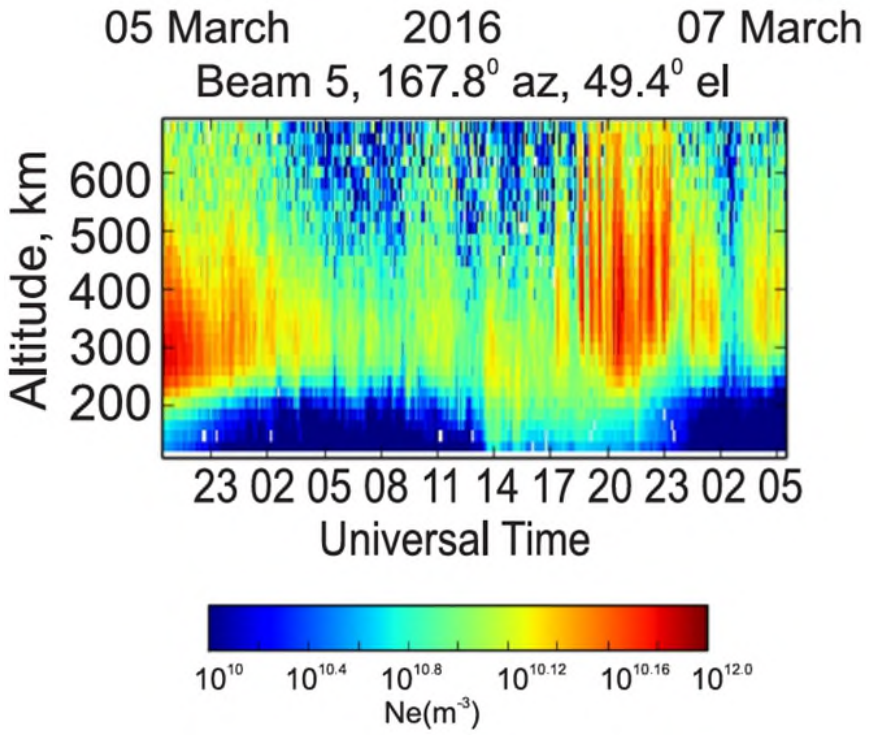

Figure 2.4: The standard RISR plot of the electron density at various ionospheric heights versus universal time (UT) as measured by the RISR-C radar in beam 5 in the Word Day experiment mode run between 05 and 07 March 2016. Image credit: Donovan (2016).

For ISRs operating in the polar cap, an issue of special concern is the errors in measurements. This is because the ionosphere here is often weak, especially the topside, and this requires longer integration time to achieve better ACF fits of the integrated signals, in order to reduce uncertainty in the integrated measurements. Although longer integration time data can be obtained upon request and for special experiments, the data are regularly distributed with 1 or 5 (or, less common, 3) minute resolution time. The errors are of a concern in this thesis because the validity of the projects undertaken are ultimately dependent on the quality of the RISR measurements. One of the issues to be discussed is a comparison of RISR electron density measurements with Swarm in-situ measurements in the topside ionosphere for spatially and temporally concurrent observations. To this end, an analysis

of the typical errors for RISR measurements was undertaken and is presented in Figure 2.5. The database here is for all concurrent measurements between Swarm satellites and RISR-C observations in the period from 2014 to 2018.

Figure 2.5a shows that typical absolute error is on the order of (2-3)$\times 10^{10}$ m^{-3}, with the range increasing at lower densities. Although this seems to be a small number, one has to keep in mind that the absolute value of the electron density at 450 km is not high (see Figure 1.1). Figure 2.5b shows the typical relative error, error/absolute value, in RISR-C measurements. Clearly, at low electron densities relative errors can be more than 200%. It should be noted that relative errors at lower heights (except of very bottom side) are not as large as those shown in Figure 2.5b. For the projects in this thesis, the decision was made not to consider the RISR measurements with relative error above 50%. More restrictive conditions were found to limit the database dramatically.

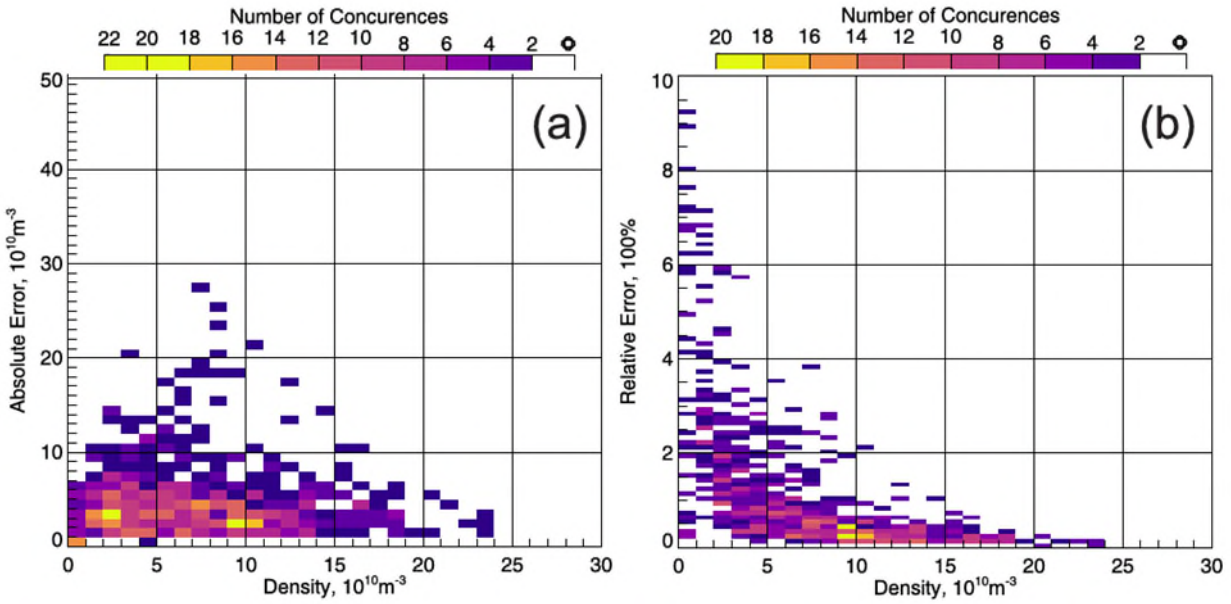

Figure 2.5: (a) Scatter plot of errors in RISR-C measurements of the electron density versus absolute value of measured electron density. The entire database of joint Swarm A/C and RISR-C observations in the World Day mode (see details in Chapter 4) were considered. (b) The same as (a) except for relative errors in RISR-C measurements (error/value).

2.1.3 Data Source

Processed RISR-C/N data were downloaded from http://madrigal.phys.ucalgary.ca. Additional processed RISR-N data for 2014 were downloaded from http://isr.sri.com/madrigal/cgi-bin/gSimpleUIAccessData.py. In both cases, electron density was provided.

2.2 Principles of Swarm LP operation

The following description of the operation of a Langmuir probe is based on a paper by Merlino (2007), a book by Schunk and Nagy (2009) and a paper by Mott-Smith and Langmuir (1926).

2.2.1 General introduction

The Langmuir probe is an instrument used to measure plasma density and electron temperature. The probe is a conductive metal in the shape of a cylinder, sphere or disk that is placed inside a plasma. The probe is operated by applying a varying bias and measuring the current through the probe. The plasma potential, plasma density and electron temperature are then obtained from the resultant current-voltage, or I-V, curve as originally suggested by Mott-Smith and Langmuir (1926).

2.2.2 IV curve and density/electron temperature derivation

Probe potentials

Initially it was assumed that simply inserting a conductor into a plasma would be sufficient to measure the plasma potential, which is the potential of the plasma surrounding the probe. However, an unbiased probe inserted into plasma assumes a floating potential V_f, which is usually negative relative to the plasma potential, V_p (Merlino, 2007). The key insight of Mott-Smith and Langmuir was that the floating potential could not be neglected.

The floating potential arises because the mass of an electron is smaller than the mass of an ion and therefore electrons have a higher thermal velocity than ions at the same temperature. For this reason, electrons collide with the probe more frequently than the ions, and the electrons collect on and near the surface of the probe. This effect is enhanced when electron temperatures are higher than ion temperatures, which is normally the case (Merlino, 2007). Thus, the probe assumes a negative V_f relative to V_p so that there is zero net current. The negative V_f repels electrons and attracts ions until an equilibrium is met. The result is the formation of a sheath, or cloud, of positive ions surrounding the probe that compensates for the difference between V_f and V_p. A sketch of such a cloud around a spherical probe is given in Figure 2.6. Thus, an unbiased conductor inserted into plasma does not measure V_p and the electrical properties of the plasma cannot be directly determined.

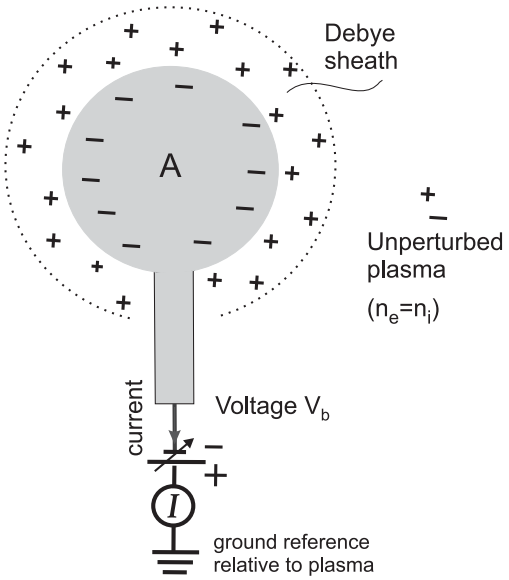

Figure 2.6: Schematic of a biased spherical Langmuir probe with Debye sheath indicated. Image adapted from (Bhattarai & Mishra, 2017).

In order to quantify the difference between V_f and V_p , Langmuir and Mott-Smith suggested the application of a bias to the conductor and sweeping the bias through a range of potentials to obtain an I-V curve. The physical processes of the operation of a biased probe are similar to that of a free floating probe in that a sheath of charged particles still forms around the probe. However, the probe bias V_b, relative to V_p, determines which species of particles form the sheath. In addition to the difference in collision rates, the difference in mass between electrons and ions also results in V_b accelerating the electrons faster than the ions. If $V_b > V_p$ the electrons are attracted to the probe and form the sheath, while positive ions are repelled. When there is a sufficient negative bias, that is $V_b < V_p$, the electrons are repelled by the probe and the positive ions are attracted, and ions form the sheath. In either case, the sheath still forms such that it shields the remaining quasi-neutral plasma from the probe (Merlino, 2007). The shielding effect in a plasma sheath is characterized by the Debye length of the plasma, which is given by

$$\lambda_D = \sqrt{\frac{\varepsilon_o k_B T_e}{n_e e^2}} \tag{2.1}$$

where ε_o is the permittivity of free space, k_B is the Boltzmann constant, T_e is the electron temperature, n_e is the electron density and e is the elemental charge.

Currents

The key difference between a floating probe and a biased probe is that, as V_b is varied, a current flows through the probe. The current magnitude depends on the difference between V_b and V_p, the probe geometry, the velocity distribution, the charge density and the temperature of the plasma in the sheath. The Debye length is a factor in the equations describing the motion of the particles near the probe and the total charge surrounding the probe. Since current is the motion of charge through an area, i.e. the flux of charge, the Debye length cancels when deriving the current equations and does not appear in the description of the ideal probe (Mott-Smith & Langmuir, 1926). In practice, the sheath expands with increasing magnitude of V_b and probe current deviates from the theoretical ideal (Merlino, 2007). Magnetic fields and the relative velocity of the plasma and the probe also affect the current in physical probes (Schunk & Nagy, 2009). In order to simplify the equations and explanations a standard Maxwellian distribution is assumed and sheath expansion, magnetic fields and relative velocities are neglected. In addition, the presence of negative ions is neglected and all ions are assumed to have a positive charge.

The difference between V_b and V_p defines three current regions, which are the ion saturation region, the electron retarding region, and the electron accelerating region. A sketch of the regions and the current-voltage relationship is given in Figure 2.7.

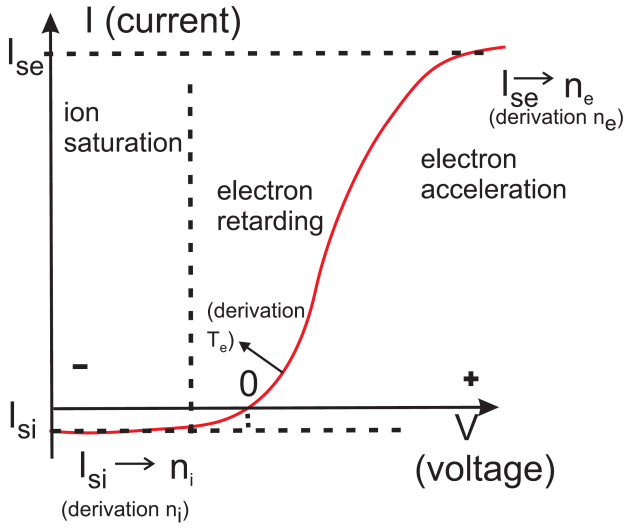

Figure 2.7: Probe current as a function of probe bias, with the three current regions indicated. The point at which electron temperature can be measured is indicated by T_e. (Adapted from Schunk & Nagy, 2009).

When $V_b > V_p$, the sheath is populated by electrons and the probe is operating in the accelerating region current where the electron current dominates. In the ion saturation region,

V_b<V_p, the sheath is populated by positive ions and the ion current dominates. Between the accelerating and saturation regions, when the difference between V_b and V_p is small, the probe operates in the electron retarding region and both the electron and ion currents are present.

With the assumption of a Maxwellian velocity distribution, the current for both electrons and ions can be described by the same set of equations (Mott-Smith & Langmuir, 1926). For regions where a given species of particle dominates the sheath such that the current saturates, the expression for the current is given by

$$I_{\alpha s} = e n_\alpha v_{\alpha,th} A \tag{2.2}$$

where α is either e for electrons or i for ions, $v_{\alpha,th}$ is the thermal velocity of the particle, and A is the surface area of the probe. The thermal velocity for particles in a Maxwellian distribution is given by

$$v_{\alpha,th} = \sqrt{\frac{2k_B T_\alpha}{m_\alpha}} \tag{2.3}$$

where m_α is the particle mass. An important exception to Equation (2.2) occurs when $T_e \gg T_i$, in which case the ion saturation current becomes

$$I_{is} = 0.6 e n_i \sqrt{\frac{k_B T_e}{m_i}} A \tag{2.4}$$

which is called the Bohm current (Merlino, 2007). The dependence of the ion saturation current on electron temperature arises because at high electron temperatures electrons collide with the sheath with enough frequency to disrupt the formation of a positive sheath unless the ions have a greater velocity than the electrons (Merlino, 2007).

The current saturates because it is limited by the rate of charged particles reaching the sheath (Merlino, 2007; Mott-Smith & Langmuir, 1926). When a given species is not saturated, the current is modified by an exponential term

$$I_\alpha = \pm I_{\alpha s} \exp[\pm e(V_b - V_p)/k_B T_\alpha] \tag{2.5}$$

where, by convention, the electron current is positive while the ion current is negative (Merlino, 2007). The current in all regions is a combination of the non-saturated and saturated currents of both ions and electrons which gives the following set of equations to describe the current in all three regions

$$I = \begin{cases} -I_{is} + I_{es}\exp[-e(V_p - V_b)/k_B T_e], & V_b \ll V_p \quad \text{Ion Saturation} \quad (2.6) \\ -I_{is}\exp[e(V_p - V_b)/k_B T_i] + I_{es}\exp[-e(V_p - V_b)/k_B T_e], & \text{Elec. Retarding} \quad (2.7) \\ -I_{is}\exp[e(V_p - V_b)/k_B T_i] + I_{es}, & V_b \gg V_p \quad \text{Elec. Accelerating} \quad (2.8) \end{cases}$$

In the ion saturation and electron accelerating regions the exponential terms both have negative exponents and for large biases the associated currents decay to zero, leaving a constant saturation current. In practice, the increase in sheath radius with bias allows some increase in the saturated current (Merlino, 2007). The ion current is generally weaker than the electron current, due to the larger mass of ions giving them a smaller thermal velocity and consequentially a smaller saturation current (Merlino, 2007). Thus, the current in the electron retarding region is more strongly dependent on the electron current than the ion current. Equations (2.2), (2.3) and (2.5) can be combined to give

$$I_\alpha = \pm e n_\alpha A \sqrt{\frac{2k_B T_\alpha}{m_\alpha}} \exp\left(\pm \frac{e|V_p - V_b|}{k_B T_\alpha}\right) \quad (2.9)$$

as the general expression of the decaying current, which more clearly shows the connection to temperature and electron density (Merlino, 2007; Schunk & Nagy, 2009).

Density

Electron density is normally calculated using the saturated current, given by Equation (2.2), at the transition point between the electron retarding region and the electron accelerating region or it is calculated in the electron accelerating region (Merlino, 2007). In the accelerating region, the relationship between current and potential is dependent on probe geometry (Bhattarai & Mishra, 2017). For a spherical probe the current is given by the sum of the kinetic and electrical energy of the electrons

$$I_e = e n_e \sqrt{\frac{2k_B T_e}{m_e}} A \left(1 + \frac{e(V_p - V_o)}{k_B T_e}\right) \quad (2.10)$$

where A is the surface area of the probe that is exposed to plasma (Diego et al., 2017). If the plasma voltage is assumed to hold constant during a sweep of the probe potential from negative to positive, and the electron temperature is known, then Equation (2.10) can be solved for the electron density.

2.2.3 Swarm specific features of LP probes

For Langmuir probes installed on spacecraft additional considerations arise. The floating potential, sometimes called the spacecraft potential V_s, can reach values as low as -10 V (Schunk & Nagy, 2009) causing a horizontal shift in the I-V curve (Knudsen et al., 2017). Consequently, valid measurements require determination of V_s. Another consideration is that current induced by photo-electrons is present (Knudsen et al., 2017; Schunk & Nagy, 2009), although the photo-current can be eliminated with the appropriate measurements and analysis (Knudsen et al., 2017). Finally, for spacecraft in low-Earth orbits, the ion saturation current depends not on the thermal energy of the ions, but on the collisions of ions with the satellite. Consequently, in Equations (2.3) and (2.5) through (2.9) the thermal energy $k_B T_i$ is replaced with

$$k_B T_i \rightarrow E_i = \frac{1}{2} m_i u_i^2 \tag{2.11}$$

and the area used is the cross-section of the probe and not the surface area of the probe.

The three original Swarm satellites, Swarm A, B and C, each have two 4 mm radius spherical Langmuir probes (Knudsen et al., 2017). One probe is nitrated titanium and the other is gold, with the difference between the two probes intended to be the focus of study (Knudsen et al., 2017). In order to prevent the electric field of the spacecraft from interfering with the measurements, the probes are extended from the satellite bodies by 8 cm posts (Knudsen et al., 2017). Figure 2.8 shows the location of the probes on one of the Swarm satellites.

With adjustments for the spherical geometry of the probes and the low Earth orbit of Swarm, the current in the Swarm LPs is described using

$$I = \begin{cases} -en_i u_i A_c \left(1 - \dfrac{eV}{E_i}\right), & V \ll V_p \quad \text{Ion Saturation} \quad (2.12) \\ -en_i u_i A_c \left(1 - \dfrac{eV}{E_i}\right) + en_e A \sqrt{\dfrac{2k_B T_e}{m_e}} \exp\left(\dfrac{eV}{k_B T_e}\right), & \text{Elec. Retarding} \quad (2.13) \\ en_e A \sqrt{\dfrac{2k_B T_e}{m_e}} \left(1 + \dfrac{eV}{k_B T_e}\right), & V \gg V_p \quad \text{Elec. Accelerating} \quad (2.14) \end{cases}$$

where $V = V_b + V_s$ is used to simplify the expressions (Knudsen et al., 2017). The measurement method used by Swarm also makes use of the derivatives of Equations (2.12) to (2.14). The derivatives are related to the electrical properties of the probe by Ohm's law for alternating current

$$I = YV = Y(V_b + V_s) \tag{2.15}$$

which relates current, voltage and admittance, Y. Differentiating Equation (2.15) with respect

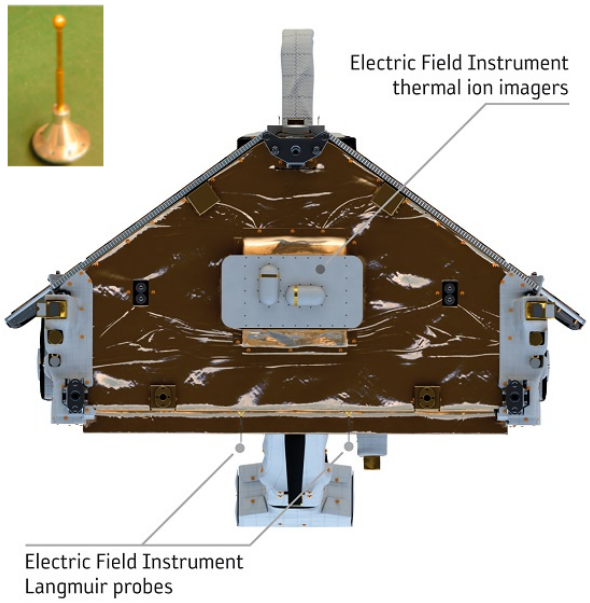

Figure 2.8: Langmuir Probe installation on a Swarm satellite ("EFI instrument - Swarm - ESA Earth Explorer Missions - Earth Online - ESA", 2020). Top Left: an image of a Langmuir probe used on a Swarm satellite, adapted from Knudsen et al., 2017.

to voltage gives

$$Y = \frac{\mathrm{d}I}{\mathrm{d}V} \tag{2.16}$$

showing that admittance is the derivative of current with respect to voltage.

As detailed by Knudsen et al. (2017), the Langmuir probes used on Swarm operate in two modes. The first is a standard sweep of one second every 128 seconds. For the remaining 127 seconds the probes operate using a harmonic mode. The harmonic mode uses three bias points, one located in each of the three current regions, and applies a sinusoid modulation of 128 Hz to 4 kHz to each bias point. The magnitude and frequency of the modulation can be changed which allows the complex admittance, in addition to the current, to be obtained. When measuring in this mode, Swarm uses 10 cycle averages and 100 ms of modulation (Knudsen et al., 2017) which allows the assumption that V_b is constant over a single measurement.

By also holding bias V_b constant, admittance Y can then be determined using Equation (2.15). Thus, by measuring current and admittance for a given bias voltage the electron density, electron temperature and spacecraft voltage can all be derived.

This is done as follows, electron density is measured directly from admittance in the ion

saturation region, using the derivative of expression (2.12)

$$Y_{is} = e^2 n_e u_i A_c / E_i \tag{2.17}$$

with the assumptions that ion thermal energy is negligible and that electron density and ion density are equivalent. This removes the dependence of electron density on electron temperature.

The spacecraft potential is found by dividing Equation (2.14) by its derivative Y_{acc}

$$V_s = \frac{I_{ret}}{Y_{ret}} - V_{acc} - \frac{k_B}{e} T_e \tag{2.18}$$

and using the more complicated expression

$$V_s = -\frac{I_{acc} - I_{ret} + Y_{ret} V_{ret} - Y_{acc} V_{acc}}{Y_{ret} - Y_{acc}} \tag{2.19}$$

when densities are low (Knudsen et al., 2017).

2.2.4 Data Source

The Swarm data used in this thesis are classified as "level1b", calibrated electron density readings at 2 Hz provided by the European Space Agency. The data were downloaded from swarm-diss.eo.esa.int.

2.3 Summary

This Chapter introduced the two instruments that collected the data that are used in this thesis. RISR-C and RISR-N are incoherent scatter radars, which collect data on electron density by analyzing the spectrum of backscattered radar pulses. The Swarm satellites, Swarm A, B and C, have Langmuir probes that collect data on electron density by analyzing the changes in probe voltage in response to changing plasma density as the satellites orbit.

Chapter 3

Topside electron density over Resolute Bay as measured by the Swarm satellites and predicted by the E-CHAIM ionospheric model

In this chapter, we assess long-term trends in variations of ionospheric electron density in the Resolute Bay area by investigating the topside electron density as measured by the Swarm satellites and as predicted by the Empirical-Canadian High Arctic Ionospheric Model (E-CHAIM, Themens et al., 2017). The topside ionosphere is comparatively under researched (Kutiev et al., 2013) and represents an opportunity for meaningful research.

At the beginning of this work in summer 2019, published research using the electron density reported by the Swarm Langmuir probes (LP) was limited and was focused on mid-latitude and equatorial regions (e.g., Buchert et al., 2015). However, three relevant papers of note were Chartier et al. (2018), which investigated polar cap patch occurrence using electron density data from Swarm, Goodwin et al. (2015) and Spicher et al. (2015), both of which considered polar cap patches using only a couple of passes of Swarm.

A barrier to the wider use of Swarm density measurements was the lack of validation studies for the Swarm LP probes. Lomidze et al. (2018) had recently published a paper showing electron density measurements provided by Swarm are reliable in the low and middle latitudes ionosphere, with underestimation of up to 20%. The authors did include some limited radio occultation measurements at high latitudes, with the admission that the measurement quality at high latitudes was of lower quality and that full validation work in the high latitudes would require a separate study.

E-CHAIM was developed specifically to improve the quantitative description of the ionosphere in the Canadian Arctic. It is based primarily on ionosonde data (Themens et al., 2017), which is relevant to the ionosphere at and below the F region peak. As well, recently

the model of the topside ionosphere had been improved (Themens et al., 2018). As an empirical model, E-CHAIM is ideal for studying large scale spatial variations and long term temporal trends.

The work presented in this chapter is divided into two largely independent comparative studies. The first study is the comparison of topside electron density as measured by Swarm A to that measured by Swarm C. This serves to give a perspective on the occurrence of polar cap patches on the dayside and nightside, while also assessing the consistency of electron density measurements between the two satellites. The second study is a comparison of the long term trends in the topside electron density observed by Swarm with the trends predicted by E-CHAIM .

Both studies are conducted in the Resolute Bay area, at extreme high latitudes. One of the advantages of the Resolute Bay location is that it is the site of the RISR-North and RISR-Canada incoherent scatter radars (e.g., Bahcivan et al., 2010; Gillies et al., 2016) as well as being covered by three SuperDARN radars located at Rankin Inlet, Inuvik and Clyde River. The RISR instruments are capable of providing information on the electron density profiles near Resolute Bay (e.g., Ullrich, 2021). The SuperDARN radars can provide estimates of the F region peak density (Ponomarenko et al., 2011; Ullrich, 2021) as well as detect polar cap patches (Spicher et al., 2015).

3.1 Geometry of Swarm satellite trajectories over the Resolute Bay area

In order to interpret the measurements made by the Swarm satellites it is important to understand the geometry of the constellation. The Swarm constellation originally consisted of three satellites Swarm A, B and C[1], which fly in circular, near-polar low Earth orbits with an orbital period of ~95 minutes (Friis-Christensen et al., 2008; Knudsen et al., 2017). The satellites transitioned from their launch orbits into their mission orbits in the first three months of 2014. Swarm A and C pass over Resolute Bay with an altitude of ~450 km, with Swarm C trailing Swarm A by 7-10 seconds and ~1.4° longitude separation (Knudsen et al., 2017). As a result, measurements made by Swarm A and C are close temporally and spatially, allowing reasonable comparison between them. In contrast, Swarm B operates independently at ~510 km in a separate orbital plane and with a different rate of precession.

Given that electron density is strongly dependent on altitude (Chapter 1), it is important

[1]The CASSIOPE/e-POP satellite which was added to the Swarm mission as Swarm E in 2018 (ESA, 2020), is not considered in this thesis. Unless expressly indicated otherwise, all references to Swarm and the Swarm satellites refer to the original triplet of Swarm A, B and C.

to determine the actual altitude of the satellites when passing near Resolute Bay. Figure 3.1 shows the average daily pass height above the surface of the Earth, calculated using the WG84 geodesic (Defense Mapping Agency, 1991), for all three satellites over the period 2014-2018. The modulation in average pass altitude observed is due to the fact that the orbits exhibit slight eccentricity and precess around the Earth, thus altering the location of the perigee.

Although Figure 3.1 shows that the orbit of Swarm A and C has decayed from 475 km (Knudsen et al., 2017) to ~445 km, Swarm A and C maintain nearly identical altitudes, with differences on the scale of centimetres (van den IJssel et al., 2015). The orbit of Swarm B has decayed from the intended altitude of 510 km (Knudsen et al., 2017) to ~500 km. When considering long term trends spanning multiple years, these changes in altitude need to be accounted for.

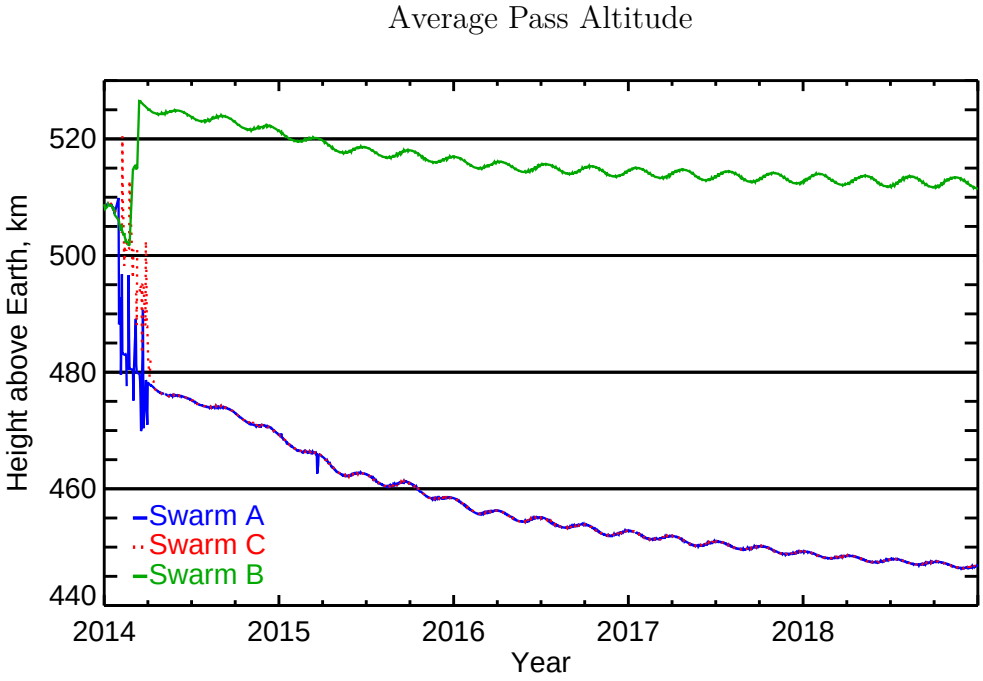

Figure 3.1: Daily mean pass altitude of the Swarm satellites for the period of 2014-2019. Note that during the first quarter of 2014, the satellites were still manoeuvring from launch orbits into mission orbits.

For the purposes of this chapter, the Resolute Bay region was defined as the area between 72.5° to 76.5° North and -85° to -105° East, with Resolute Bay in the approximate centre. On average the Swarm satellites complete 15 orbits per day, however only a few orbits pass through the region of interest on any given day. Typically two passes cross through the region

of interest, separated by a single orbital period of ~95 minutes. As the orbits of the satellites precess, the time of day when the passes occur gradually shifts. As a result multi-year, seasonal and diurnal effects must all be considered when comparing data.

3.2 Comparisons of Swarm A and Swarm C electron densities

Two example passes through the Resolute Bay area are given in Figure 3.2a,b. The satellite tracks are indicated as single North-South lines, with perpendicular lines, broadly East-West in orientation, indicating density. Each line represents the median density of a 0.2° geographic latitude bin of measurements. The satellite tracks and density lines are coloured according to satellite, with blue indicating the median measurements of Swarm A bins, and red indicating the median density of Swarm C bins. For reference, the location of Resolute Bay is indicated by the green point. Visually, it can be seen that both satellites measure comparable densities on the order of ~10×10^{10} m^{-3}.

For a more objective estimation of agreement, subplots c) and d) of Figure 3.2 compare the medians of the 0.2° bins of each satellite, with each point representing the median of Swarm A paired with the median of Swarm C for the same latitude bin. The standard deviation of data in each bin is shown by the horizontal and vertical lines plotted with each point. Vertical lines plot the standard deviation of Swarm A bins and horizontal lines of Swarm C bins. The line for perfect agreement is shown in red, bisecting each panel. Since both axes have an error estimate, a simple linear regression for the data of each satellite as a function of the other was calculated. The regression of Swarm A measurements assuming Swarm C measurements are ideal is provided in green, in the top left of each subplot. The regression assuming Swarm A measurements are ideal, is provided in the lower right in purple. R squared (R^2), that is, the square of the correlation coefficient, and the number of points for each regression are also provided. The linear regression line for each regression is plotted in the corresponding colour.

Daytime observations (~19:38 UT) are shown in Figure 3.2c. Clear clustering about the bisector of perfect agreement (red line) is shown. This is reflected in both the linear fit assuming Swarm C is ideal and the linear fit assuming Swarm A is ideal with fits of $N_e^{Swarm\ A} = 1.060 \times N_e^{Swarm\ C} - 2.98 \times 10^{10} m^{-3}$ and $N_e^{Swarm\ C} = 0.915 \times N_e^{Swarm\ A} + 0.706 \times 10^{10} m^{-3}$, respectively. Both regressions have a R^2 value of 0.97, indicating close to ideal fits. Computing Pearson's correlation coefficient (PCC) (not shown on the plot) as a second measure of agreement, gave a value of 0.985, confirming the results of the linear regression.

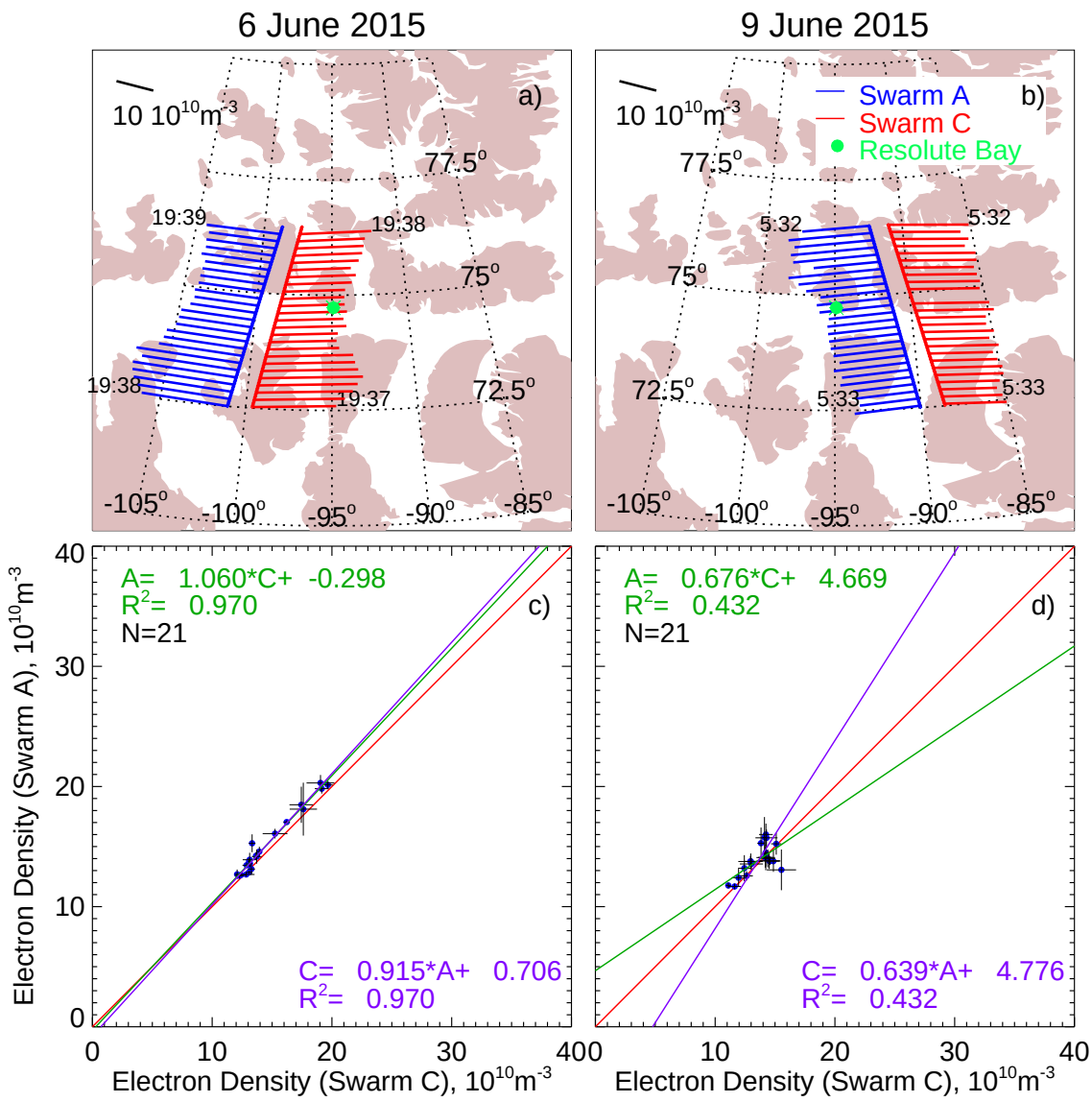

Figure 3.2: a) and b) Footprints of the Swarm A and C satellites at the height of 450 km as they travel over the Resolute Bay zenith (green circle) on 06 June 2015 (daytime) and 09 June 2015 (nighttime). The colored bars across the tracks reflect measured electron density. The electron density is given in units of 1×10^{10} m^{-3}. The scale is given by a vector in the top-left corner. c) and d) Comparison of the electron density medians computed in 0.2 ° bins of geographic latitude along the tracks, for the daytime and nighttime passes, respectively. Vertical and horizontal bars are standard deviations of data in each data bin. Presented also are the expressions for the linear fit lines assuming either Swarm C (green) or Swarm A (purple) values are known precisely.

Figure 3.2d shows a comparison similar to that in Figure 3.2c, however, nighttime observations made on 9 June 2015 (~5:32 UT) are shown. In this case, agreement is visually poorer. This is reflected in both the linear fit assuming Swarm C is ideal and the

linear fit assuming Swarm A is ideal, which have similar slopes, giving fits of $N_e^{Swarm\ A} = 0.676 \times N_e^{Swarm\ C} + 4.67 \times 10^{10} m^{-3}$ and $N_e^{Swarm\ C} = 0.639 \times N_e^{Swarm\ A} + 4.78 \times 10^{10} m^{-3}$ respectively. Both regressions have a R^2 value of 0.43, indicating a poor fit. Computing the PCC (not shown on the plot) as a second measure of agreement, gave a value of 0.657, confirming the results of the linear regression.

An explanation for the differences in agreement between the passes on 6 June 2015 and the passes on 9 June 2015 is needed. The passes are only three days apart, and subsequent days show passes with good agreement and poor agreement, which strongly implies the differences are due to variations in the electron density and not changes in the probes themselves. A very likely explanation for inconsistencies in the electron density is the occurrence of polar cap patches (Spicher et al., 2015). Top-side ionosphere plasma is known to drift in the $\vec{E} \times \vec{B}$ direction (Chapter 1.1.2). Due to this drift, Swarm A and Swarm C would cross a drifting patch at slightly different latitudes. Given a nominal time separation of ~10 s between the satellites and a drift speed of ~1.0 km/s, a reasonable expectation is that the plasma would drift 10 km between passes of the satellites. The density readings shown in Figure 3.2 are medians of 0.2° sections of latitude (~20 km), so drift alone does not explain the poor agreement. Two important geometric differences must be kept in mind. First, the Swarm A and Swarm C are separated by ~1.4° of longitude (~100 km) and the "edge" of the patch may not be straight. Second, the "edge" of the patch maybe at an angle to the track of the satellites.

Visual analysis of the plots shows the detection of sharp edges in the density by both satellites, often with separation of 0.5° (50 km) of latitude. With a longitudinal difference of ~1.4° , an angle of 30° is sufficient to produce the separation in latitude. In the presence of drifting polar cap patches with edges at an angle to the path of the satellites, agreement for the types of comparisons shown in Figure 3.2 are expected to be poor.

In order to qualitatively investigate the differences between the satellites, the analysis used to generate Figure 3.2 was extended to cover all passes over the region of interest during the period of April 2014 until the end of December 2018 resulting in 2585 passes to analyze. Passes were filtered to exclude instances where either satellite had less than 30 seconds of measurements in the region of interest.

If both satellites passed these minimum requirements and the satellites crossed through the region at an angle such that one satellite exited the region before the other, the longer range of latitude was used for both satellites.

In order to quantitatively assess the degree of disagreement between the two satellites, and by extension to quantify the occurrence of polar cap patches, the PCC was calculated for each pair of passes. The PCC was chosen because it characterizes linearity without assuming

either instrument is ideal.

Figure 3.3 shows the monthly PCC in black and a three point boxcar average in red. Note that the first three months of 2014 are excluded as Swarm A and Swarm C were still entering mission orbit and were operating at different altitudes, as shown in Figure 3.1. The monthly PCCs show good agreement between Swarm A and Swarm C, with only a single month showing agreement lower than 0.86, and agreement generally in the low nineties range. The PCC does not show a discernible solar cycle effect, as correlation does not meaningfully change between 2014 (solar cycle maximum) and 2018 (solar cycle minimum). The data are inconclusive regarding seasonal effects. Both 2014 and 2015 show better agreement, and fewer irregularities by implication, during the summer. This matches expectations that the long daylight hours in the High Arctic smooth out the upper ionosphere due to ionization from solar radiation. In contrast, 2015 and 2017 shows better correlation during the winter while 2018 shows better agreement during equinoxes.

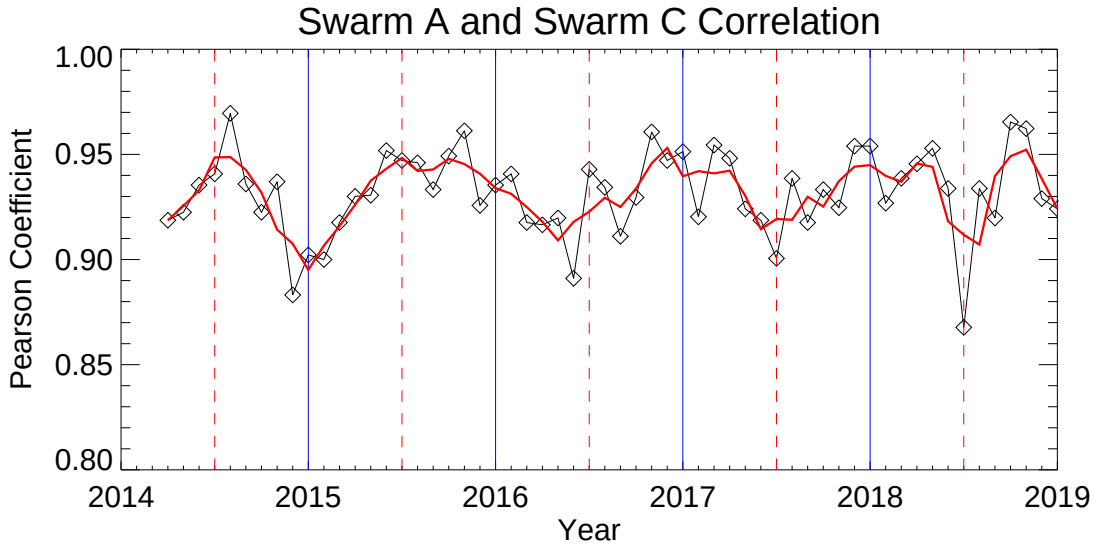

Figure 3.3: Pearson correlation coefficient for Swarm A - Swarm C electron density monthly datasets collected over the Resolute Bay area during 2014-2018. Data in all time sectors were considered. Red curve is a smoothed variation obtained by applying a car box filter with 3 consecutive values.

One of the stated goals of the thesis was to identify the time sector and season during which polar cap patches are most frequent. To this end, analysis of the PCC was extended by plotting histograms of the PCC separated along two dimensions, time sector and season. Similar analysis of other parameters, such as the slope of the linear fit, was not successful as the histogram distributions did not show any significant differences between time sectors or

seasons.

Figure 3.4 shows the histogram distributions resulting for the analysis. The top row of subplots are distributions from the day sector and the bottom row are distributions for the nighttime sector. The leftmost plots are the summer distributions, the middle for the equinoxes and the final two plots, on the right, are for the winter. The day sector was defined as 16-23 UT or 10-17 MLT, while the night sector was defined as 02-10 UT or 20-04 MLT. It should be noted that the definitions of day/night and day/night/dawn/dusk used here and elsewhere in this thesis are approximate and do not reflect precise sunlight conditions in the high latitudes. The summer season was defined as May until August, the winter season as November until February and the equinox "season" as the remaining months, March to April.

The summer season, Figure 3.4a and 3.4d, shows peaks in the distribution at r=0.8, where r is the PCC, in both the day sector and the night sector. However, the distribution in the day sector, Figure 3.4a, is narrower, with a more pronounced peak, than the distribution for the summer night sector, Figure 3.4d. This implies that polar cap patches are more frequent in the nighttime. This matches with the current understanding of the daytime topside ionosphere, which expects the ionizing effect of solar radiation to disintegrate and smooth out irregularities in the day sector.

The equinox season data, that is data for spring and fall, are shown in Figure 3.4b and Figure 3.4e. Both the nighttime and daytime distributions are similar. The peaks of the distributions are wider, r=0.6-0.9, than the summer distributions. There is a rather subtle increase in low correlation values in the nighttime.

Finally, Figure 3.4c and Figure 3.4f show the winter distributions. Both time sectors show a strong peak in the distribution, r=0.7-0.9, a small improvement in agreement compared to the equinox season. Both the winter and summer peaks are centered around the same value. Again, the nighttime distribution shows a greater prevalence of poor correlation, which is consistent with the summer distributions and with theory.

The general conclusion is that polar cap patches are more frequent on the nightside, regardless of the time of year, where polar cap patches are identified as a weakened correlation between the electron density measured by Swarm A and Swarm C at a given latitude. Unexpectedly, given the lower average electron density, the agreement between the satellites is the best in the winter.

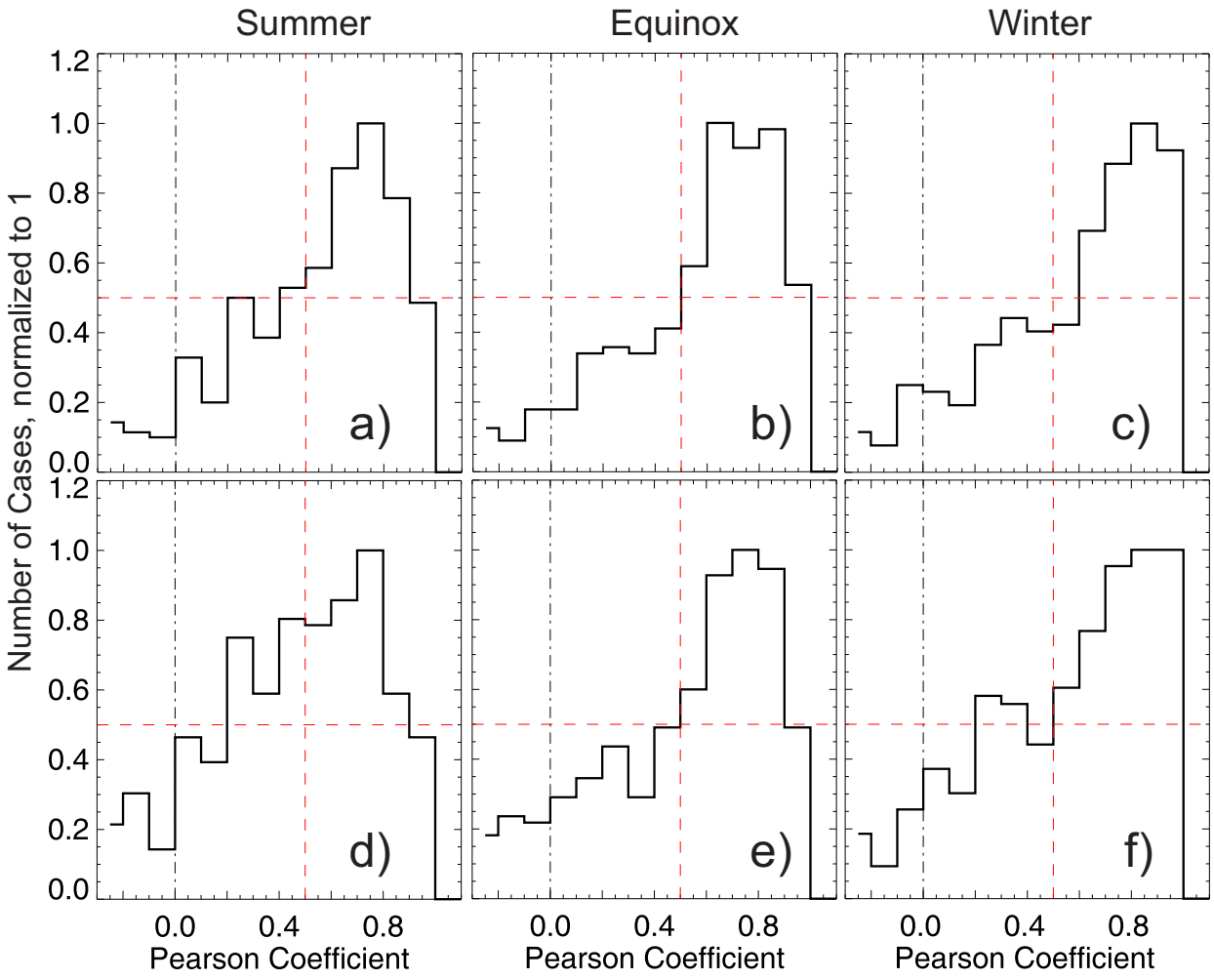

Figure 3.4: Pearson correlation coefficient distributions for joint Swarm A - Swarm C electron density data collected over the Resolute Bay area during 2014 (starting from April)-2018. Each distribution includes 350-400 points. Panels a)-c) are for daytime measurements (16-23 UT) while panels d) - f) are for nighttime measurements (02-10 UT).

3.3 Long term trends in the ionosphere above Resolute Bay: Swarm data and E-CHAIM predictions

The second focus of research undertaken in this chapter is the investigation of long term trends in the variation of the electron density in the Resolute Bay region, as measured by the Swarm satellites and as predicted by E-CHAIM (Themens et al., 2017). This research is prompted by the need to better quantify the topside ionosphere. The long term trends of the

electron density at the F region peak over Resolute Bay were recently discussed by Ullrich (2021). One issue of interest is whether the variations at different altitudes are the same. The physics governing the formation of the ionosphere is different at differing altitudes, so some differences in variations are expected. Another issue is the general lack of information regarding the long term behaviour of the top-side ionosphere (Kutiev et al., 2013), which is due, in part, to the lack of long term satellite missions capable of measuring the topside electron density. A final issue is the validation of the recently developed E-CHAIM model against measurements made by instruments not used in its development. This is vital for studies of the high latitude ionosphere where satellite coverage is limited. In particular, Swarm data are limited to certain times of the day, which change over the years. In some years the satellites only pass through the Resolute Bay area during the nighttime while in other years all passes occur in the daytime hours. Validation of E-CHAIM would expand the range of topics that can be considered for investigation.

Although not the focus of Figure 3.5, the limited pattern of satellite coverage is clearly evident in Figure 3.5b, which shows an overview of average electron density measured by Swarm A and C (Figure 3.5b) and predicted by E-CHAIM (Figure 3.5a). The plot covers measurements from January 2014 through December 2018, as indicated on the common y-axis. The local time at Resolute Bay is indicated on the x-axis of each subplot. The electron density on both subplots is indicated by colour, with grey indicating no data.

For Figure 3.5 and subsequent plots in this section, E-CHAIM was used to generate predictions of electron density at the location of Resolute Bay (74.68°N, -94.87°E). An electron density value was calculated for each hour of each day, on the hour, at the average altitude of all Swarm A and Swarm C passes in that day. The same passes that were used in Section 3.2 were used in this section. In Figure 3.5a the E-CHAIM prediction for each day and hour is depicted. It should be recalled that the altitude of the satellites was highly variable in the first quarter of 2014 (Figure 3.1) and the black bands of low density seen are the result of a much higher average altitude of Swarm A and C.

Overall, Figure 3.5a shows a decrease in electron density from 2014 (high solar activity) to the end of 2018 (low solar activity). Seasonal variations are also evident, with enhancement of density predicted in the spring (March-April) and a decrease in density in the winter (December-January). The diurnal cycle is also evident in the predictions, with modelled density increasing at noon and persisting until 22-23 local time. These features are consistent with trends identified in the electron density of the F region peak (Koustov et al., 2019). The decrease in density at noon from 2014 to 2018, by about a factor of 2, agrees with that of Koustov et al. (2019). However, the decrease in electron density for the dusk and dawn sectors is predicted to be larger, 3 or 4 times.

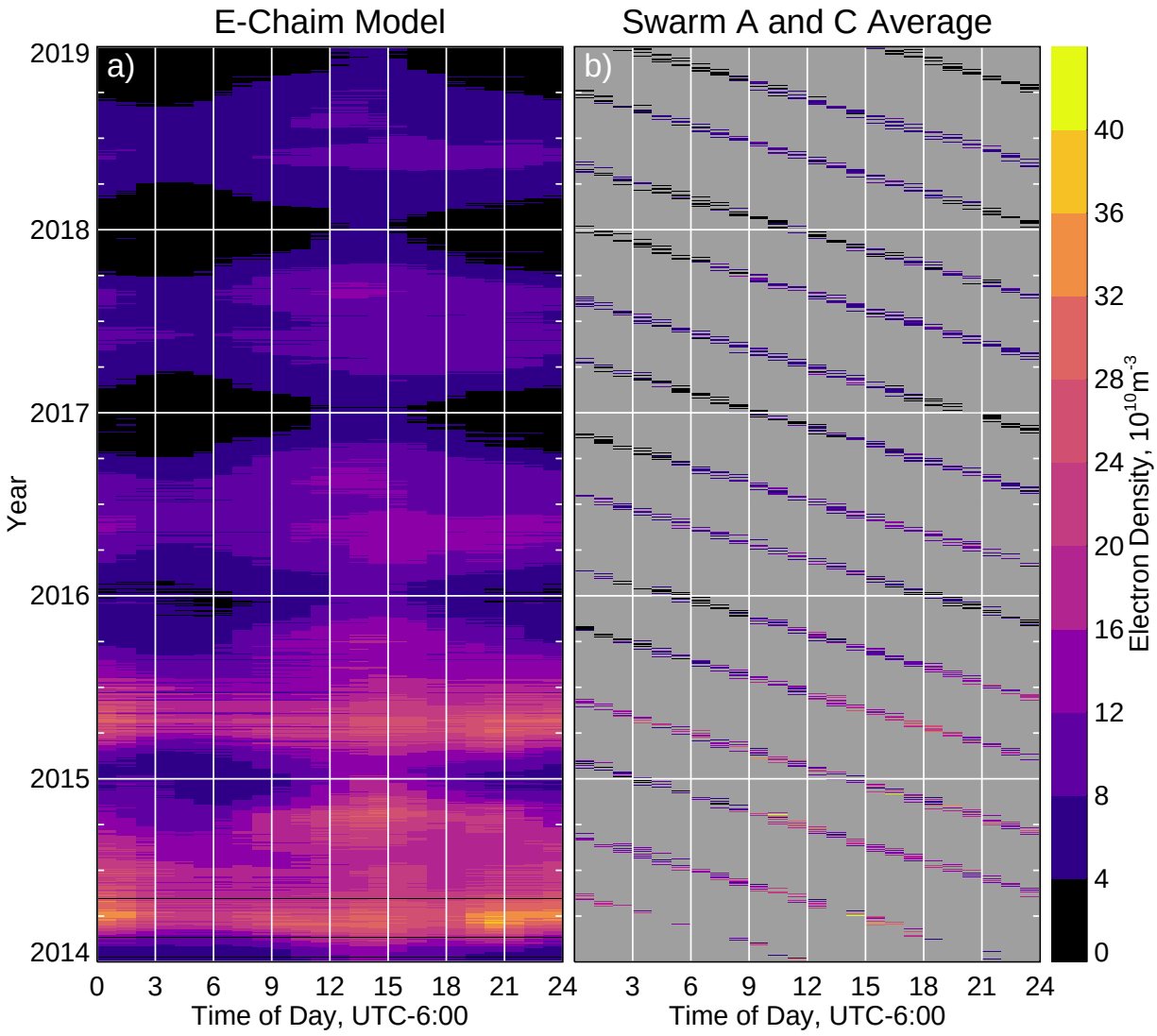

Figure 3.5: Electron density over Resolute Bay (RB, Nunavut, Canada)) in coordinates "local time-year" a) according to the E-CHAIM model (Themens et al., 2017) and b) Swarm A and C measurements. The E-CHAIM data are for the height, location and time of Swarm measurements (see the text).

As mentioned, the Swarm data are clearly limited, as seen in the diagonal stripped pattern in Figure 3.5b. However, a general decrease in electron density from 2014 to 2018 is still evident. The magnitude of the decrease in density is less than that predicted by E-CHAIM . Unfortunately, the satellites' orbits were such that there was limited Swarm data for the dawn or dusk time sectors in 2014.

Comparison of E-CHAIM and Swarm was further advanced by comparing each time sector independently. The day was broken into four time sectors of six hours each, dawn (3:00 to 9:00 LT), day (9:00 to 15:00), dusk (15:00 to 21:00 LT) and night (21:00 to 3:00 LT). Resolute

Bay is located at UTC -6 and daylight saving was not applied.

Figure 3.6 shows the time sector comparison of Swarm A (blue) and C (red) with E-CHAIM (black). The median electron density of all passes in each day are plotted as points.

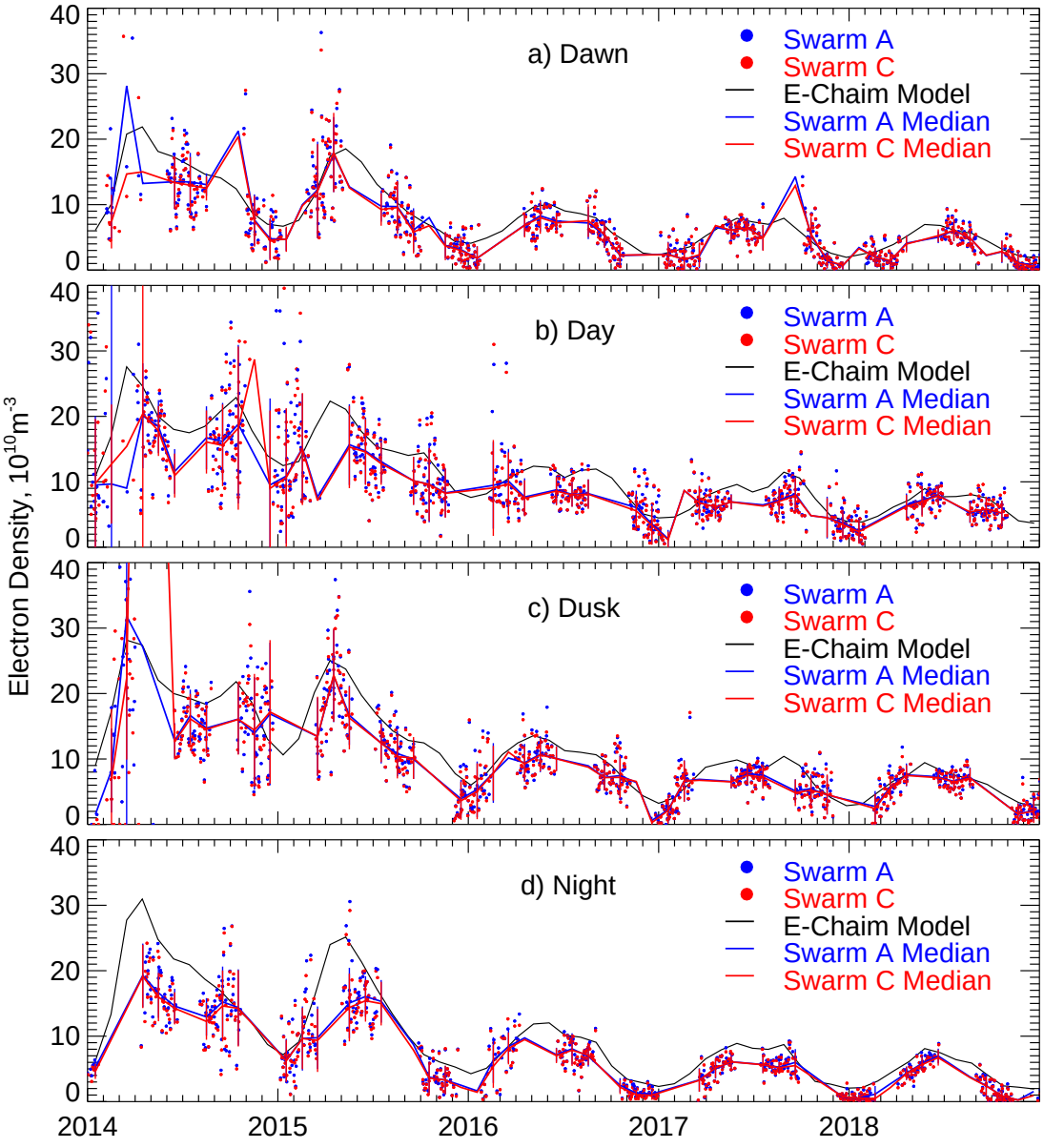

Figure 3.6: Electron density near the Resolute Bay zenith as predicted by the E-CHAIM model (Themens et al., 2017) and measured on Swarm A and C satellites for 2014-2018. Time sectors were introduced as follows: dawn (3:00 to 9:00 LT), day (9:00 to 15:00 LT), dusk (15:00 to 21:00 LT), and night (21:00 to 3:00 LT). The model values (lines) are medians of all values available for a specific time sector.

To identify trends, the median of all densities measured in each month were calculated and plotted as lines. The vertical bars indicate the standard deviation of each monthly bin. Due to the high degree of correlation between Swarm A and Swarm C, the points and lines often overlap. For E-CHAIM only the monthly median is shown. Unsurprisingly, the Swarm coverage is patchy and daily medians are quite variable.

Each of the four time sectors exhibits an overall trend of decreasing electron density from 2014 to the end of 2018. This is consistent with the results shown in Figure 3.5, but is shown more explicitly. The change in density is stronger in the dusk sector and less prominent in the day sector.

Seasonal changes are exhibited in some years. For example, in 2016-2017 the density is larger around the equinoxes than in the winter months. The result is similar to changes in the F region peak density identified by Koustov et al. (2019) in their Figure 3.4.

The trends seen in the E-CHAIM predictions are consistent with the solar cycle progression. The model shows electron densities systematically higher than those measured by Swarm during 2014-2015, when solar activity was highest. The model predicts as much as twice the measured electron density and the difference is largest in the night sector. The disagreement between the model and the measured data decreases with solar activity decay, and by 2018 the disagreement is minor. The seasonal variations predicted by the model are matched by synchronous variations in the measured density, for example, a relatively smooth variation occurring in dawn 2016 and the strong enhancement in dusk during the 2015 spring equinox. The qualitative agreement in variations between the model and the satellites is the least similar in the day sector. This is unexpected, as solar radiation is expected to be a major factor in the formation of the topside ionosphere. However, as indicated in Section 1.2.5, the formation of the topside ionosphere is complex and it is difficult to identify a main mechanism of formation.

Figure 3.7 presents the results of the same analysis as Figure 3.6 but for Swarm B (green). The E-CHAIM predictions were generated in the same manner, but using the daily average altitude of Swarm B. It can be seen that the Swarm B and E-CHAIM exhibit the same trends at the higher altitude of ~510 km, but with smaller differences between the two.

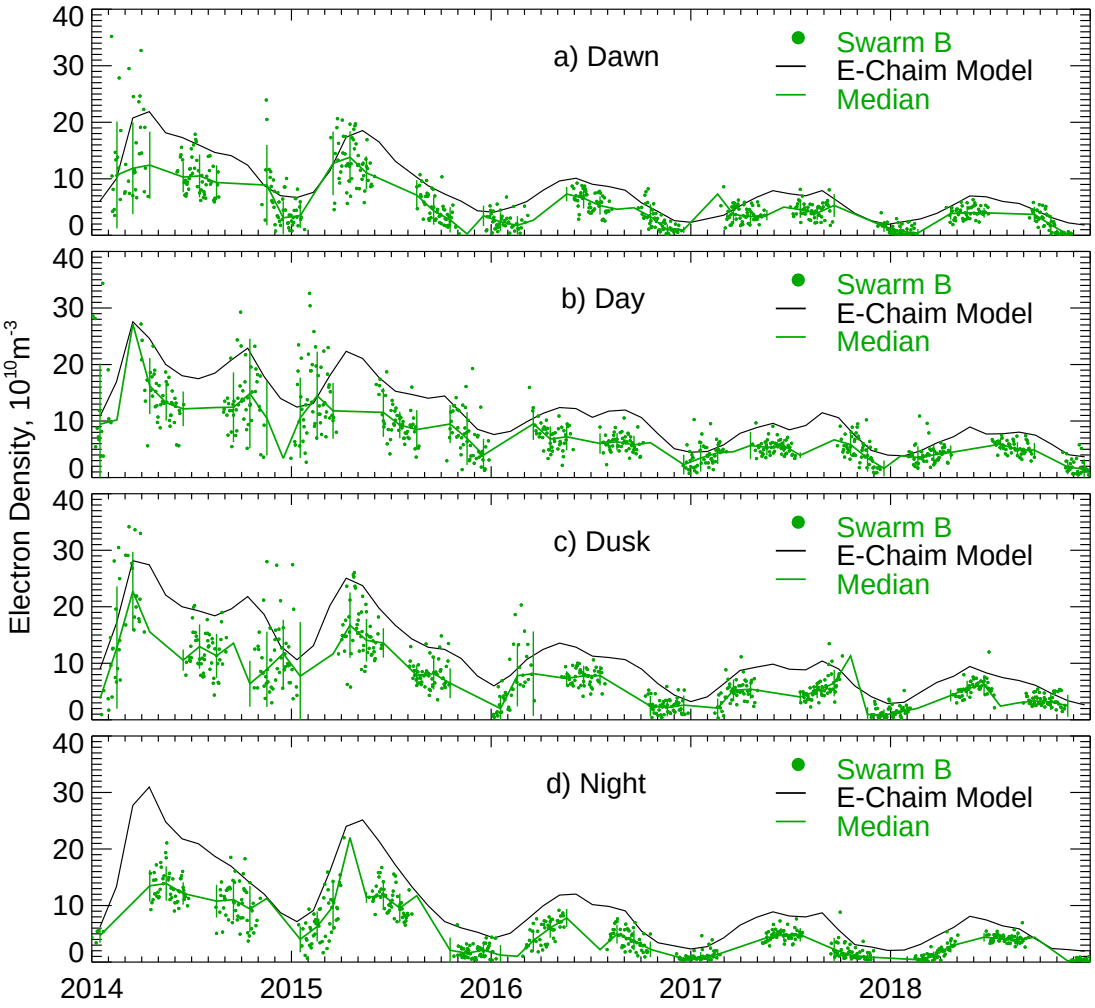

Figure 3.7: The same as in Figure 3.5 but for Swarm B measurements and corresponding E-CHAIM predictions.

The differences observed between Swarm measurements and the electron density predicted by E-CHAIM are not unexpected. E-CHAIM is primarily a climatological model and, as a result, should not be expected to accurately predict minor or transient details in the ionosphere. Additionally, the Swarm LPs are not yet calibrated for the high latitude ionosphere. In the middle latitudes they are known to underestimate electron density by ~20% (Lomidze et al., 2018). If a similar underestimation applies to the high latitudes, then the differences between E-CHAIM and the Swarm measurements are smaller and agreement between the two is reasonable.

A final analysis of the agreement of Swarm and E-CHAIM undertaken is shown in Figure 3.8. A 2-D histogram was generated by binning the median density measured by Swarm for

each hour with the density predicted by E-CHAIM for that hour. The resultant histograms for Swarm A, Figure 3.8a, and Swarm B, Figure 3.8b, are shown. Bins of 1×10^{10} m^{-3} were used along both axes. Because the Swarm measurements were sorted by hour, and not by pass, the number of points exceeds the number of passes. The colour of each bin indicates the number of measurements in that bin.

From Figure 3.8 it can be seen that E-CHAIM predicts electron densities larger than those measured by Swarm by 20-30%, or conversely, Swarm underestimates the electron density by 20-30%, a result in line with that found by Lomidze et al. (2018) for the middle latitudes. In general, there is a trend towards greater underestimation at higher densities.

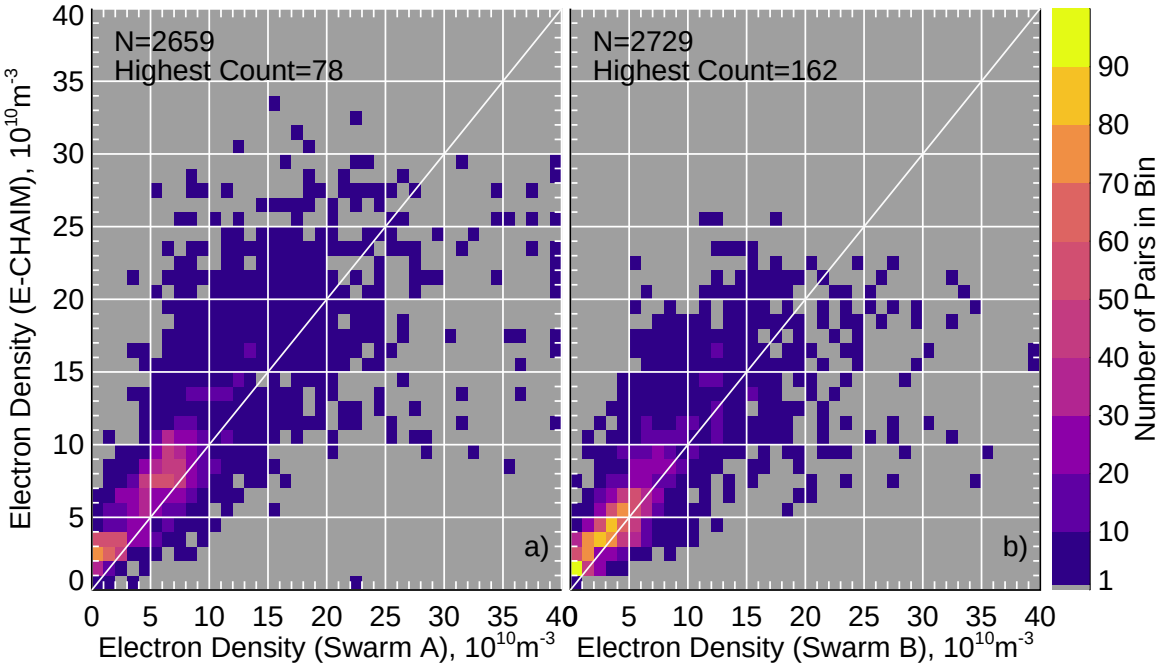

Figure 3.8: Scatter plots of the electron density predicted by the E-CHAIM model for the height and time of a) Swarm A and b) Swarm B measurements near Resolute Bay (for criteria of co-location see the text). The data are binned in steps of 1×10^{10} m^{-3}.

In summary, the long term trend of electron densities in the Resolute Bay region is a decrease in density toward the solar minimum, by a factor of two.

The decrease in electron density is more pronounced in the dusk time sector. Seasonal patterns can be seen, with some years showing larger densities around the equinoxes than in the winter. Electron density medians during the summer were comparable to densities around the equinoxes. Thus, for the Resolute Bay region, no winter anomaly effect (Kutiev et al., 2013) was found in the topside ionosphere. This is expected, as the winter anomaly effect is documented only for the middle latitudes.

E-CHAIM predictions show the same trends as those observed in Swarm measurements, but with larger densities. The predicted values are 10-30% larger, depending on time sector. The largest differences between predicted and observed values were seen in the night sector during high solar activity (2014).

3.4 Summary

This chapter presented the investigation of two aspects of the topside electron density in the polar cap, specifically the Resolute Bay region, defined as 72.5° to 76.5° North and -85° to -105° East. Long term trends in the electron density were investigated and E-CHAIM predictions of electron density for the Resolute Bay area were compared to the density as measured by the Swarm satellites.

In investigating long term trends, passes through the region were identified and the median densities of 0.2° latitude bins were calculated for Swarm A and C. Scatter plots comparing the electron density measured by each satellite were plotted. In order to asses trends, the Pearson correlation coefficient was calculated for each plot. Instances where the PCC was small were associated with polar cap patches. A more detailed analysis was conducted by sorting the data by time of day, day or night, and by season, summer, winter and equinox. Histograms of these subsets of the data showed polar cap patches were more frequent in the night sector, especially in the summer and winter seasons. The equinoctial season showed fewer polar cap patches.

Plotting the Swarm measurements versus time highlighted the solar cycle and long term trends. A decrease in electron density for the region from high solar activity (2104) to low solar activity (2018) by a factor of approximately 2 was observed. Due to orbital precession, the data coverage of Swarm varied by time of day from year to year too significantly to allow for a well grounded conclusion with respect to seasonal change. However, no evidence for a winter anomaly effect in the polar cap region was found.

Finally, comparisons between the electron density measured by the Swarm satellites and the density predicted by E-CHAIM showed reasonable qualitative agreement between the model and the measured data at the altitudes of ~450 km (Swarm A and C) and ~510 km (Swarm B). E-CHAIM was found to predict densities 20-30% higher than observed by Swarm. This is comparable to the magnitude of the electron density underestimation by Swarm LPs in the middle latitudes found by Lomidze et al. (2018). The difference between the model and the measurements was found to increase at higher densities, such as during periods of high solar activity.

Chapter 4

Topside electron density over Resolute Bay as measured by Swarm satellites and incoherent scatter radars

In this Chapter the comparison of the electron density measured onboard Swarm satellites in situ and the electron density measured by incoherent scatter radars at nearly coinciding points in space and time is presented. The objective of this Chapter is to assess the differences between the two classical instruments for electron density measurements in the Earth's ionosphere. Despite of expected high consistency between the instruments, inter-calibration of the instruments is important for users of the data, and the work in this chapter fills in the void in this knowledge.

Results presented in this chapter have been submitted for publication as a paper:

Larson, B., Koustov, A. V., Kouznetsov, A. F., Lomidze, L., Gillies, R. G., & Reimer, A. S. (2021). A comparison of the topside electron density measured by the Swarm satellites and incoherent scatter radars over Resolute Bay, Canada. *Radio Science*, *56*. https://doi.org/https://doi.org/10.1029/2021RS007326

My contributions to this study are as follows:

- Development of the software for identification of joint incoherent scatter radar-Swarm conjunction points and selection of criteria for proximity of the satellite measurements points and radar range gate of measurements. Reaching a compromise between the proximity criteria and data availability.
- Development of the software for the analysis of the electron density measured by the incoherent scatter radars RISR-C and RISR-N.

- Development of the software for the analysis of the electron density measured by Langmuir Probes on Swarm satellites.
- Analysis of joint data for various conditions.
- Production of all Figures for the paper.
- Participation in writing of the manuscript.
- Contributions to the work on reviewers' comments and production of additional diagrams that are not part of the paper.

4.1 Introduction

Knowledge of the electron density distribution in the Earth's ionosphere is fundamentally important for a general understanding of the electrodynamical interaction between the Sun and Earth as it has been recognized that the ionosphere is not a passive element in the system (e.g., Wiltberger et al., 2017). On the other hand, practical needs such as establishing reliable communication using high frequency (HF) radio waves dictate the need for refining the details of the electron density distribution as a function of conditions in space (Belehaki et al., 2015; Rawer, 2013). Of special interest is the high latitude ionosphere where it is very dynamic because of energetic particle precipitation ionizing neutral atoms and molecules and because of plasma redistribution under an applied electric field of magnetospheric origin.

Over the decades, significant information has been accumulated with respect to the maximum electron density in the ionosphere, at the height of the F layer peak (e.g., Danilov, 2021; Kutiev et al., 2013; Laštovička, 2017). This information has led to the development of global scale, comprehensive models of the electron density distribution in the ionosphere at all heights. For example, the International Reference Ionosphere model (IRI, Bilitza, 2018; Bilitza et al., 2017) and NeQuick model (Nava et al., 2008). These models seem to perform reasonably well with respect to the peak electron density at middle latitudes, but they still require improvements at high latitudes (Bjoland et al., 2016; Themens et al., 2017). One example of an improved ionospheric model for high latitudes is the recently developed Empirical Canadian High Arctic Ionospheric Model (E-CHAIM, Themens et al., 2017; Themens, Jayachandran, McCaffrey, et al., 2019).

Efforts in assessing and predicting the ionospheric electron density away from the electron density peak are less extensive (e.g., Coïsson et al., 2006; Pignalberi et al., 2018; Rawer, 2013). One interesting question is about the electron density height profile above the F region peak, known as the topside ionosphere. At these heights, traditional ground-based ionosondes

cannot provide information, while ionosonde observations on satellites are very limited (Davis, 1990; Hunsucker, 1991; Pignalberi et al., 2018; Rawer, 2013). Ground-based incoherent scatter radars (ISR) are capable of measuring electron density up to the heights of ~700 kilometers (Beynon & Williams, 1978; Hunsucker, 1991; Rawer, 2013). Modern phased-array ISRs sound the ionosphere along several directions nearly simultaneously, allowing them to build a 3-D volumetric image of the electron density with temporal resolutions often as good as 1 min (e.g., Gillies et al., 2016; Semeter et al., 2009). However, there are few such systems, and their operation time is limited.

Over the last decades, several satellite missions were successful in providing electron density measurements above the F region peak (e.g., Hocke & Igarashi, 2002; Huang et al., 2015). Besides traditional Langmuir Probes (LP) measurements, e.g., Lebreton et al. (2006), radio occultation (RO) techniques became popular (e.g., Hocke & Igarashi, 2002). One obvious advantage of satellite in situ measurements is their global coverage so that a single pass provides electron density (at a certain height) along a trajectory from the Southern to Northern hemispheres. Outcomes of these experiments have been discussed in a number of papers (e.g., Huang et al., 2015; Kakinami et al., 2008; Kutiev et al., 2006).

One important aspect of the electron density measurements with various instruments is consistency between the instruments. With respect to LP measurements, interesting work was done by McNamara et al. (2007) who considered Challenging Minisatellite Payload (CHAMP) satellite electron densities and concurrent ionosonde measurements in the equatorial ionosphere where the electron densities were very high, mostly with critical frequencies of the F2 layer between 10 and 14 MHz. They reported that the average discrepancy for CHAMP passing above the peak of the F2 layer was 0.22 MHz (or only about 2.6%), while for the measurements below the peak the average discrepancy of 0.25 MHz (or 4.2%) was found, with the ionosonde values systematically higher than the CHAMP measurements in both cases.

Important contributions to studying the electron density distribution in the topside ionosphere have started being published with the data from three relatively new satellites, Swarm A, B and C, launched by the European Space Agency in November 2013 (Buchert et al., 2015; Chartier et al., 2018; Jin et al., 2019; Spicher et al., 2015). These satellites employ LP instruments (Buchert et al., 2015; Friis-Christensen et al., 2008; Knudsen et al., 2017). LP instruments have flown on numerous spacecraft (Kakinami et al., 2008; Lebreton et al., 2006; Lee et al., 2013) and showed robust performance. However, despite the fact that these are well-established devices for measurements of the plasma electron density, the validation work for the Swarm instruments is limited. A recent publication by Lomidze et al. (2018) has addressed this shortcoming of Swarm experimentation and found that Swarm LPs systematically underestimate electron density by about 20% (or the plasma frequency by

~10%). They used, however only about 2.5 years of Swarm data available at that time and did not focus specifically on high latitudes. Furthermore, for Swarm data calibration, they used only low and middle latitude ISRs. Their comparison of Swarm data with Constellation Observing System for Meteorology, Ionosphere, and Climate (COSMIC) RO measurements for low electron densities included the high latitude data, and no significant differences between the two were reported. However, an assumption of spherical symmetry in the RO method can cause substantial errors in the presence of horizontal electron density gradients, which is a possibility in the polar cap ionosphere (Shaikh et al., 2018).

It is critical to continue work related to validation of the Swarm measurements as more data is becoming available. The goal of this study is to extend the previous work by Lomidze et al. (2018) at high latitudes with more recent data and compare electron density measurements onboard Swarm satellites with concurrent measurements by the Resolute Bay ISRs, which are located at the extreme high latitude of ~74.5° N (~83° of MLAT).

4.2 Instruments

Information on the Swarm satellites and the LP instruments providing electron density data (Buchert et al., 2015; Knudsen et al., 2017) has been given in previous Chapters 2 and 3. Here is provided more details important for understandings of the issues addressed in this chapter.

The Swarm LP sensors are traditional spheres, ~4-mm of radius sticking out of the satellite main body on 8-cm long posts. Physically, two sets of probes are available, one for measuring high densities ($> 10 \times 10^{10}$ m^{-3}, $f_p > 3$ MHz plasma frequency) and one for measuring low densities ($< 10 \times 10^{10}$ m^{-3}, $f_p < 3$ MHz plasma frequency) by collecting the strong or weak current, respectively, under various applied bias voltages (Knudsen et al., 2017). Swarm LP sensors were chosen to operate in the so-called harmonic mode, similar to the design by Siefring et al. (1998). Instead of the traditional approach of building the volt-ampere (V-I) curve, Swarm LP measurements are done at only three bias voltages: (a) at small voltage so that the probe current is driven solely by collected ions, (b) at a relatively large voltage so that the electron current saturation is reached (linear part of V-I curve), and (c) at intermediate voltages in the middle of the V-I curve "knee" where the transition from the ion-driven current to the electron saturation curve occurs (retarded electron region). At these points, the voltage is amplitude-modulated sinusoidally at a frequency of ~125 Hz for up to 10 periods of ~100 ms duration. Data for two periods of 79-ms duration within each one-second interval are used to compute the average ion current for point (a), during negative biasing voltages. In this way, electron density data at a rate of 2 Hz are produced. Alternatively, the electron

density can be evaluated at the biasing voltage point (b) by computing derivative dI/dV proportional to the admittance of the plasma and thus the electron density. The assumption is made that the plasma consists of only O^+ ions and the effect of plasma $\vec{E} \times \vec{B}$ motion is neglected (Buchert et al., 2015). More details on the principle and modes of LP operation are given by Buchert et al. (2015) and Knudsen et al. (2017).

Initial information on the ISR radars providing electron density data has been given in previous Chapter 2. Here more details important for understanding the issues addressed in this chapter are given.

The Resolute Bay (RB) incoherent scatter radars, RISR-North (RISR-N) and RISR-Canada (RISR-C), are modern modular-type systems capable of pulse-to-pulse beam repositioning which enables 3-D volumetric imaging with time resolutions of up to 1 minute which can be increased or decreased depending on the number of beams used and the magnitude of the plasma density (e.g., Bahcivan et al., 2010; Gillies et al., 2016). Historically, the radars operate mostly in two modes. One type of mode is the so-called "Imaging" modes that use up to 51 beams. The second type of mode is the so-called "world-day (WD) mode" which uses 11 beam positions and provides both E and F region measurements. For the WD modes, the density of beams is lower compared to Imaging modes, but provides a wide spatial coverage critical for the derivation of the plasma $\vec{E} \times \vec{B}$ flow. The present study considers RISR data collected in the WD mode of operation. This is of particular importance for nighttime operations when the ionosphere becomes significantly depleted and the electron density height profiles are often spiky and irregular. To alleviate difficulties in dealing with irregular electron density height profiles, only data with 5-min integration time were considered in this study.

The electron density data used in this study were produced by the standard data processing procedure used for the RISRs. For the topside measurements, an assumption of purely O^+ ion plasma is adopted. A non-linear least-squares best fit of a theoretical ion-line power spectrum is fitted to the radar measurements. This fitting procedure solves for four parameters, producing a best-fit electron density, electron temperature, ion temperature, and line-of-sight bulk plasma drift velocity assuming the ionospheric plasma is in thermal equilibrium. For this study, it is important to note that the electron density derived from ISR measurements depends on the ratio of the electron and ion temperatures, however, if the errors in the best-fit parameters are small, the uncertainty in ratio of the electron and ion temperatures brings little uncertainty in the electron density measurement. If the errors are large the ratio can cause the electron density value can vary by a factor of up to 2 (Ding et al., 2018). The single-ion composition assumption does not affect significantly inferred electron densities (e.g., Wissing et al., 2011). Depending on the radar, integration time, echo power and the

method of analysis, the differences in the inferred electron densities can be large (e.g., Wissing et al., 2011). For this reason, in the case of the RISR radars, special attention is paid to the calibration of the instruments.

Calibration of the electron density produced by the RISRs is routinely performed in one of two different ways: comparison with simultaneously received enhanced plasma line data or comparison with the co-located Resolute Bay Canadian Advanced Digital Ionosonde (CADI) data. Comparisons with the CADI are performed by comparing the RISR-derived critical frequencies of the F2 layer f_0F2 and the height of the maximum h_mF2 with those measured by the CADI. Values of f_0F2 and h_mF2 are obtained for the RISRs by fitting a 2-nd order polynomial to the electron density profile near the peak. To remove potentially possible differences between the radar and CADI due to differences in sensing modality (e.g., CADI has a much larger FoV with much poorer spatial resolution), the comparison of f_0F2 and h_mF2 between the instruments is performed statistically, usually with several days of data. The median ratio of the f_0F2 between the radar and CADI is used to derive a calibration constant for each radar beam. Finally, the fits of the ion-line data are reprocessed using the new calibration constants. The calibration procedure is repeated until the median ratio is ~1.0.

4.3 Example of Swarm-RISR comparison, the event of 12 October 2016

Figure 4.1 shows the geometry of joint Swarm-RISR radar observations when satellites A and C were flying near the RB zenith on 12 October 2016. For this day, the RISR radars were both operational and provided data. We note that the time of the event, ~23:00 UT, corresponds to the dusk sector (local midnight for RB is at 6 UT).

The one-minute time stamps for Swarm A measurements are indicated along its track. Swarm C is ahead of Swarm A by ~7 s. Measured electron density (at the heights of ~450 km) is shown by segments of the tracks that are color-coded according to the color bar on the right. The shown electron density for each segment is a median value of multiple successive Swarm measurements in bins covering 0.2° geographic latitude along the satellite track. One can see that the densities were on the order of ~10×10^{10} m^{-3}.

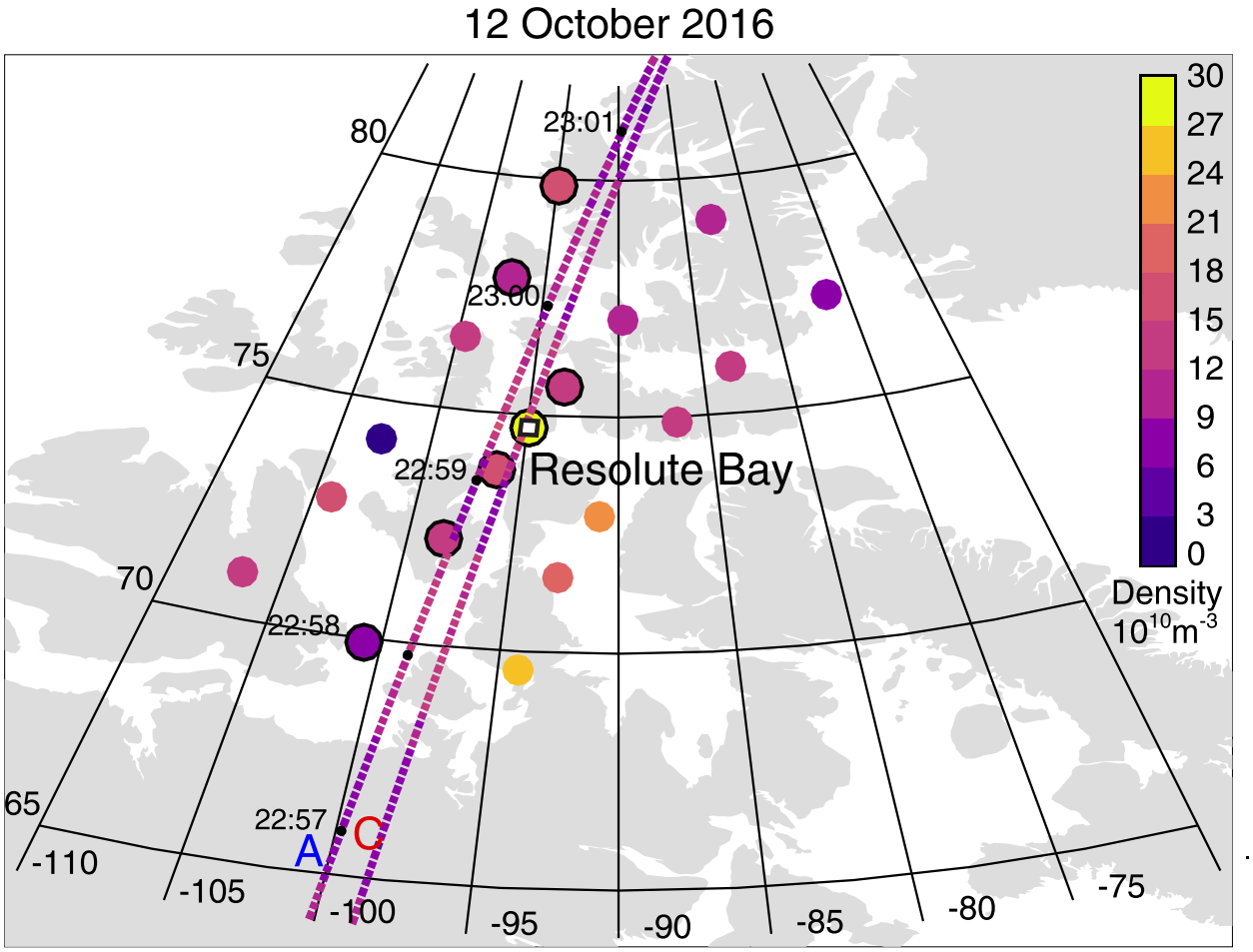

Figure 4.1: Swarm A and Swarm C satellite tracks (two lines across the diagram) and the ionospheric locations at the altitude of ~450 km (colored circles) where the electron density was measured by the Resolute Bay (black square) incoherent scatter radars. The event of 12 October 2016 is considered. Circles to the North-East of the square are locations for the RISR-North radar measurements while circles to the South-West of the square are locations for the RISR-Canada radar measurements. The electron density is given in units of 10^{10} m^{-3} according to the color bar shown on the right. Individual points of radar measurements "collocated" with Swarm A tracks (with separation of <200 km) are emphasized by black circles.

Solid colored circles in Figure 4.1 are ionospheric locations where the electron density was monitored by the RISR-C (south-west of RB) and RISR-N (north-east of RB) at a height of ~450 km. On this day, the RISR radars were operating in the WD mode, and 5 min data for RISR-C and 1-min data for RISR-N are available. In Figure 4.1, the locations where ISR measurements are matched with the measurements from Swarm A, both in time and space, are emphasized by black solid lines. The radar-satellite "conjunction" was selected to occur when the separation between the center of the radar gate and the satellite was less than 200 km and the difference in altitude was less than 20 km. In terms of time, differences up to 2.5

min were allowed.

In Figure 4.1, the electron density measured by the radars ranged from ~10×10^{10} m^{-3} to ~20×10^{10} m^{-3}, showing more variability than the Swarm data. For the "conjunction" points the agreement between the radar and satellite measurements is visually reasonable for most of the points except for one, for the near-vertical RISR-N beam, so that the yellow-colored circle stands out from otherwise beige/violet-colored circles. This point is accompanied by three other circles to the South-East with similarly large electron density as measured by the RISR-C radar. These observations indicate the occurrence of a strong polar cap patch extended toward the East.

Figure 4.2 provides a more detailed comparison of the data from the instruments. Panel (a) shows the electron density measurements by Swarm A and C with a time resolution of 0.5 s versus geographic latitude, along the respective tracks. One can see consistent spatial variations of the electron density and strong peak-to-peak variations, by a factor of 2. Two strong enhancements of the electron density are seen at geographic latitudes ~70° and ~75°, consistent with the radar data enhancements seen in Figure 4.1. This is an indication that the satellites were crossing the ionosphere with polar cap patches, likely at the western edge of the large-scale structure seen in the ISR data, Figure 4.1. The Pearson correlation coefficient between the curves in Figure 4.2a is 0.88 which is remarkably good for such an irregular ionosphere. One can also notice some "delays" in the curves' variations, the red curve sharp changes occur at slightly lower latitudes than those for the blue curve. These differences can be explained by the fact that the satellites are spatially separated by ~100 km, see Figure 4.1, so that they detect patches of somewhat different shapes and at somewhat different locations.

Figure 4.2b compares Swarm A and Swarm C data median-filtered over 0.2° geographic latitude along their paths. Despite some spread in the data of Figure 4.2b, many points concentrate around the bisector of perfect agreement (red line). We remind the reader that the measurements are shifted in time by ~7 s and the satellite's paths are separated by ~100 km (Figure 4.1) and therefore perfect agreement is not expected.

Overall, the two satellites report very comparable electron densities. This was not always the case. For some other passes, the differences were more significant. However, statistically, for example on a monthly basis, the overall point clustering around the bisector of perfect agreement holds reasonably well. This is an indicator that the LP instruments on the satellites are working consistently with each other.

Figures 2c and 2d compare coincident Swarm and ISR measurements. In this case, to identify a "conjunction" in radar and satellite measurements the same criteria were selected as for the data in Figure 4.1. Note that the allowed up to 2.5-min difference between Swarm and ISR measurements originated from the choice to consider ISR data obtained with the

5-min integration time. For Swarm data, all points satisfying the proximity criteria were selected and their median value was selected as the one characterizing the electron density in the ionosphere. The standard deviation within every Swarm conjunction data set was adopted as a measure of the error in measurements.

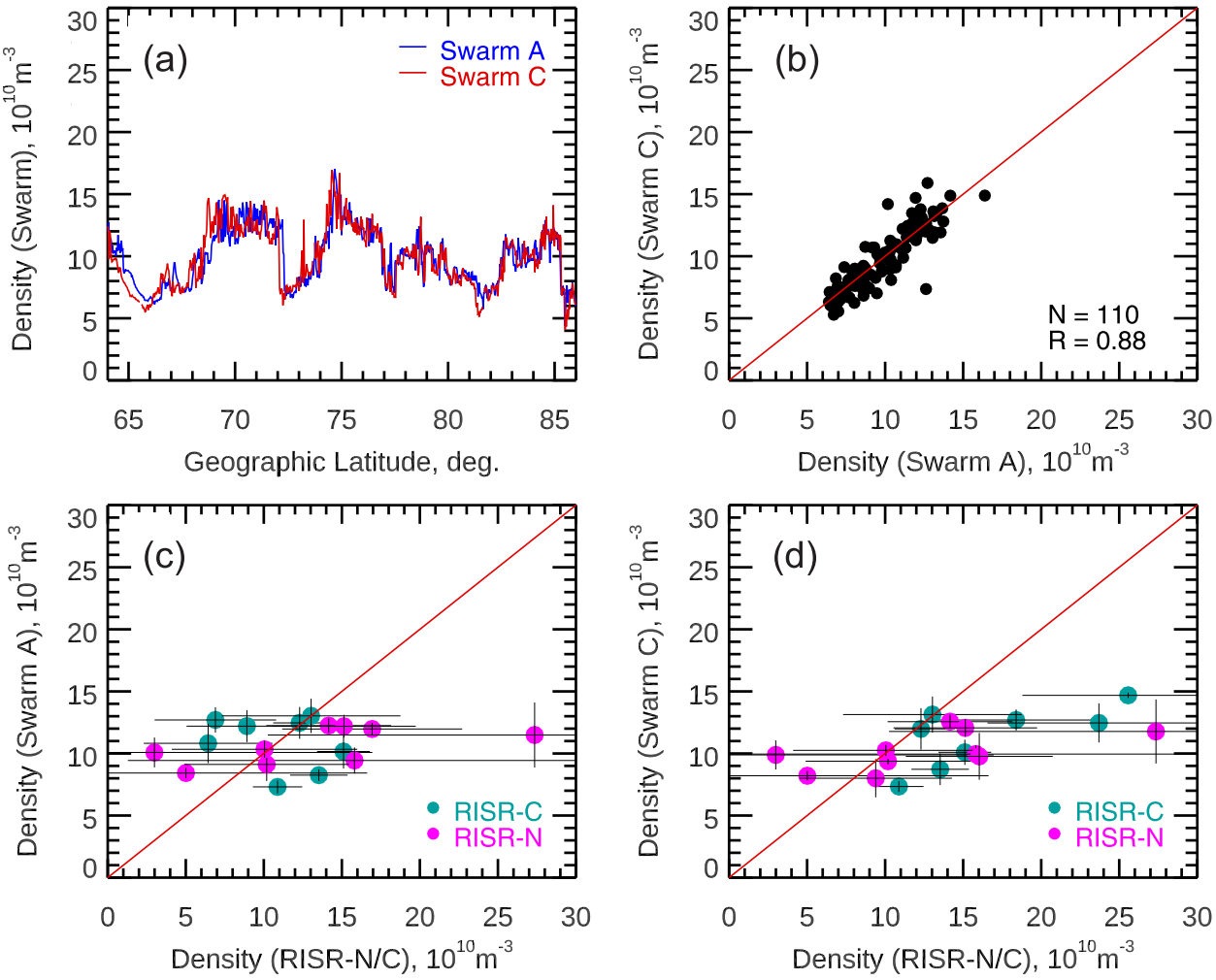

Figure 4.2: Electron density measured by Swarm A and Swarm C as they travel near Resolute Bay, Nunavut on 12 October 2016 and electron density measured by the RISR incoherent scatter radars. (a) Electron density according to Swarm A (blue) and C (red) plotted versus geographic latitude. (b) The same data as in (a) but presented as a scatter plot of individual measurements taken as the median value in a bin of 0.2° latitude. The red line is the bisector of perfect agreement. (c) Scatter plot of the electron density measured by Swarm A against ISR electron density at the conjunction points for the selected pass. The horizontal bar for each point is the error in ISR measurement while the vertical bar for each point is the standard deviation in each bin of Swarm data. (d) The same as (c) but for the Swarm C satellite.

Figure 4.2c is a scatter plot of $N_e^{Swarm\ A}$ versus N_e^{RISR} while Figure 4.2d is a scatter plot

of $N_e^{Swarm\ C}$ versus N_e^{RISR}. Many points in Figures 2c and 2d are located not far from the bisector of the perfect agreement but several points are significantly removed, both ways, with Swarm values being larger and smaller than those measured by the ISRs, for N_e^{RISR} >10×10^{10} $m^{-3}$and N_e^{RISR} <5×10^{10} m^{-3}, respectively. The disagreements are not unexpected since there are indications of strong polar cap patches presence, as discussed above. In a patchy ionosphere, matching in space and time becomes a challenging task.

Focusing on possible reasons for strong disagreement between the measuring systems, it was realized that the straight point-by-point comparison, as it is done in Figures 4.1 and 4.2, is not the only way to perform a comparison. On top of the separation in time and space between the radar and satellite measurements and their spatial coverage, the data have quite different integration times. In addition, while investigating individual ISR profiles, it was discovered that they often show significant variability with large error bars at altitudes above the F region peak. This is particularly evident in 1-min ISR data.

One example of a typical situation is given in Figure 4.3a for the event considered in Figures 4.1 and 4.2 and for Swarm C passing RISR-N beam #3. Here one can see that the RISR error bars at ~400-500 km are at least two times larger compared to those at 250 km. Figure 4.3a also shows the Swarm C electron densities recorded over the period when the satellite satisfied the criteria of proximity (blue points). The measured Swarm and RISR-N electron densities are also shown in Figure 4.3b versus geographic latitude. For the point-by-point comparison of Figures 4.1 and 4.2, the ISR measurement at the point closest to the satellite (at 455 km) was selected. However, one can notice that this approach might be not the ideal characterization of the real electron density in the ionosphere. This is because, while the Swarm values are consistently in the range of (8-10)×10^{10} m^{-3}, the RISR reported values at closest heights of 439 km and 470 km are much smaller than that reported for the height of 455 km, (3-5)×10^{10} m^{-3} versus 7×10^{10} m^{-3}. In addition, all three ISR measurements have large error bars. The selection of only one closest in location point seems to be not very convincing.

Another situation is illustrated in Figures 4.3c and 4.3d. In Figure 4.3c, there is a gap in the ISR-reported electron density values near and above the height of Swarm B measurements. In Figure 4.3d, this is for the data of Figure 4.1 with one of the yellowish points, RISR-C shows anomalously large density at the height selected for the comparison and also at the next height below it. These two points are away from the general trend in the electron density height profile and well might be measurement artifacts. To avoid obvious outliers in the data, all measurements with the electron density or errors above 250×10^{10} m^{-3} were discarded.

One way to improve the certainty of the selected ISR measurements is to consider only points in ISR electron density profiles with low errors. In the subsequent analysis, a

requirement that errors be below 50% of a measured value was implemented. Although this is a less stringent condition compared to the 15% limit in Lomidze et al. (2018), imposing stronger restrictions reduces data availability dramatically. The data set obtained in this way will be referred to as data set 1. It consisted of 200-300 points for each satellite. We comment that considering almost all the available measurements does not change our conclusions drawn from this type of analysis as removed points are mostly for low electron densities of $<5\times10^{10}$ m^{-3}.

An alternative approach is to consider "smoothed" electron density height profiles by fitting the actual raw measurements of ISR electron density with a best-fit line based on most of the measurements available above the F region peak. In this way, data set 2 was created. This data set is at least twice as large as data set 1.

Figures 4.3a and 4.3c-e give examples of the fitted curves, black lines, overlaid with the original measurements. In all cases, the best fit profile seems to reasonably characterize the trend in the electron density variation with height and, perhaps, better reflects the real electron density in the ionosphere on a large scale. Recall that the ISR data are averaged over altitude range gates of ~25 km (although ~50 km along a radar beam). Note that the electron density described by the fitted profiles can be smaller or larger than the raw ISR measurement at a specific height. Figure 4.3e gives an example of a case when the fitted profile values correspond to larger values than the original ones. We expect that, generally, no systematic trend was introduced while creating the data set 2. In all cases of Figures 4.3a and 4.3c-e, the fitted lines agree better with the median of Swarm measurements (red vertical line) than the closest ISR single measurement. Certainly, this was not the case for some other conjunctions.

We note that the tilt of the RISR beams introduces some uncertainty into the profiles involved when strong horizontal electron density gradients are present. For the events considered, the electron density variations along the Swarm track (latitude) were mostly smooth. This was considered as a sign of smoothness of the ionosphere for the events under investigation. The primary intent of the fitting procedure is to replace the spikes in the electron density with values that are consistent with those measured above and below the heights of a spike.

Analytical description of the RISR electron density height profiles above the F region peak is a challenging task. Recently, some progress has been achieved in the analytical description of the electron density profiles in the topside ionosphere (e.g., Pignalberi et al., 2020), but the problem encountered stemmed from the fact of significant variability of the ISR profiles. Attempts to work with the Chapman-like function or NeQuick function described by Coïsson

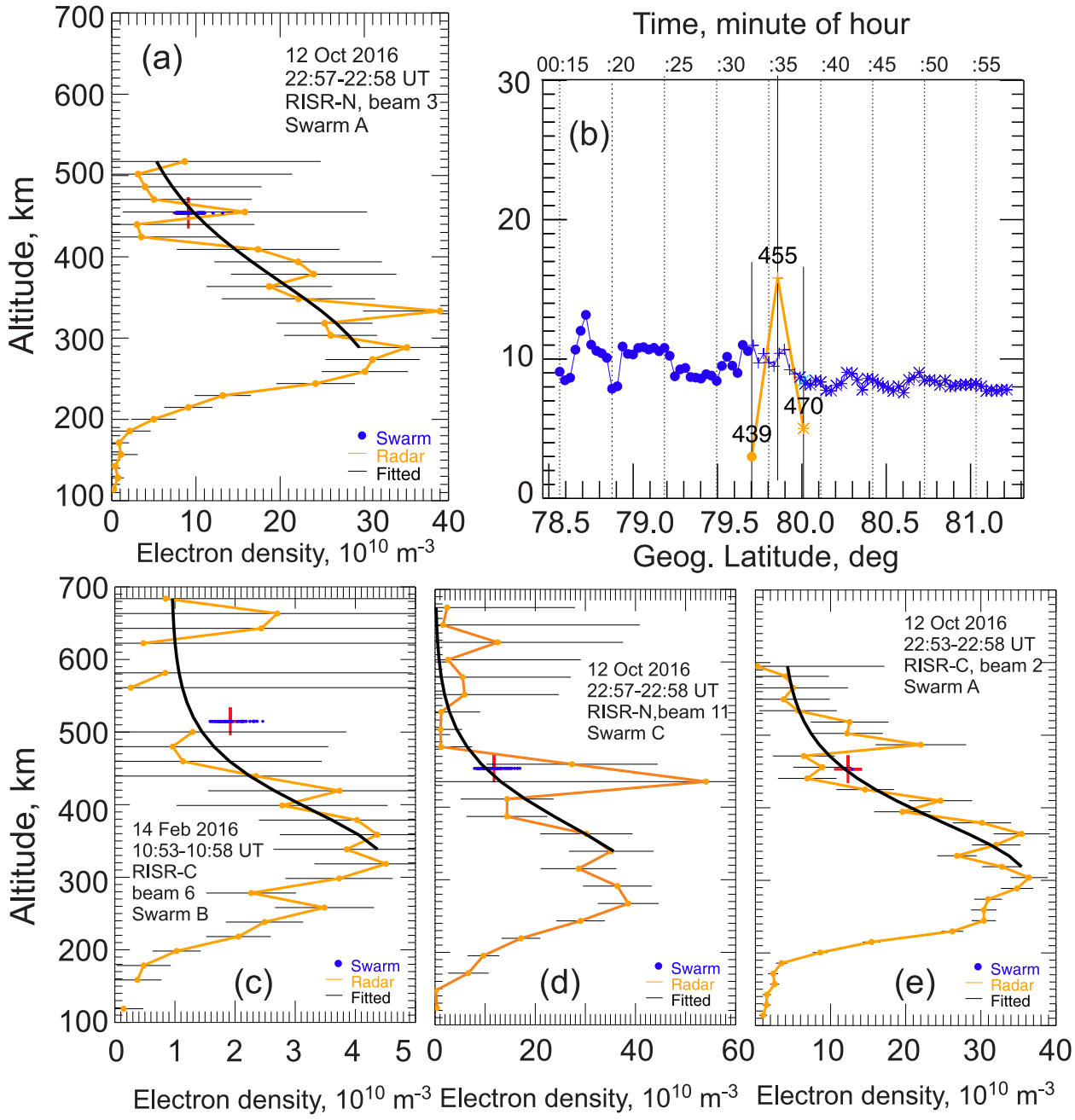

Figure 4.3: (a), (c)-(e) Electron density profiles as measured by the Resolute Bay incoherent scatter radars (ISR), solid beige circles with horizontal bars representing the error of measurements, and the electron density according to Swam Langmuir Probe measurements at closest locations (less than 200 km separation) best matching ISR measurement interval in time (blue circles). The median value of the Swarm measurements is marked by a red vertical bar. The black line is the best fit line to the RISR electron density profile, as described in the text.

et al. (2006) were unsuccessful because the electron density was falling with height too fast to accommodate the observed values at the heights above 500 km. It was determined that

varying the r parameter, as in the approach of Coïsson et al. (2006), did not improve the fit. After several trials, it was decided to use a modified function by Coïsson et al. (2006) in the form:

$$N_e = k_1 + 4\frac{N_m F2 \exp(Z^{k_2})}{(1+\exp(Z))^2} \qquad Z = \frac{z - h_m F2}{H\left(1 + \frac{rg(z-h_m F2)}{rH+g(z-h_m F2)}\right)} \tag{4.1}$$

where $N_m F2$ is the electron density at the F region peak achieved at the height $h_m F2$, r=100 (selection by Coïsson et al. (2006)) and g, H, k_1 and k_2 are free parameters. The free parameters were determined by the least-square minimization of a selected curve and actual data, for each profile separately. The introduction of the parameter k_1 allowed the profile to be placed in such a way that the electron density was not getting close to zero at the largest heights of measurements.

4.4 Results for multiple events

This study considered RISR radar observations between 2014 and 2019. Figure 4.4 shows data for Swarm-radar conjunction occurrence in terms of the time of a day (for RB, LT=UT-6) and year, separately for RISR-C and RISR-N. For both radars, prevailing were conjunctions in the early afternoon and late dusk-midnight sectors. In terms of season, summer data were limited. The above limitations are due to radar scheduling aimed at the investigation of the polar cap ionosphere under dark conditions.

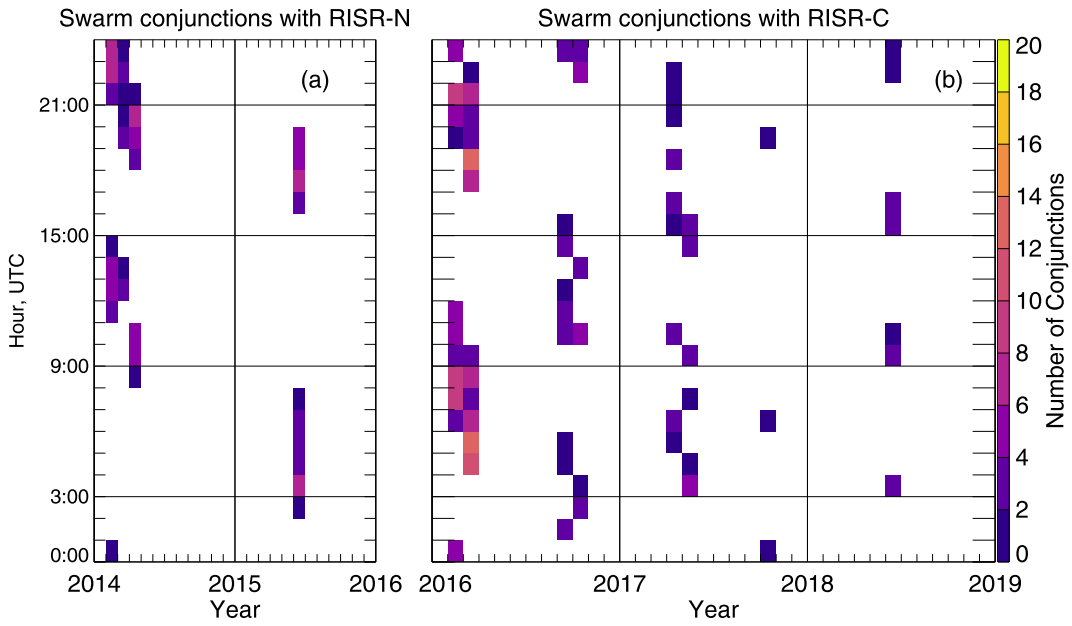

Figure 4.4: Data on the occurrence of conjunctions between Swarm (for all three satellites) and (a) RISR-North and (b) RISR-Canada incoherent scatter radar measurements.

4.4.1 Statistics for the ratio of electron density measured by Swarm and RISR radars

For presenting statistics of Swarm-RISR data, it was decided to consider the electron density, a basic parameter of interest for ionospheric physicists, rather than the plasma frequency as was done by Lomidze et al. (2018). Accordingly, a ratio R, $R = N_e^{Swarm}/N_e^{RISR}$, was computed separately for the data sets 1 and 2. Below, where appropriate, plasma frequency values are reported so as to facilitate a comparison of our results with those reported by Lomidze et al. (2018).

Figure 4.5 gives histograms of R values for each satellite separately while performing the point-by-point comparison, data set 1. The histograms include all conjunctions satisfying the proximity criteria in space and time for each satellite. To characterize the histograms quantitatively, the median (μ) and the standard deviation (σ) were obtained. The values of μ and σ are presented in the top right corner of each panel.

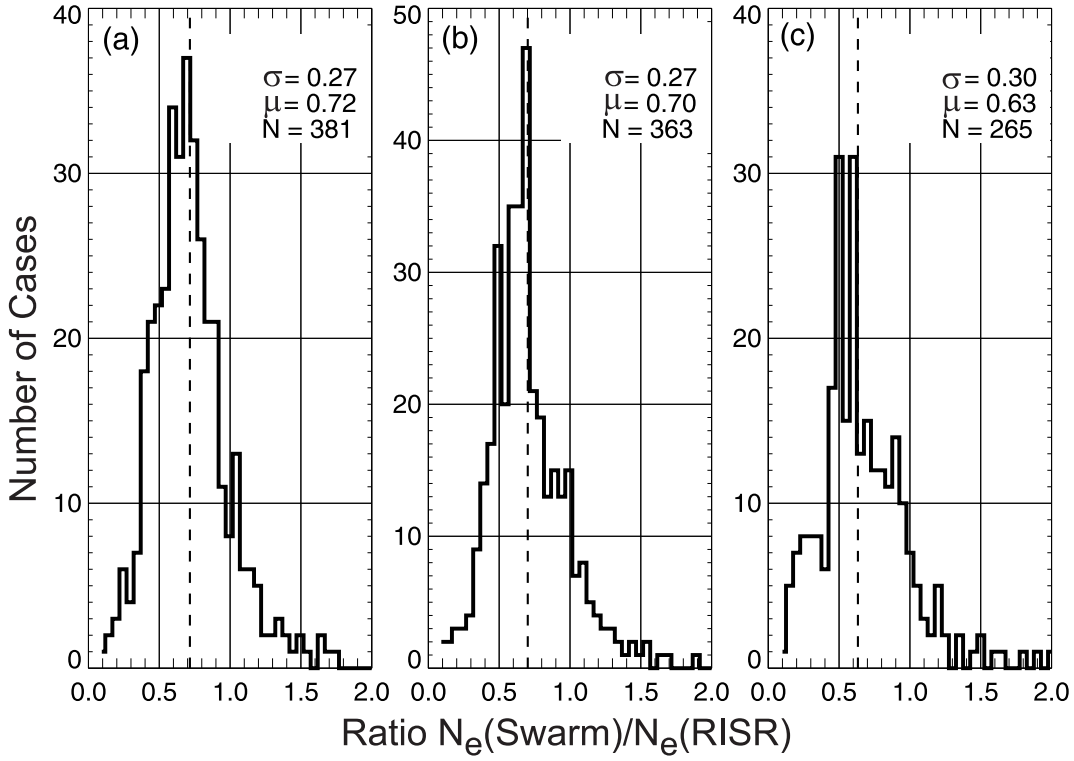

Figure 4.5: Distributions of the ratio $R = N_e^{Swarm}/N_e^{RISR}$ for the (a) Swarm A, (b) Swarm C and (c) Swarm B satellites for all radar-satellite conjunctions (2014-2019) while point-by-point comparison (data set 1) is made. Each histogram is characterized by the median value (μ) and the standard deviation value (σ). The values for μ and σ are reported in the upper right corner.

According to Figures 4.5a and 4.5b, the ratios for Swarm A and C are consistently maximized at μ ~0.7 with the standard deviation σ of ~0.3. For Swarm B (Figure 4.5c), the maximum is smaller ($\mu = 0.63$) and the distribution is slightly broader. The values of μ and σ are presented in Table 4.1, top row. These results can be interpreted as, broadly speaking, the Swarm electron density values are systematically smaller than those measured by the radars by ~30-35%.

A similar analysis has been performed for Swarm-radar data set 2. The results are presented in Table 4.1, bottom row. In this case, values μ are higher, 0.75-0.80, while the spread of the data (values of σ) is slightly larger.

Table 4.1: The median value μ and the standard deviation σ for a histogram distribution of the ratio $R = N_e^{Swarm}/N_e^{RISR}$ for the point-to-point satellite-radar data comparison (data set 1) and the comparison that used the height-fitted RISR electron density profiles (data set 2). Also presented is the number of points for each distribution.

	Swarm A			Swarm C			Swarm B		
	μ	σ	points	μ	σ	points	μ	σ	points
Set 1	0.72	0.27	381	0.70	0.27	363	0.63	0.30	265
Set 2	0.80	0.29	566	0.79	0.31	545	0.75	0.32	545

An attempt has been made to assess the Swarm-RISR differences in terms of the time of day. Data for all three satellites and both ISRs were merged into one data set to have reasonably large statistics. Four time sectors were introduced as follows: day (15-21 UT), dusk (21-03 UT), night (03-09 UT) and dawn (09-15 UT). Ratio R was computed and the histograms were built, similar to the procedure described above. The results of the histograms' assessment are presented in Table 4.2. The highest values of the electron density ratio R were found to be for dusk while the smallest Rs were found to be for nighttime and dawn.

Table 4.2: The median value μ and the standard deviation σ for a histogram distribution of ratio $R = N_e^{Swarm}/N_e^{RISR}$ for the point-to-point satellite-radar data comparison (data set 1) and the comparison that used the fitted RISR electron density profiles (data set 2). Also presented is the number of points for each distribution. Data for all three Swarm satellites were considered.

	Day, μ	points	dusk, μ	points	night, μ	points	dawn, μ	points
Set 1	0.68	276	0.72	247	0.70	317	0.69	169
Set 2	0.81	415	0.81	461	0.78	410	0.79	370

4.4.2 Trends in the relationship of Swarm and ISR radar measured electron densities

To assess further the degree of agreement between the Swarm and RISR electron densities the electron densities measured by each of the Swarm satellites and by the radars were presented as scatter plots in Figure 4.6 (black circles). Here the top three panels are for the point-by-point comparison (data set 1) and the bottom three panels are for the fitted electron density profiles comparison (data set 2).

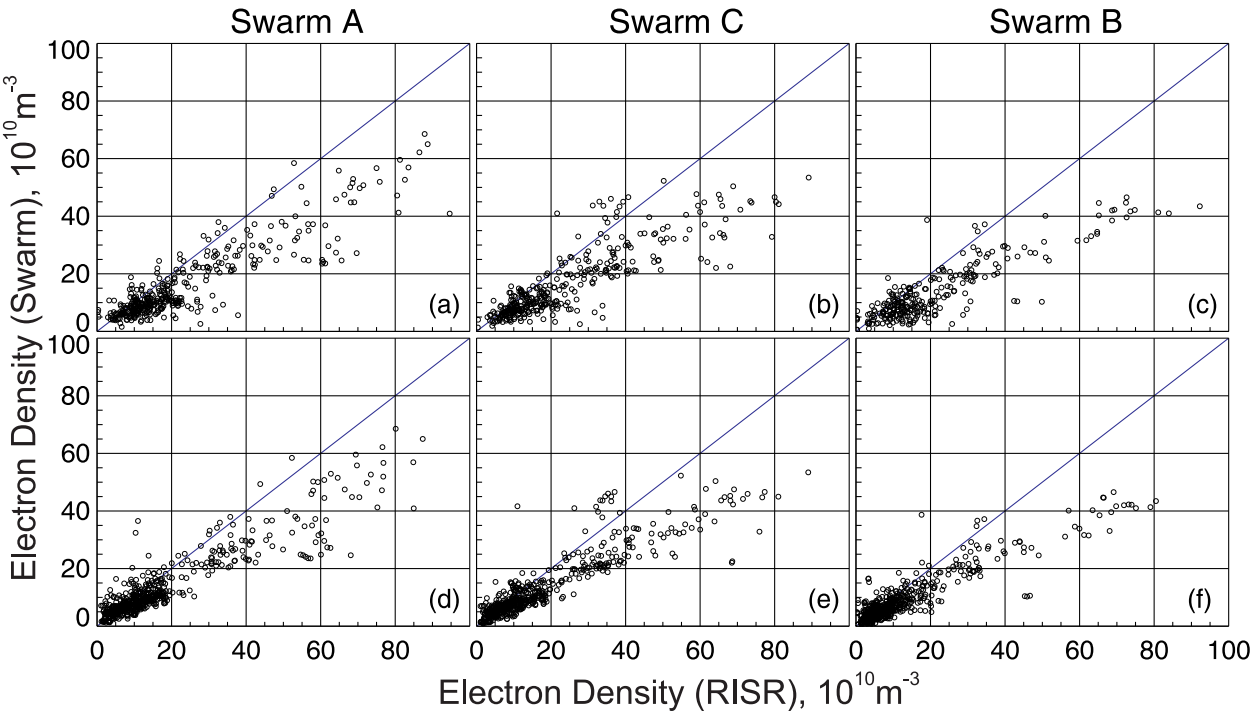

Figure 4.6: Electron density measured onboard the Swarm satellites versus electron density measured by the Resolute Bay incoherent scatter radars RISR-C/N at close locations and at close time. The left, center and right panels are for Swarm A, C and B, respectively. The top row panels are the direct point-by-point comparisons (data set 1) while the bottom row panels are comparisons by considering RISR electron density height profiles fitted by a curve (data set 2).

It should be noted, when comparing with Figure 4.6 with Figure 4.2, that dataset 1 is composed of 5 minute filtered data while the data in Figure 4.2 is unfiltered and the RISR-N data are 1 minute data.

One common feature of the data in Figure 4.6 is that despite data scatter and underestimation by Swarm, the points are clustering close to the bisector of perfect agreement for electron densities between ~3×10^{10} m^{-3} and ~15×10^{10} m^{-3} corresponding to plasma frequencies f_p between 1.5 and 3.5 MHz. At progressively higher electron densities, the points

deviate from the bisector more, especially for $>30\times10^{10}$ m^{-3} ($f_p > 5$ MHz). The number of large-value points is low. We note that most of these points came from Swarm conjunctions with RISR-N and for the Swarm B satellite flying at larger heights. The other visible feature of the data in Figure 4.6 is that the Swarm electron densities are slightly above what radars measure at $N_e < 5\times10^{10}$ m^{-3} ($f_p < 2$ MHz), however, the effect is subtle.

All plots of Figure 4.6 show an increasing trend visually identifiable as a linear one. To confirm this judgment,Swarm density data were binned using the paired RISR density value. Figure 4.7a gives an example of the analysis for Swarm C data (presented in Figure 4.6b). Here bins of the ISR electron density with a size of 5×10^{10} m^{-3} were introduced. The bins were judged as statistically significant if more than seven measurements were available. The vertical bar around each median value of Swarm-measured electron density is the standard deviation of the Swarm values within the RISR bin (reflecting the variability of measurements).

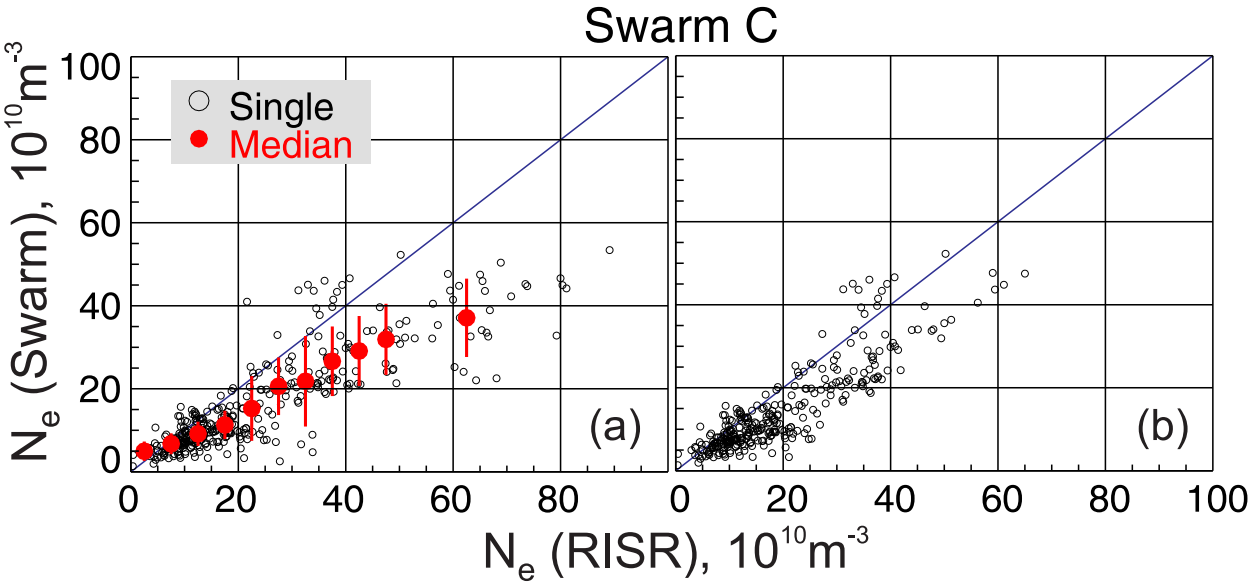

Figure 4.7: Electron density measured onboard Swarm C satellite (N_e^{Swarm}) versus electron density measured by the Resolute Bay incoherent scatter radars RISR-C/N (N_e^{RISR}) at close locations and at close time. Data set 1 was considered (see the text). (a) All available conjunctions are considered. Red dots are medians of N_e^{Swarm} (Swarm C) in bins of N_e^{RISR}. Vertical bars are standard deviations of N_e^{Swarm} in each bin of N_e^{RISR}. (b) The same data as in (a) but filtered by applying the median absolute deviation technique (see the text).

Alternatively, to articulate the linear trend in the data of Figure 4.6, the median absolute deviation (MAD) technique (e.g., Rousseeuw & Croux, 1993) as applied, Figure 4.7b. Here the absolute value of the difference between the Swarm and RISR densities for each conjunction was calculated as well as the standard deviation. This was applied to each data set and for

all three satellite data separately. Then all the points with the absolute difference between the measured electron densities of more than 3 standard deviations were rejected and a new MAD-filtered data set for each satellite was formed. The new data sets are about 75% of the original ones. Figure 4.7b compares Swarm and ISR data after application of MAD filtering. Stretching of the points near the bisector of perfect agreement is recognizable.

Since the Swarm-based electron density in Figures 4.6 and 4.7 shows close to a linear relationship with the electron density measured by the ISR radars, the linear regression lines were applied to the data. The regression analysis has been done in several ways. The slopes and the y-offsets of the linear fit lines are presented in Table 4.3, for each satellite and data sets 1 and 2 separately.

The first set of parameters, presented in rows 1 and 2, is for the linear fit that assumes that the ISR densities are known with high precision and no errors are given in Swarm LP measurements, for all the points available (such as those shown in Figure 4.6). We then performed a similar linear fit analysis to measurements with ISR electron densities between 5×10^{10} m^{-3} and ~40×10^{10} m^{-3}, the parameters in rows 3 and 4. In this way, the relationship of measured electron densities for the limited data sets best covered in terms of conjunctions was assessed (since the amount of high and low electron density points is more limited).

Table 4.3: Coefficients of a linear fit $N_e^{Swarm} = a \cdot N_e^{RISR} + b$ to a scatter plot of electron density measured by Swarm versus electron density measured by RISR-C/N radars for data sets 1 and 2. Also presented are the number of points (N) for each plot and the Pearson correlation coefficient (r). Values of b are given in units of 10^{10}m^{-3}.

		Swarm A				Swarm C				Swarm B			
		a	b	N	r	a	b	N	r	a	b	N	r
1	Set 1	0.58	2.64	381	0.88	0.52	3.98	363	0.84	0.53	2.37	265	0.88
2	Set 2	0.59	3.08	566	0.90	0.54	3.64	545	0.88	0.57	1.92	545	0.92
3	Set 1, limited	0.61	2.09	277	0.75	0.63	1.71	259	0.81	0.59	2.04	189	0.74
4	Set 2, limited	0.66	2.25	373	0.82	0.62	2.55	347	0.87	0.65	1.81	263	0.84
5	Set 1	0.62	1.57	381	0.88	0.56	2.77	363	0.84	0.56	1.60	265	0.88
6	Set 2	0.63	2.42	566	0.90	0.58	2.96	545	0.88	0.60	1.59	545	0.92
7	Set 1, limited	0.76	-0.51	277	0.75	0.73	-0.22	259	0.81	0.74	-0.66	189	0.74
8	Set 2, limited	0.77	0.66	373	0.82	0.67	1.67	347	0.87	0.74	0.48	263	0.84

The next assessment was done by keeping in mind that the difference in the temporal and spatial resolutions of the instruments brings some uncertainty to ISR measurements despite

that an individual measurement can be of high quality (low error). In this approach, linear fit lines were applied by considering deviations of the Swarm and ISR electron density values in the direction perpendicular to the fit line (Sampaio, 2006), rows 5, 6 and 7, 8 for all data points and for the limited band of RISR electron densities (5-40)$\times 10^{10}$ m^{-3}, respectively.

The parameters of the linear fits, presented in Table 4.3, allow us to make several conclusions. First of all, the slope of the lines varies, from a low of 0.52 to a high of 0.77. Larger values are found for the limited data sets with better conjunction coverage and data sets 2 for which "smoothed" over height electron density profiles were considered. The median of all the slopes reported in Table 4.3 is 0.62. The y-offsets in Table 4.3 also vary significantly, with the median value of 1.8×10^{10} m^{-3}. The Pearson correlation coefficients for the fits are on the order of 0.85. We note that a linear fit analysis performed on MAD-filtered data sets shows much higher slopes, up to 0.9 and higher correlation coefficients, up to 0.9.

On the final step in the assessment of the data in Figure 4.6, linear fits were performed while considering errors along the x and y axes for data set 1 according to the procedure given by (York et al., 2004). In this case, errors in RISR measurements were available and the standard deviations in matched Swarm measurements were adopted as a proxy for the errors in measurements on the satellites. Obtained dependencies have the following coefficients for Swarm A, C and B dependencies, respectively: $a = 0.69(\pm 0.01); b = 1.51(\pm 0.15)$, $a = 0.67(\pm 0.01); b = 1.49(\pm 0.13)$, and $a = 0.68(\pm 0.01); b = 1.39(\pm 0.04)$ with b values given in units of 10^{10}m^{-3}. The numbers in these fits show that the slopes of the linear fit lines are robustly in the range of ~0.68 indicating ~32% smaller Swarm-reported electron densities. This is somewhat different from those in row 1 of Table 4.3, but not dramatically.

4.5 Discussion

Lomidze et al. (2018) compared the electron density measured by Swarm LPs at middle and low latitudes with ionosondes and incoherent scatter radars and with satellite radio occultation measurements at all latitudes. They formulated results in terms of the plasma frequency, to reduce the spread of the data so that the plots (for example, their Figure 1) showed a clear linear dependence with the correlation coefficients of ~0.98 and with the slopes of the best linear fit line on the order 1.1 (or 10% smaller Swarm LP plasma frequencies). In the present study, the data are presented in terms of the electron density, and, in addition, the Swarm electron densities are plotted along y axes. To compare our results with those by Lomidze et al. (2018), their data were recast and reprocessed in terms of electron densities and the typical slope was found to be about ~0.82 indicating the ~18% underestimation for the Swarm LP densities. It is important to realize that the Lomidze et al. (2018) data set includes

a broad range of possible densities from 4.4×10^{10} m^{-3} (f_p~2 MHz) to 100×10^{10} m^{-3} (f_p~13 MHz) although the bulk of the data was in the range of ~(5-50)$\times10^{10}$ m^{-3}. We would like to note that although the data of Figure 1 in Lomidze et al. (2018) are characterized by a linear dependence, a somewhat stronger underestimation effect is seen for plasma frequencies >8 MHz (>~8×10^{10} m^{-3}), their Figures 1 and 3.

It is interesting that the earlier work by McNamara et al. (2007) also indicated that the LP instrument on the CHAMP satellite showed generally smaller values (their Figure 3). This was particularly evident for plasma frequencies of 4-8 MHz, typical for the polar cap ionosphere. What was not emphasized is that in this range of plasma frequencies, the differences were on the order of 1 MHz, which translates to the LP underestimation in terms of the electron density by ~25%, the number consistent with the number in Lomidze et al. (2018), as mentioned above.

Both data sets 1 and 2, produced and investigated in the present study, cover the low end of values considered by Lomidze et al. (2018), and some points are even below their lowest limit. The data spread is much more significant in our case. This is not a surprise because the polar cap ionosphere generally has lower densities (Themens et al., 2017; Themens, Jayachandran, McCaffrey, et al., 2019) and it is much more patchy (e.g., Chartier et al., 2018; Moen et al., 2007). For the linear fit line applied to all the points in Figure 4.6, a typical slope was found to be 0.62, which is a lower dependence than that of Lomidze et al. (2018).

It is symptomatic that both our comparison and that by Lomidze et al. (2018) for the Swarm satellites and McNamara et al. (2007) for the CHAMP satellite showed "underestimation" of the electron density by the LP instruments. Lomidze et al. (2018) cited the paper by Oyama and Hirao (1976) who showed that the surface contamination of LP electrodes can result in a decrease of the current through the probe and thus in a lower reported electron density. Furthermore, it was expected that the effect is more pronounced at larger electron densities.

The surface contamination effect can occur for the LPs on the Swarm satellites. In this respect, interestingly enough, the Swarm-ISR differences are progressively larger at larger densities (our Figure 4.6), consistent with the expectation. In this scenario, one can also expect that the Swarm "underestimation" would be stronger at later stages of the mission with a general degradation of the instrument. This hypothesis can be tested by working with other ISRs that have longer observational periods. Note that the larger underestimation effect reported in the present study is for the data collected several years later as compared to the data considered by Lomidze et al. (2018).

Samaniego et al. (2020) reported on a possibility of underestimations of plasma electron density by LPs in a case of high plasma flow speeds with a probe being larger than the Debye

length in the plasma. They argue that the electron density in the wake of the LP sphere can be depleted under these conditions, leading to a lower current through the probe. To what extent their analysis applies to the Swarm instruments is difficult to estimate. This is because although the Swarm LPs operate at a high Mach number (6), the probe size is comparable with the Debye length.

In this respect, more conclusive is a recent paper by Resendiz Lira and Marchand (2021), who considered a realistic model of the Swarm LP probe and employed 3-D kinetic simulations to infer the current collected by the probe under typical conditions. One important aspect of their approach was allowing for the presence of light ions which is expected in real situations but not accounted for while the standard LP measurements are considered. They showed that the difference between the electron density inferred under pure O^+ plasma and plasma mixed with lighter ions can be on the order of 20%, which is significant. They also confirmed that the current collected by an LP is always reduced in the wake of the probe under the negative floating potential which is typical for the conditions of electron density derivation in the Swarm experimentation. These results hint that a more substantial electron density underestimation in Swarm measurements at high latitudes can be expected.

So far, discussion has focused on the smaller Swarm-based electron densities in terms of operational features of the LP instruments. Undoubtedly, there are some features in RISR measurements that have to be taken into consideration as well. Generally, the radar calibration process is designed to have no statistical bias in measurements for an extended period of a specific experiment. For WD experiments more than one day of RISR-CADI data with 15-min time resolution is usually considered. The median of the histogram distribution for the ratio of the RISR-reported to CADI-reported maximum electron densities is required to be close to 1. However, the distributions have certain width so that about 10% larger or smaller RISR electron densities are present in a data set for every radar calibration run. This implies that for specific RISR-Swarm conjunction, there might be a minor difference on the order of 10%. In this view, to arrive at a well-founded conclusion, a statistically large RISR-Swarm data set is needed.

Another important consideration is the fact that the quality of ISR spectrum fits (and thus electron density determination) depends on the strength of returned signals, and this is particularly critical for the topside measurements in the generally low-density polar cap ionosphere. For the case of RISR radars, spikes in the electron density profiles above the F layer peak are widespread. We showed the spike in the electron density limited to the heights close to the satellite flying height in Figure 4.3d. The events with exceptionally strong spikes were filtered out during the creation of both data sets but profiles with moderate spikes, as shown in Figure 4.3d, were still allowed. This concern was one of the reasons for the creation

of data set 2 with smoothed electron density profiles. Interestingly enough, data set 2 (fitted electron density profiles) shows slightly better agreement with Swarm measurements than data set 1 (point-by-point comparison) which can be affected by the spikes in RISR data.

Even though our study focuses on low-density plasma in the high-latitude ionosphere and has statistics 2-3 times larger than that for ISRs in Lomidze et al. (2018), who used stricter criteria (such as data with errors <15%, zenith-pointing ISR measurements, and only during geomagnetically quiet conditions) for selecting coincident Swarm and ISR data and wider density ranges, the results of the two studies are generally consistent. Lomidze et al. (2018) used COSMIC radio occultation data to compare the two measurements for the low electron densities ($f_p \leq$3 MHz) and did not find any significant underestimation by Swarm. This is different from the results of this study, which shows that the Swarm LPs underestimate the measurements also for low electron densities. A possible explanation could be related to the lower accuracy of COSMIC data for low densities, as outlined in Lomidze et al. (2018).

The analysis of the data sets 1 and 2 drew comparable conclusions despite quite a different approach to handling the ISR data, either considering a point of immediate "conjunction" or by considering a smoothed density profile above the F region peak. This indicates that the relationships presented in Fig 4.6 reflect the real differences between the instruments. At the same time, however, the derived linear dependencies are occasionally characterized by, though still high but somewhat reduced, correlation coefficients (Table 4.3).

The results obtained in this paper can be re-evaluated in the future by including more data, and particularly those for higher electron densities. That will help in making a better assessment of differences between the instruments in the entire range of possible electron densities. The constant presence of polar cap patches over RB makes the data comparison relatively more difficult than at other locations. Yet, for many events considered in this study, the Swarm-measured electron density was not changing strongly while the satellites were crossing RISR beams, unlike what was seen in Figure 4.1.

In the process of examining the data, interesting cases of the electron density variations were identified with sharp and strong changes of the electron density as reported by Swarm C and later on by Swarm A. One would generally expect the edges to be detected at slightly different geographic locations because the ionospheric plasma is $\vec{E} \times \vec{B}$ drifting. With a typical drift of 0.5 km/s and satellite time delay of 7 s, up to 4 km separation in the location of identified "edges" is expected. In many cases, the separation was much larger, on the order of 50 km. This implies that often the satellites crossed the ionospheric patches at a small angle to a sharp edge of patches.

4.6 Summary and major conclusions

In this Chapter, the consistency in electron density measurements by two independent instruments, the Swarm satellites and the incoherent scatter radars RISR-C/N in the Resolute Bay area, was investigated. Joint data collected between 2014 and 2019 for more than 200 satellite passes were considered. The comparison resulted in the following conclusions:

1. Currently available Swarm electron density values are smaller than those measured by the RISR incoherent scatter radars for observations in the vicinity of Resolute Bay, Canada, in the polar cap. The effect is stronger for observations in the midnight and dawn sectors.

2. The comparison of electron densities indicates that Swarm values are lower than those measured by RISR radars by ~35%. For a scatter plot of Swarm versus RISR electron density, the best linear fit line has a typical slope of ~0.62 and the y-offset of ~2×10^{10} m^{-3}. This result is, overall, consistent with those reported by Lomidze et al. (2018) although the reported slopes are smaller in our case. The agreement between the satellite-radar data is better for the electron densities between ~5×10^{10} m^{-3} and ~40×10^{10} m^{-3}, corresponding to plasma frequencies between 2 and 6 MHz.

3. As the electron density increases, the underestimation of electron densities by Swarm compared to those measured by the RISR radars becomes progressively better.

Chapter 5

Electron density in the ionosphere over Resolute Bay as measured by RISR-C and predicted by the E-CHAIM statistical model

5.1 Introduction

E-CHAIM is a recently developed model of ionospheric plasma (Themens et al., 2018; Themens et al., 2017) focused on the Canadian High Arctic. It is an attempt to improve the quality of existing models such as the IRI family (e.g., Bilitza, 2018). The development of the model was introduced in Chapter 1. The model has been shown to perform well (Themens, 2018; Themens et al., 2018; Themens, Jayachandran, & McCaffrey, 2019; Themens, Jayachandran, McCaffrey, et al., 2019), but assessment of the model is still incomplete. An example of the ongoing assessment is a recent paper accepted in Space Weather, in which the author participated (Themens et al., 2021). The paper assesses E-CHAIM performance in terms of total electron density content (TEC) and investigates the differences between the model and the TEC data from multiple GPS receivers.

In this chapter the results of comparing E-CHAIM electron density predictions to the electron density measured by the RISR-C radar at Resolute Bay are presented. The work is limited and exploratory, and, as such, only RISR-C data from 2016-2018 are considered. Reasonable agreement between RISR-C and E-CHAIM is expected, as the model was validated against RISR-N during development (Themens, 2018).

The investigation of the differences between E-CHAIM and RISR-C is founded on three main justifications. The first is that, given the minor role of RISR-C data in the development of the model, RISR-C contributions would be overwhelmed by the other data sources. The second is that studies show that IRI electron density predictions and electron density observed by the

Svalbard ISR can differ by more than a factor of two (Bjoland et al., 2016) for some heights and some seasons, while studies show that the differences between IRI and E-CHAIM are not typically as large (Themens et al., 2018). More work comparing E-CHAIM and RISR-C could shed light on the reason for this discrepancy. A third motivation is that the model is periodically updated and, consequentially, should be periodically reevaluated.

5.2 Average ionospheric electron density distribution over Resolute Bay

As described in Chapter 1, ionospheric electron density varies significantly at the high latitudes. This variance is the result of many factors which have been under study for many years (e.g., Schunk & Nagy, 2009). However, despite the variance it is still useful to know the average or typical electron density. For example, knowledge of the background or "quiet" electron density values for a given location, season and time of day is necessary for identifying the effects of space weather. Space weather has been a field of active research in the past decade and can result in extraordinary parameters (Belehaki et al., 2015; Kutiev et al., 2013).

To this end, the work presented in this chapter is based on highly averaged RISR-C electron density measurements. The data used is the long pulse World Day mode scans with 5-minute integration time. Data with 1 minute resolution is available but was found to have larger measurement errors in general. Additionally, 5-minute resolution data are traditionally used to calibrate the radar and are the typical resolution given to users. Longer integration times would be suitable for the study, as E-CHAIM is a climatological model, but this would require special data processing which was not feasible in the time available for the work in this chapter.

The data were filtered in several ways. Consistent with the approach in Chapter 4, all measurements with a relative error of over 50% were excluded from the study. Since the relative error in RISR-C measurements can be large, especially at low densities and high altitudes, this has the side effect of limiting the number of data points with low densities and the number of points at high altitudes. Consequently, the study was constrained to altitudes between 100 and 500 km.

Additionally, the study was limited to RISR-C beams with an elevation angle of 45° or greater. This was done because the lower the elevation angle the further geographically from the radar the measurements are. A second reason is that low angle beams complicate analysis that uses altitude binning, as data points are spaced ~24 km apart along the beam, and, thus, the altitude change between data points depends on the elevation angle of the beam. This

can create a statistical bias in the bins as many points from low elevation angle beams, which have a small change in altitude between data points, will be included in low altitude bins. Additional bias could also be created at high altitudes where low angle beams do no reach.

Figure 5.1 shows the distribution of the measurements, that is range-gates, binned by year, hour and month. Seasonally, data are particularly limited in the winter, with no data available in November and December. Similarly, there is no data available for the months of July and August. Comparing between years, the only month with significant inter-year coverage is October, with all other months only having coverage in a single year. Unfortunately, RISR-C relies on generators which are expensive to fuel and only operates intermittently. Despite the limited temporal coverage constraining the scope of the study, data were assessed to be sufficient to proceed.

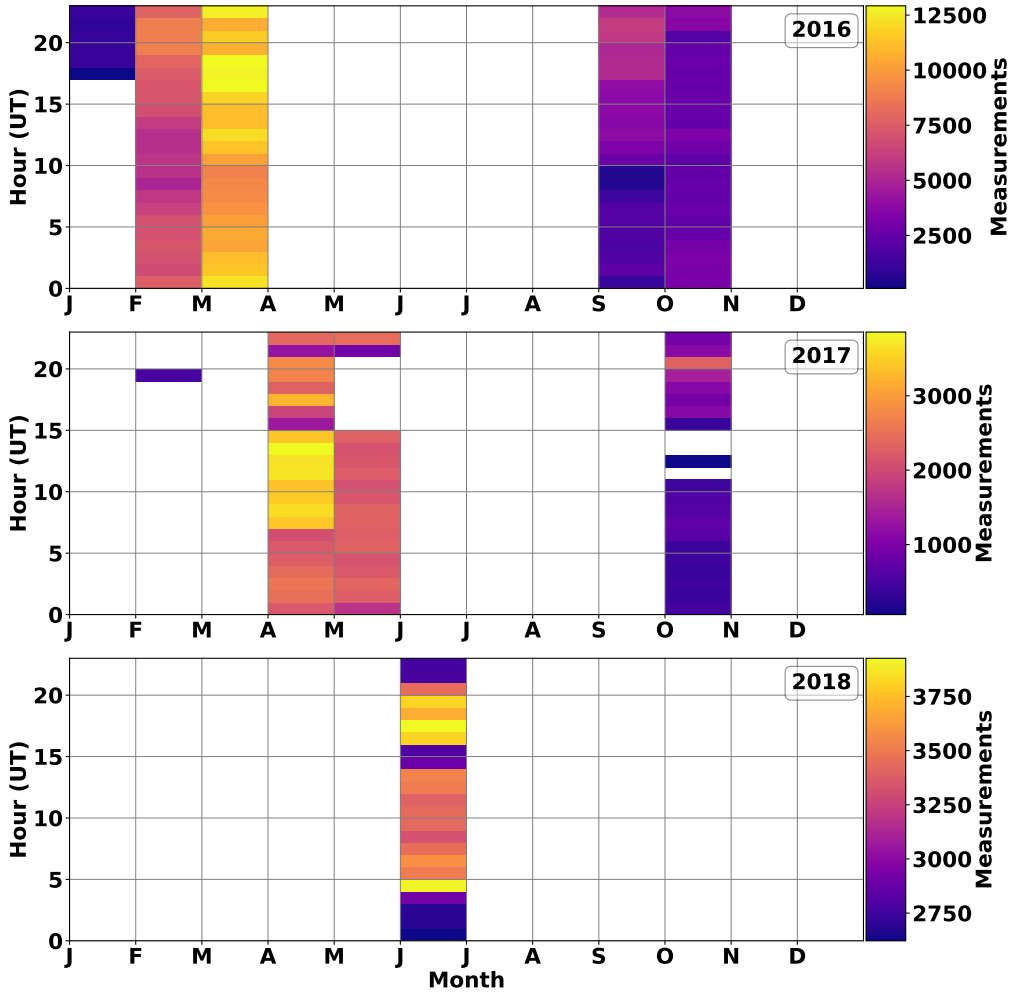

Figure 5.1: Hourly number of points of RISR-C WD mode measurements in various months of observations in 2016-2018. Measurements presented are filtered by relative error ($\leq 50\%$), by elevation angle of the radar beam ($> 45°$) and by measurement altitude (between 100 and 500 km).

The first step was to asses the typical electron density distribution over Resolute Bay. To this end, all of the electron density measurements presented were plotted in Figure 5.2. Figure 5.2 shows the median electron density binned by altitude, using 25-km bins, and hour. Additionally, the data were sorted into seasons of three months each. February, March and April were grouped into spring. The summer season was composed of the months May, June and July. Autumn was defined as August, September and October. Finally, the winter season was defined as November, December and January. Features in the electron density can be assessed in Figure 5.2 by further separating down each plot into one hour time sectors based on the local time of day. Recall that Resolute Bay is located at UT -6 so local noon is 18 UT and local midnight is 6 UT. The same time sectors for this Chapter were defined as in Chapter 4: day (15-21 UT), dusk (21-03 UT), night (03-09 UT) and dawn (09-15 UT).

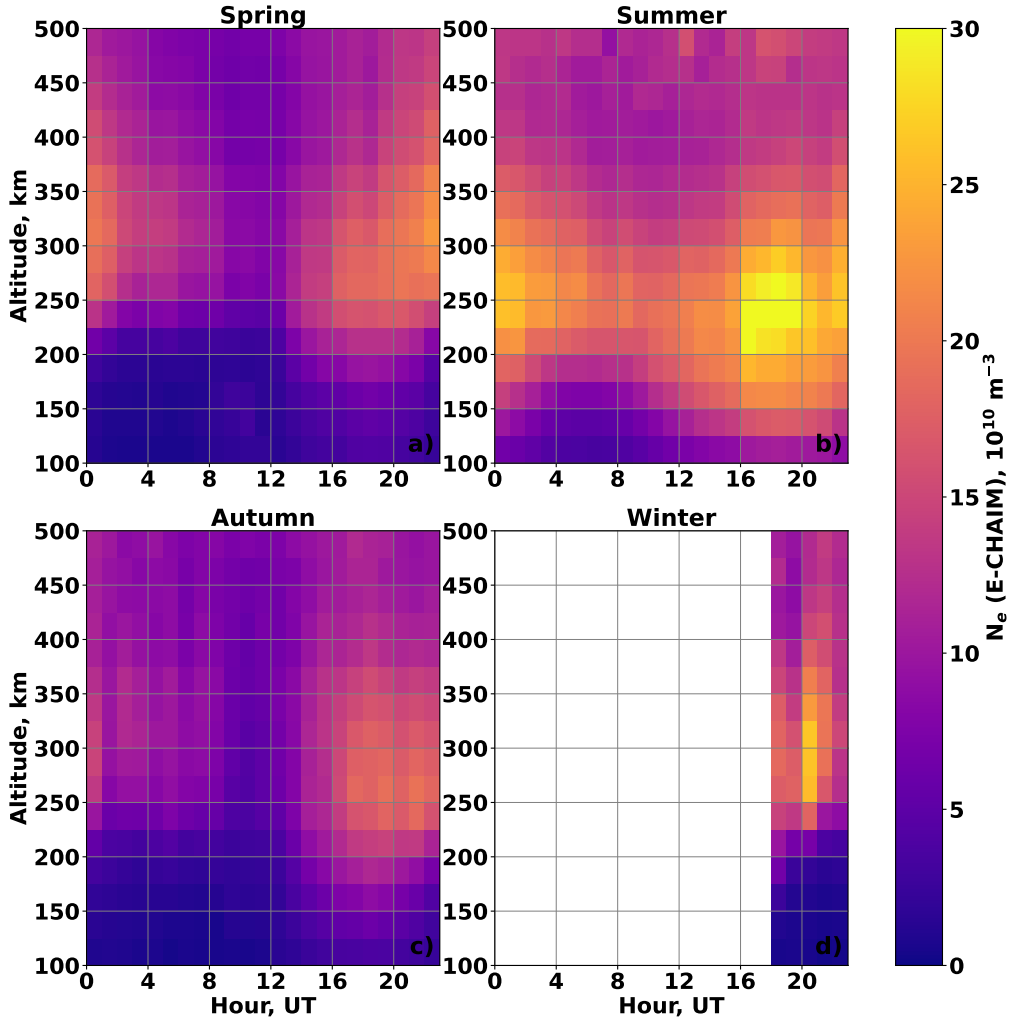

Figure 5.2: Electron density distribution in the ionosphere over Resolute Bay according to RISR-C observations in 2016-2018. Presented are hourly median values of Ne in 25-km height bins.

Nighttime Profiles

Considering the nighttime sector (03-09 UT) first, it can be seen that the night-time electron density is largest in the summer and lowest during the equinoxes. These results are consistent with CADI data on N_mF2 (Koustov et al., 2019). Unfortunately, no data were available for the nighttime during the winter season. The larger electron density values in the summer season correlates well with the increased sunlight hours in the High Arctic in the summer, which is expected from Chapman theory. Comparing the density between the equinoxes, the density during the autumn equinox is lower than the density during the spring equinox. Comparing the altitude bins with the highest density median in the summer with the same bins in the equinoxes, it can be seen that the peak density shifts higher from ~250 km in the summer to ~300 km in the equinoxes.

Daytime to Dusk Profiles

When considering the daytime (noon is 18 UT) profiles, electron density is the lowest in the autumn and highest in the summer. Comparing between seasons, the spring and winter electron density maxima are comparable to the autumn maximum. The typical values for summer are (20-30)$\times 10^{10}$ m^{-3} and (10-20)$\times 10^{10}$ m^{-3} for autumn. The largest electron density values are in the afternoon time sector. The afternoon enhancement persists until late dusk in the spring and summer seasons. In both the spring and winter seasons the density profile shifts higher at noon, that is, the maximum shifts to a higher altitude, see Figure 5.2a,d.

Dawn time Profiles

When considering the dawn time, 9-12 UT in particular, electron density profiles in Figure 5.2 it can be seen that the profiles are generally flat regardless of season. The dawn time sector is the period of lowest density for the equinoctial seasons. Additionally, no clear maxima emerge in the spring and autumn seasons. However, a dawn maximum can be seen in the summer in the 225-325 km altitudes.

Topside Electron Density

When considering the topside electron density at higher heights of 400-450 km, which was of interest in Chapter 4, the data showed less variance than at the F region peak. One observation that can be made is that both equinoctial seasons show an increase in electron density in the day and afternoon time sectors (Figure 5.2a,c).

5.3 Comparison of RISR-C data and E-CHAIM model output

Before presenting the results of comparing RISR-C and E-CHAIM, it is useful to describe the data handling used. The same dataset as described in Section 5.2 was used for the work in this comparison. For data generated using E-CHAIM, the C implementation of version 3.21 of E-CHAIM was used with the precipitation, storm and D region flags set. The inputs for the model functions were time and date, as well as altitude.

Initially, a simple approach was taken. E-CHAIM supports calculating N_mF2 and h_mF2 directly from time and location. In this mode the precise location of Resolute Bay was used. The electron density profile, at set altitude intervals, was also utilized, again using the precise location of Resolute Bay. However, it was found that there are significant differences in some time sectors and a more sophisticated approach was also utilized, where an E-CHAIM electron density prediction was generated for each RISR-C range gate in the dataset. In this approach the model was passed the altitude, latitude and longitude center of each range gate.

5.3.1 Model-measurement comparison for the electron density peak

Using the simplistic approach, the first comparison of RISR-C and E-CHAIM was comparing N_mF2 and h_mF2 values, Figure 5.3. These two parameters are of interest because they are focal parameters in empirical models (Shubin, 2015). The peak for RISR-C was identified by finding the maximum density value under 400 km along each radar beam and taking the median value for each scan. The midpoint of the integration time of each scan was used when calculating N_mF2 and h_mF2 using E-CHAIM .

Figure 5.3a shows the distribution of comparisons between h_mF2 predicted by E-CHAIM versus h_mF2 determined from RISR-C measurements. Although there is significant spread in the distribution, the majority of the points are close to the line of perfect agreement. The distribution is asymmetric, and is stretched along the E-CHAIM axis towards 30×10^{10} m^{-3}, which presents as an upper limit of the model predictions.

Figure 5.3b, in turn, shows the comparison of h_mF2 between RISR-C and E-CHAIM. Similar to the comparison of N_mF2, the h_mF2 comparison is asymmetric with significant spread. The model again appears to have an upper limit, with h_mF2 limited to ~320 km by the model.

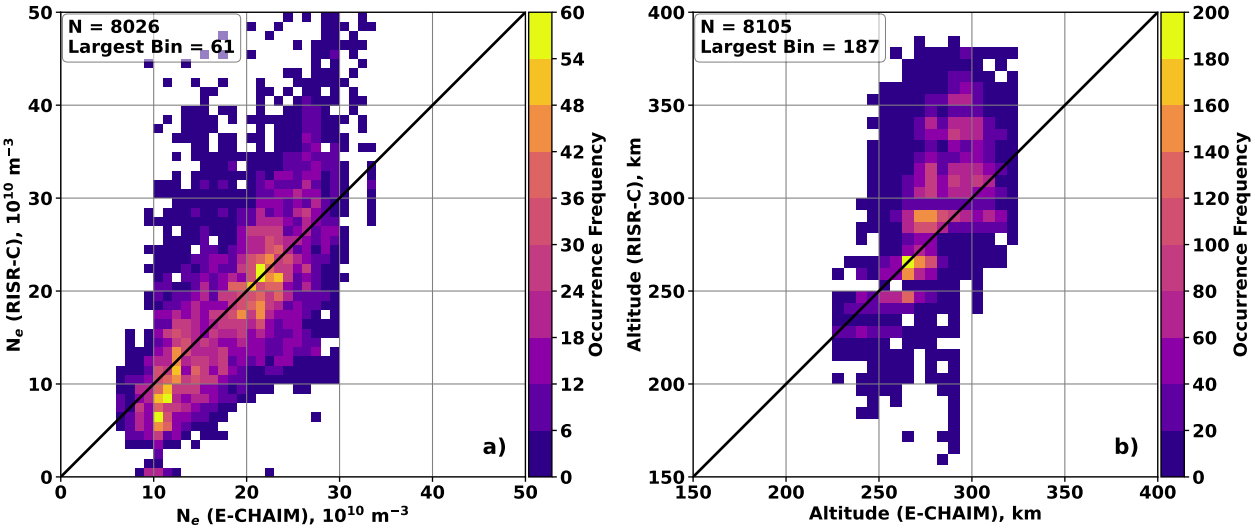

Figure 5.3: (a) Scatter plot of the peak electron density N_mF2 inferred from E-CHAIM model versus RISR-based peak electron density N_mF2 for matched moments. 5-min RISR-C data in the World Day mode of operation in 2016-2018 were considered. The total number of available points N is shown in the top left corner of each panel. The number of points in each pixel of the plot is coded according to the color bar to the right. (b) The same as (a) but for the height of the electron density maximum h_mF2.

5.3.2 Model-measurement comparison for various heights

Although peak density is a critical parameter for many space weather applications (Belehaki et al., 2015; Kutiev et al., 2013; Shubin, 2015), knowledge of the entire electron density profile is also useful in practical applications, for example, electron density profiles are useful for assessing propagation modes of HF radio waves. For this reason, comparisons of RISR-C and E-CHAIM were made at multiple altitudes. Figure 5.4 presents comparisons of observed electron density from RISR-C to predicted electron density from E-CHAIM at 200, 300 and 450 km altitudes, chosen to represent the bottomside, near peak F region and topside regions of the ionosphere. The plots supplement the information given in Chapter 3. Additionally, Figure 5.4c, at 450 km, is at the approximate altitude of the Swarm satellites A and C, and is relevant to Chapter 4.

From Figure 5.4a it can be seen that the bottom side electron density $N_{200}^{E-CHAIM}$ given by E-CHAIM is typically lower than electron density N_{200}^{RISR} measured by RISR-C. However, below densities of ~5×10^{10} m^{-3} the trend reverses and $N_{200}^{E-CHAIM}$ is greater than N_{200}^{RISR}. In the middle of the F region, E-CHAIM generally overestimates electron density compared to RISR-C, Figure 5.4b.

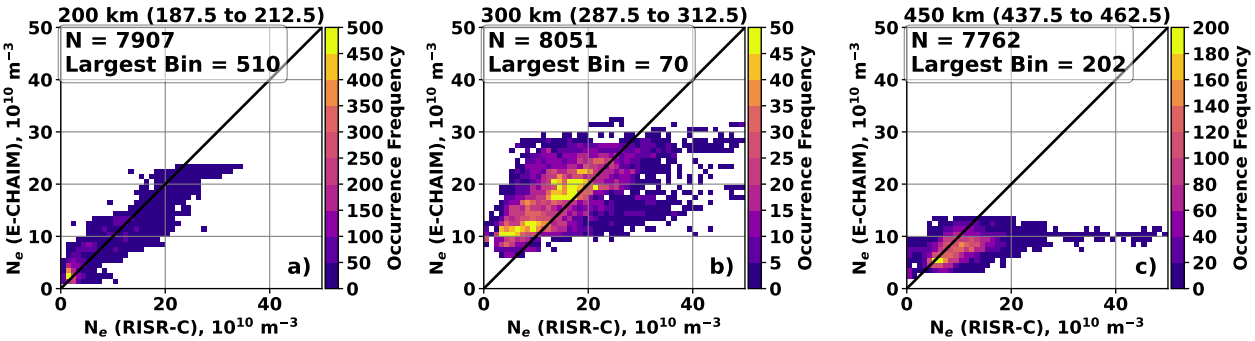

Figure 5.4: Scatter plot of the electron density inferred from E-CHAIM model versus RISR-based electron density for matched moments and heights. 5-min RISR-C data in the World Day mode of operation in 2016-2018 were considered. The number of points in each pixel of the plot is coded according to the color bar to the right. The total number of available points N is shown at the top left corner of each panel. (a), (b) and (c) are for the height of 200 km, 300 km and 450 km.

In the topside, Figure 5.4c, the same features as for the bottomside are observed, with even larger underestimation by E-CHAIM for large RISR-C densities greater than 10×10^{10} m^{-3}. Additional analysis showed the transition between the F region overestimation and bottomside/topside underestimation occurring at ~225 km and at ~400 km (Appendix A, Figure A.1).

From Figures 5.3 and 5.4 it can be concluded that, in general, E-CHAIM electron density profiles have higher density peaks at lower altitudes than the peaks observed in RISR-C data. However, these results are general, for a combined dataset and make no allowance for time of day or seasonal variability, which is addressed in the following section.

5.3.3 Diurnal and seasonal changes in the ratio predicted-to-measured electron densities at various heights

Moving on from the simple approach used to compare N_mF2 and h_mF2, the more sophisticated approach of calculating E-CHAIM density values at every RISR-C measurement in the dataset was used to investigate the differences between E-CHAIM and RISR-C. The ratio $R_{p/m}= N^{E-CHAIM}/N^{RISR}$ was calculated for every range-gate. The dataset was separated into seasons and the ratios in each season were then binned by hour and by 25 km altitude intervals, with the result plotted in Figure 5.5. The seasons were defined as in Section 5.2.

Overall, reasonable agreement between E-CHAIM and RISR-C can be concluded from Figure 5.5. A ratio of 0.5 to 1.5, shown in Figure 5.5 as violet to dull orange, dominates the results. Nevertheless, some regions show poor agreement, which are discussed separately for each season. When considering Figure 5.5 it is worth noting that higher altitudes have

5-7 times fewer points, in part due to large error bars in the RISR-C data at those heights (Chapter 2).

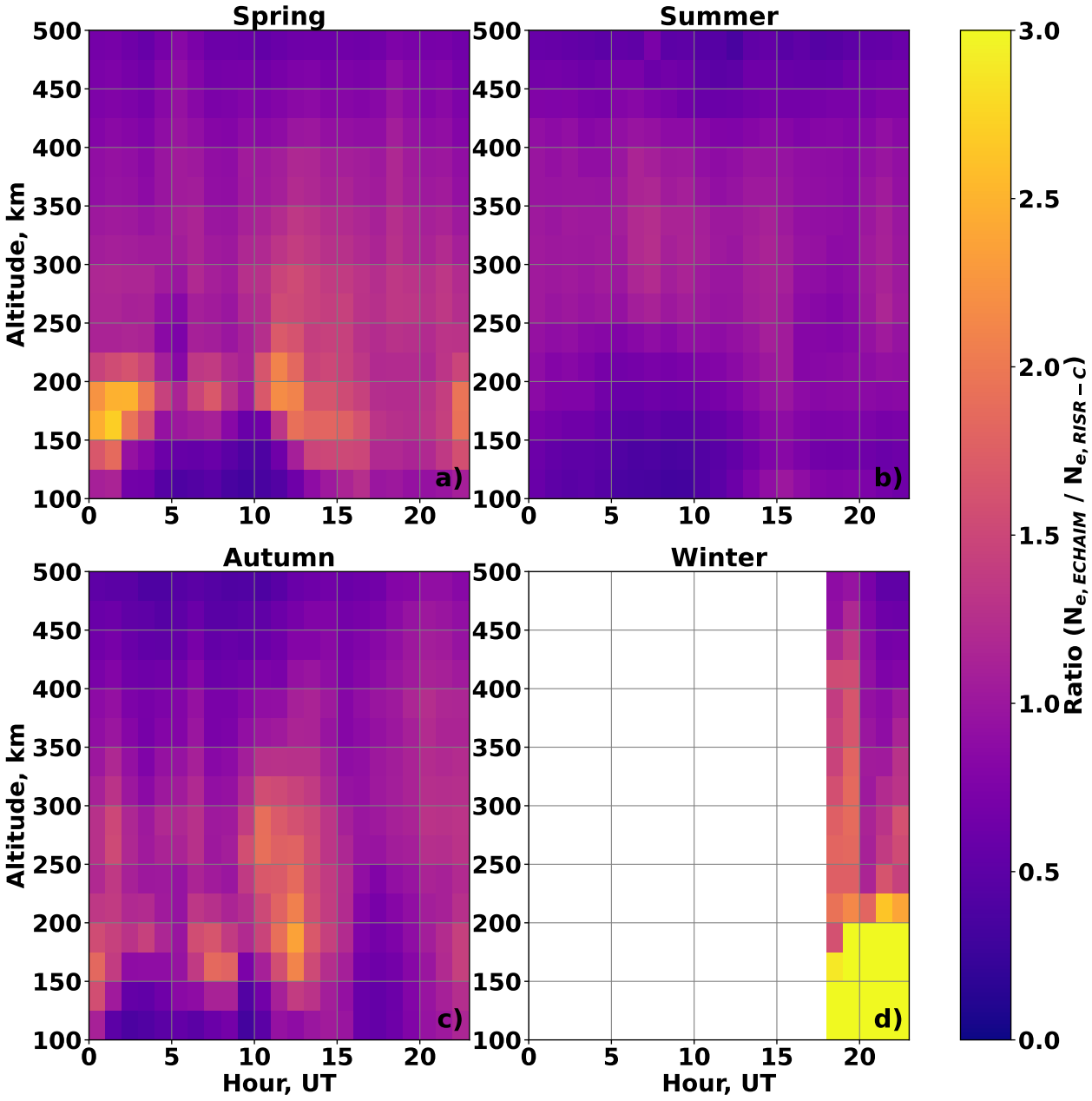

Figure 5.5: The ratio of E-CHAIM predicted to RISR measured electron density for all events available in 2016-2018. The data have been binned according to season, as indicated.

For the spring, Figure 5.5, the ratio $R_{p/m}$ for altitudes below 250 km is generally above 2.0 and rises at lower altitudes. An exception is the dawn time sector, between 7 and 14 UT. This shows underestimation of electron density by E-CHAIM in the lower ionosphere, particularly below 200 km. In the autumn, Figure 5.5c, large differences are evident at dusk

(~18 UT), near midnight (6 UT) and at dawn (12 UT), the latter showing the largest ratios. The summer, Figure 5.5b, shows good agreement, with $R_{p/m}$ close to 1 for all hours and altitudes. The model underestimates, i.e. ratios below 1.0, electron density between midnight and dawn under 200 km altitude.

The winter season shows the largest ratios, Figure 5.5d, with the ratio particularly bad below 200 km. Above 200 km the ratios are large but below 200 km they reach 3.0 or greater. These poor results must be considered with some caution. Referring back to Figure 5.1, it can be see that the winter seasons has the lowest quantity of data, with only a small number of measurements made in January 2016. Below 150 km the numbers per bin are exceptionally low, such that this anomaly could be related to statistical problems.

While Figure 5.5 provides a good qualitative view of the comparison between RISR-C and E-CHAIM, a more qualitative assessment was attempted. Figure 5.6 shows histogram distributions of $R_{p/m}$ for each season at three altitude ranges. Again the data were separated by region of the ionosphere, the bottom covering from 100 to 175 km altitude, the middle spanning 175 to 425 km altitude, and the top covering 425 to 500 km altitude.

Several conclusions can be made from Figure 5.6. Considering the bottom side first, the ratios are close to 1 for both spring and autumn, Figure 5.6a,g. In the summer E-CHAIM underestimates the electron density , while in the winter it significantly overestimates it, subplots d and j respectively. For the middle ionosphere, the middle column of Figure 5.6, E-CHAIM performs well with the ratio for all season centered near 1.0. In the winter the model underestimates slightly. However, the tails of the distribution for both spring and winter show noticeable overestimation. Considering the topside, the right column, the overall trend is underestimation for all seasons, with the distributions centered around a $R_{p/m}$ value of 0.6 to 0.7.

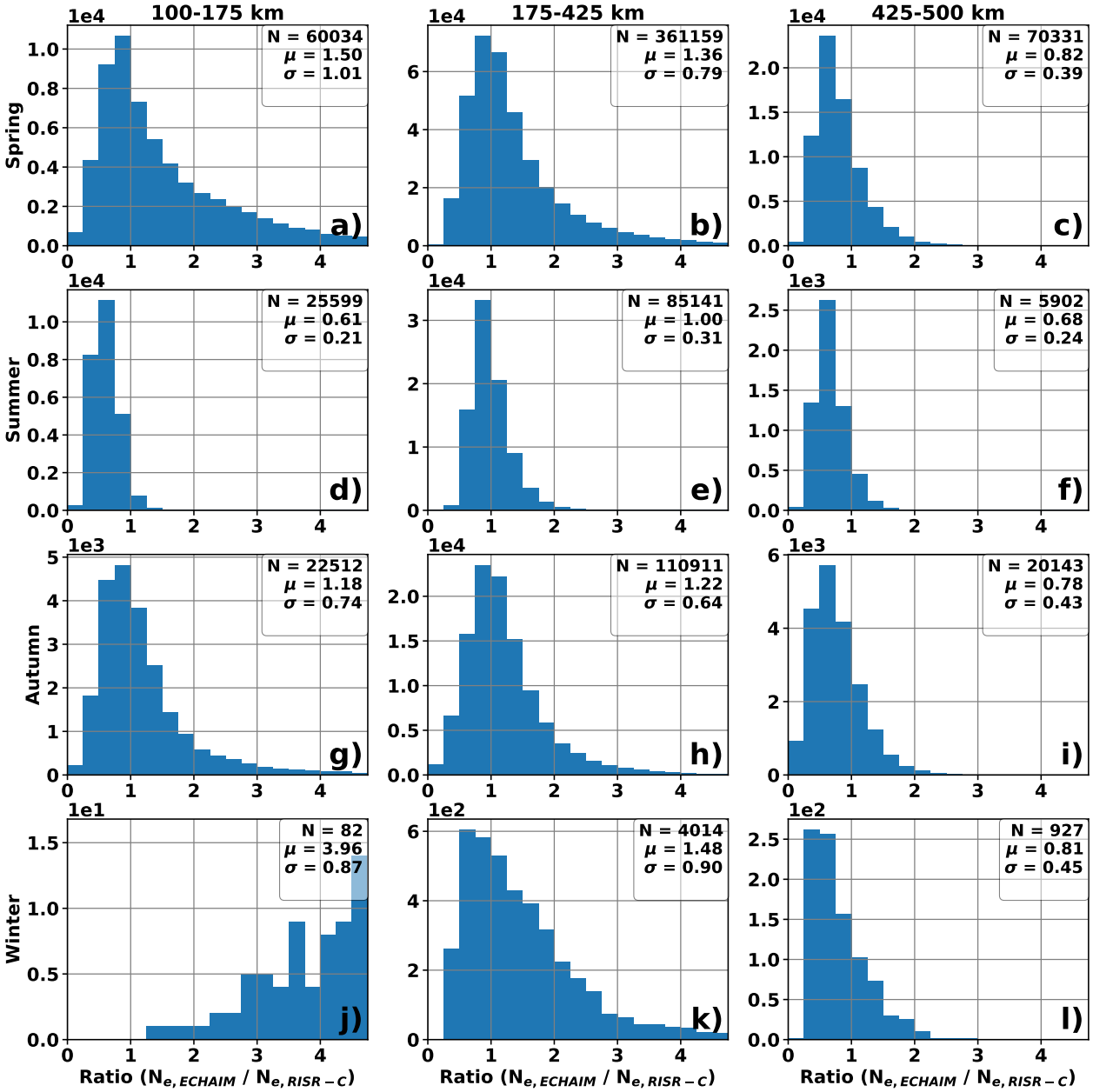

Figure 5.6: Histogram distributions for the ratio of E-CHAIM predicted to RISR measured electron density at three different ranges of heights and for four seasons. Each histogram is characterized by the median value (μ) and the standard deviation value (σ), reported in the upper right corner. Also presented is the number of points N for each distribution.

5.4 Discussion of the results

The performance of E-CHAIM has been assessed by the model developers in the past, as mentioned above and in Chapter 1. These comparisons mostly relied on ionosonde data not utilized for the development of the model. The original model-measurement comparisons

were limited in terms of data coverage. For example, in assessing N_mF2 only a single week of data was considered by Themens et al. (2018) for his Figure 8.3. When assessing the critical frequency f_0F2, the differences between between monthly median was found to be on the order of 0.5 MHz. This can be estimated as a 10% difference from the background critical frequency, which is a difference of 20% in terms of electron density. Temporal variations were found to have a correlation of ~0.8, with a slope of linear fit of ~0.8 by Themens et al. (2018), as shown in his Figure 8.5. Themens et al. (2018) also found that the altitude h_mF2 calculated from the model was within ~15-20 km of the comparison measurements, with no bias. These initial validation studies demonstrate the success of E-CHAIM at predicting average N_mF2 and h_mF2.

More recent work by Themens, Jayachandran, and McCaffrey (2019) has been more extensive. Their study utilized in situ data from Defense Meteorological Satellite Program (DMSP) satellites operating at ~830 km and the Challenging Mini-satellite Payload (CHAMP) satellite operating between 350 and 400 km. The study compared seasonal and solar cycle trends against E-CHAIM in order to identify the time sectors when E-CHAIM predicts seasonal and diurnal trends. It was shown that there is good agreement between DMSP and E-CHAIM , and therefore E-CHAIM performs well at topside altitudes. At the approximate altitude of the F region peak, E-CHAIM was found to overestimate electron density as compared to data from CHAMP in the summer and the nighttime during the winter. E-CHAIM predicts an afternoon enhancement in electron density correctly, but again overestimates compared to electron density measured by CHAMP. It is important to note that all validation of E-CHAIM has involved average data, such as mean hourly or mean monthly values.

The work undertaken in this section differs from previous work by others, in that, except for the analysis of N_mF2 and h_mF2, the comparison was based on measurements from RISR-C with a time resolution of five minutes. E-CHAIM is a climatological model and, thus, comparison with five minute data may fail because E-CHAIM is not designed for that temporal scale. The results presented here support this reasoning, as the findings presented are not as successful as those presented by Themens, Jayachandran, and McCaffrey (2019).

Comparison of the peak values of N_mF2 and h_mF2 shows the model performs well in the range (20-30)$\times 10^{10}$ m^{-3}. As shown in Figure 5.3, larger peak densities are generally underestimated by E-CHAIM . Subsequent analysis showed similar results for the bottom and topsides, as presented in Figures 5.4 and 5.5.

For the densest region of the ionosphere, from 300-400 km, the model is in close agreement, that is with $R_{p/m}$ close to 1, with the electron density measured by RISR-C. This is explainable by considering that the model was constructed using large amounts of data from this region. Agreement is particularly clear for the summer and autumn seasons. In the winter, however,

large differences were found. Given the prevalence of polar cap patches in the winter, a transient feature that would not be expected to be present in a climatological model such as E-CHAIM, this poor agreement with five minute data from RISR-C is expected. In the topside of the ionosphere the ratio $R_{p/m}$ was ~0.7 for all seasons. This is somewhat inconsistent with (Themens, Jayachandran, & McCaffrey, 2019), who found good agreement between E-CHAIM and topside measurements.

The largest disagreement between electron density values modelled by E-CHAIM and those measured by RISR-C were found in the bottomside, with the worst results in the winter season. E-CHAIM predicted a significantly larger density for an extended period in the late afternoon/dusk (Figure 5.5d). This could be related to the model having a lower altitude for the F2 peak (Figure 5.4) compared to the peak altitude found in he RISR-C data.

It is worth noting that E-CHAIM was designed to follow seasonal and diurnal patterns. Over the past decade N_mF2 maximized during the equinoctial time periods. However, this changed in 2016, as shown by Koustov et al. (2019) in their Figure 4. Koustov et al. (2019) showed that larger densities were found in the summers of 2017-2017 instead (data for 2018 were not published). This effect was observed in both the pre-noon and late afternoon time periods, which is the only winter data used in this study. Considering the results and data limitations of both this study and Koustov et al. (2019), it is reasonable to conclude that validation of E-CHAIM needs a more comprehensive dataset.

In a study inspirational to this work, Bjoland et al. (2016) performed an analysis of the ratio between E-CHAIM and IRI in the polar cap region. They found ratios of up to 3 (overestimation by the model) for the bottomside ionosphere (Figure 3 Bjoland et al., 2016). This effect was most visible during all seasons of solar cycle 23. For E-CHAIM , this study found instead underestimation in the top and bottom sides, with the exception of the winter night time sector.

5.5 Summary and conclusions

This Chapter presented highly averaged electron density profiles from RISR-C at Resolute Bay, using data for 2016-2018, and described the seasonal and diurnal trends found therein. It was found that the maximum electron density at F region altitudes occurs in noon-afternoon of the summer. The ionosphere was found to be generally weaker at dawn, although this effect lessened in the summer.

Using the more advanced approach of generating an E-CHAIM electron density prediction for every RISR-C measurement used, a comparison of RISR-C and E-CHAIM was undertaken. From this it was shown that:

- For electron densities in the range of (10-25)$\times 10^{10}$ m^{-3}, E-CHAIM matches well with electron density values found in RISR-C measurements. At higher observed densities E-CHAIM was found to underestimate. E-CHAIM was found to predict the correct N_mF2 peak altitude when the RISR-C data showed a peak altitude in the 225-300 km range. Again, E-CHAIM underestimated the peak latitude if the RISR-C data showed an altitude above 300 km.

- For the middle ionosphere, near the F region peak, E-CHAIM was found to be in reasonable agreement with measurements. The ratio of predicted density to observed was mostly between 0.5 and 1.5, with 1.0 indicating perfect agreement. The best agreement was found in the summer.

- At the topside altitudes E-CHAIM was found to underestimate electron densities, particularly in the summer season.

- The comparison of the winter data showed worse agreement than for other seasons, with particularly poor agreement below 200 km altitude. The strongest overestimation was observed in the winter data. However, there was insufficient winter data, and definitive conclusions would require more data to be available.

- The spring and autumn comparisons showed good agreement, with some exceptions at low altitudes. In the spring, for altitudes below 200 km, E-CHAIM overestimated at dusk and dawn. In the autumn, E-CHAIM overestimated the dawn electron density values.

Chapter 6

Summary of the results, conclusions and suggestions for future work

This Thesis has addressed several issues related to the electron density distribution in the ionosphere at extreme high latitudes with an emphasis on the topside altitudes. New information on typical values and their variations was provided specifically for the region over Resolute Bay. Electron density measurements with the Swarm LP instruments in space and with the RISR incoherent scatter radars on the ground were considered. The purpose of this Chapter is to summarize the most interesting findings of the work undertaken and make suggestions for future research.

6.1 Summary

Here a brief summary of what has been accomplished in this thesis is provided by using plain language.

6.1.1 Differences of electron density measured by Swarm A and Swarm C

Two aspects of Swarm electron density observations were addressed first (Chapter 3). Because at the time of the beginning of this Thesis, there was not much published on the Swarm electron density measurements in the high-latitude ionosphere, the first task was to assess the reported densities with a focus on the Resolute Bay area where ground-based ISRs provided electron density height profiles.

First, the consistency of electron densities measured by the Swarm A and Swarm C satellites was investigated. It was natural to start with such a comparison. The plots of the electron density measured by these satellites at low and middle latitudes are very as shown in Figure 3 of Buchert et al. (2015), for example. As the satellites approach high

latitudes, variations of density become irregular and such consistency between the satellites is not obvious from standard plots. Making plots of the measured densities around Resolute Bay has revealed several interesting details.

Individual passes showed that the spatial variations are very consistent, with a Pearson correlation coefficient well above 0.9. However, occasionally no consistency was observed with Pearson coefficients as low as 0.3. An attempt was made to find a preferential year of the solar cycle, season and time of the day when strong inconsistencies occur.

To assess the long-term trends in data compatibility, Swarm A and Swarm C data for all the passes in each month in 2014-2018 were produced and a Pearson correlation coefficient was computed for each month. The conclusion was that there is no noticeable solar-cycle type variation in changes of the coefficient. The plots also showed that there are seasonal changes but the pattern of these changes was not obvious. At the beginning of the period studied (2014-2015) better correlation was found in the summer. However, in later years winter enhancements were seen instead.

To develop further insight into the data, a more sophisticated approach was undertaken. All the data in individual passes were split into groups by season, and the analysis was focused on passes roughly through local noon-midnight sectors. The idea behind this approach is that inconsistency in individual satellite measurements can be caused by the presence of polar cap patches which are more frequent on the nightside of the winter ionosphere.

Analysis showed only marginal support for these expectations. The reasons for this result are not clear. Perhaps the database is too limited. Visual inspection of the data showed that often the density variations are small but inconsistent between the satellites, resulting in small correlation coefficients. For other events, the variations were consistent but shifted in latitude, often by $\sim\frac{1}{2}$ of a degree latitude. The latter case is thought to occur when a satellite crosses a polar cap patch at an acute angle to its boundaries such that the two satellite pass through the patch at different locations.

The overall conclusion from the analysis of consistency between Swarm A and Swarm C measurements over Resolute Bay is that a more detailed approach is needed to understand the reasons for identified mismatches in the data. Although there are indicators of real gradients in plasma electron density at the heights of measurements, more probable causes have not been identified.

6.1.2 Assessing electron density variations and comparison with E-CHAIM

The second task, and one of the main objectives of this Thesis, was the assessment of long terms trends in the topside electron density over the Resolute Bay area as predicted by the E-CHAIM ionospheric model and as measured by the Langmuir probes onboard the Swarm satellites.

The data presented showed that both the model and observations show a decline in the electron density from maximum values in 2014 to minimum values in 2017-2018, for both Swarm A/C and Swarm B at heights of ~450 km and ~500 km, respectively. This is consistent with the overall trend reported for Swarm high-latitude measurements (cumulatively, at magnetic latitudes above 55°) by Chartier et al. (2018). The model showed a somewhat stronger decline of the electron density for the nighttime and dawn time sectors. This is mostly because the model predicts much larger densities, almost by a factor of 2, during high solar activity, in those time sectors. It is important to note that the variability of the measured values is quite high in 2014-2015. This is perhaps an indicator that the polar cap ionosphere is more patchy for stronger solar activity.

An important conclusion of the E-CHAIM/Swarm comparison is that the model expects larger densities than measured ones. The effect is on the order of 20-30% and it is stronger at high electron densities.

6.1.3 Swarm and RISR electron density comparison

Comparison of the electron density measured by the Swarm satellites and by the RISR radars at conjunction points (Chapter 4) showed, similarly to Lomidze et al. (2018), that the Swarm LPs show systematically smaller values than those measured by independent instruments. The underestimations are on average about 30-35%. This is stronger than the ~20% effect reported by Lomidze et al. (2018). The differences between Swarm and RISR were found to be more significant for observations in the night time and dawn ionosphere.

An important difference with the previous work is that a limited number of points were available for the large electron densities, more than 50×10^{10} m^{-3}. This is expected as the polar cap ionosphere is less dense. However, an increasing, nearly linear trend was identified with a slope of less than one, implying that at larger electron densities the Swarm/RISR differences would be larger in absolute units. This is not consistent with the results of Lomidze et al. (2018). Work with other high-latitude ISRs is highly desirable to resolve the identified differences.

Another interesting aspect of the trends reported in this thesis is that if the data by

Lomidze et al. (2018) are plotted in terms of the electron density rather than in terms of plasma frequency, the dependence would be non-linear and exhibit saturation at large values. The data are expected to be well described by the square root of the density function since the plasma frequency is proportional to the square of the electron density and Lomidze et al. (2018) reported a nearly linear dependence of Swarm density upon plasma frequency. The data presented in this Thesis shows a rather linear dependence.

The reasons for larger differences discovered in this Thesis and inferred trends with the electron density increase are not clear. More extensive comparisons are needed.

6.1.4 Validation of the E-CHAIM ionospheric model with RISR data

The E-CHAIM model predictions were compared with RISR-C data (Chapter 5). RISR electron density values at every height were matched with predictions of the E-CHAIM model for the exact location of each radar range-gate and the time of the scan. For a number of experiments in 2016-2018, a general judgment on the performance of the model was done. The amount of data available ranged from several hundred to several thousand points, depending on the height of comparison and season. The comparison is still limited and should be considered as a preliminary analysis. For quantitative assessment, the ratios of the model predicted to measured electron densities were computed, $R_{p/m}$.

It was concluded that for the ionospheric heights around the peak of the F2 layer, the differences between the model and observations are not large. The medians in the distributions for ratios were found to be in between 1.0 and 1.5 with larger values occurring because of the extended tails in the distributions, mostly in winter and spring. For the topside ionosphere, the values were found to be mostly ~0.8, indicating model underestimations. The effect is stronger in summer. For the bottomside ionosphere, the strongest model-observation differences were found for summer and winter, with the $R_{p/m}$ exceeding 2-3 in the winter. For the summer ionosphere, the $R_{p/m}$ values of ~0.6 were found, a consistent underestimation. It was noted that winter bottomside data are very limited and more data are needed.

6.2 Suggestions for future research

The work undertaken in this thesis has several potential expansions that are briefly identified here.

6.2.1 Further assessment work for Swarm LP instruments

One clear conclusion of this thesis is that more careful analysis of Swarm electron density data needs to be done for observations with very low ($<5\times10^{10}$ m^{-3}) and very high electron density in the topside ionosphere ($>50\times10^{10}$ m^{-3}). Although the data on low electron densities is simply a question of time, data for high electron density is unlikely to be achieved in the polar cap for the Resolute Bay location. This is because high densities can occur here only spontaneously, perhaps resulting from anomalously high dense plasma departure from the auroral zone ionosphere. In this view, the search for radar-Swarm conjunctions should be expanded by involving the auroral zone ISRs such as PFISR and EISCAT. Although data are available for downloading from the Madrigal data website, the quality of measurements at the heights 450-550 km is not known to the author.

The other important direction of future work is involving in the Swarm-RISR comparison for RISR Imaging mode data. Originally, it was thought that the WD mode of RISR operation would provide better chances for radar-satellite conjunctions because the radar beam locations are widespread around Resolute Bay as compared to focusing on high beam elevation measurements in the Imaging modes. Another advantage of the WD mode taken into account is that the radars routinely use long pulses (~50 km in length along the beam) allowing for a reasonably strong return signal even at the heights well above the F layer peak where the Swarm satellites fly. When Imaging data analysis began, it seemed that many ISR data being processed with 1-min resolution were noisy and the investigation turned toward the WD data. One of the possible methods to alleviate the problem is averaging of the 1-min data in multiple beams, implying a new round of analysis.

More recent preliminary comparisons of Swarm with 5-min and 1-min Imaging mode ISR data showed a stronger underestimation effect for all three Swarm satellites. This was not expected, although according to private communication by Dr. Ashton Reimer of the RISR operation team at Stanford Research Institute (USA), the RISR data with 1-min resolution may be affected by the reception of echo signals from satellites, along with scattering from thermal plasma fluctuations. The author of this Thesis was not aware of such a possibility, but the fact of occasionally strong differences between the Swarm and RISR electron densities deterred the author from further analysis of RISR data in Imaging modes. This work, however, is desirable as it might give some clues on the reasons for identified differences between the instruments.

An interesting and important issue dealt with in this Thesis is the shape of the electron density profiles in the topside ionosphere (Chapter 4). The RISR-C data considered indicated that for some periods the density rapidly decreases with height while for other periods it does

not. To some extent, the existence of noticeable electron density above 400-500 km could be due to the radar monitoring the ionosphere at lower latitudes (with highly slanted beams), closer to the auroral oval latitudes where the electron density is expected to be higher on average (Themens et al., 2017). Although this possibility was ignored in this Thesis, it could be a real effect. In this respect, it is interesting that the RISR-N data show stronger Swarm underestimation of the electron density, thus hinting of a possibility of the effect for the RISR-C data. One possible investigation is the consideration of only RISR beams with high elevation angles. This work can be done for the existing dataset and, more interestingly, in the future as more data are coming online.

It has been recently proposed to use Swarm electron density data for forecasting electron densities at the F region peak (Pignalberi et al., 2018). The method is based on knowledge of the electron density profile decay above the F region peak. The developed empirical method can be supplemented, and probably adjusted, by extensive analysis of individual electron density profiles measured by ISRs.

6.2.2 Detection of polar cap patches with two Swarm satellites

The analysis of Swarm A and Swarm C electron density data performed in Chapter 3 postulated that poor correlation between variations of the LP-based electron densities from the two satellites is due to their crossing of polar cap patch edges at acute angles. It is highly desirable to investigate whether this interpretation is correct. One alarming inconsistency is that polar cap patches as detected by Swarm with other algorithms see clear preferential occurrence in winter (Chartier et al., 2018). A number of events of joint Swarm-RISR radar observations of polar cap patches need to be identified. After the mapping of the electron density distribution based on RISR radar measurements in the Imaging mode, a correlation of patch edges with the Swarm A and Swarm C electron density mismatches could be established.

6.2.3 Study of long-term trends in the topside ionosphere

It is highly desirable to establish the occurrence of the winter anomaly effect in typical electron densities measured by the Swarm satellites. In this project, averaged electron densities can be obtained and compared. Chartier et al. (2018) considered Swarm measurements over the auroral zone and polar cap regions, above magnetic latitudes of 55°, and showed that no winter anomaly is seen and electron density is maximized at summer solstices, their Figure 4. However, there is a chance that the anomaly still occurs because SuperDARN ground scatter data do show the effect for the Saskatoon radar (Ullrich, 2021). Yasyukevich et al. (2018)

found the winter anomaly is related to solar activity, so a future study during a strong solar maximum is desirable.

6.2.4 Further validation work for the E-CHAIM ionospheric model

The validation work of the E-CHAIM ionospheric model can be expanded in several ways. Presented in Chapter 5, RISR/E-CHAIM data are limited in coverage. The data span can be extended by involving ISR measurements from the north facing RISR-N and other ISR locations. Of special interest are RISR-N experiments aimed specifically at studying the F region plasma. Data of such experiments are not freely available to the researchers worldwide but they can be obtained upon special requests.

It is desirable to perform model validation with RISR data in the Imaging mode. These data better characterize the average conditions in a small region around the zenith of the station and statistical noise in the data, unavoidable in World Day experiments, would be reduced. These data are freely available.

Concluding this chapter, and the thesis, the author would say that the work undertaken has led to improvement in general understanding of the electron density distribution over the Resolute Bay area but, clearly, more work needs to be done specific to this region to have a better ionosphere specification for Space Weather monitoring and forecasting.

References

Akasofu, S.-I. (2011). The scientific legacy of Sydney Chapman. *Eos, Transactions American Geophysical Union*, *92*, 281–282. https://doi.org/10.1029/2011EO340001

Alouette I and II - Canada.ca. (2020, June 4). Retrieved June 4, 2020, from https://www.asc-csa.gc.ca/eng/satellites/alouette.asp

André, D., Sofko, G. J., Baker, K., & MacDougall, J. (1998). SuperDARN interferometry: Meteor echoes and electron densities from groundscatter. *Journal of Geophysical Research: Space Physics*, *103*, 7003–7015. https://doi.org/10.1029/97JA02923

Aol, S., Buchert, S., & Jurua, E. (2020). Traits of sub-kilometre F-region irregularities as seen with the Swarm satellites. *Annales Geophysicae*, *38*, 243–261. https://doi.org/10.5194/angeo-38-243-2020

Bahcivan, H., Tsunoda, R., Nicolls, M., & Heinselman, C. (2010). Initial ionospheric observations made by the new resolute incoherent scatter radar and comparison to solar wind IMF. *Geophysical Research Letters*, *37*. https://doi.org/10.1029/2010GL043632

Bankole, P. O. (2019). *Study of the polar cap plasma flows with the Clyde River SuperDARN radar* (Master's thesis). University of Saskatchewan. http://hdl.handle.net/10388/11861

Belehaki, A., Tsagouri, I., Kutiev, I., Marinov, P., Zolesi, B., Pietrella, M., Themelis, K., Elias, P., & Tziotziou, K. (2015). The European Ionosonde Service: Nowcasting and forecasting ionospheric conditions over Europe for the ESA space situational awareness services. *J. Space Weather Space Clim.*, *5*, A25. https://doi.org/10.1051/swsc/2015026

Beynon, W. J. G., & Williams, P. J. S. (1978). Incoherent scatter of radio waves from the ionosphere. *Reports on Progress in Physics*, *41*, 909–955. https://doi.org/10.1088/0034-4885/41/6/003

Bhattarai, S., & Mishra, L. N. (2017). Theoretical study of spherical langmuir probe in maxwellian plasma. *International Journal of Physics*, *5*, 73–81. https://doi.org/10.12691/ijp-5-3-2

Bilitza, D. (2018). IRI the International Standard for the Ionosphere. *Advances in Radio Science*, *16*, 1–11. https://doi.org/10.5194/ars-16-1-2018

Bilitza, D., Altadill, D., Truhlik, V., Shubin, V., Galkin, I., Reinisch, B., & Huang, X. (2017). International Reference Ionosphere 2016: From ionospheric climate to real-time weather predictions. *Space Weather*, *15*, 418–429. https://doi.org/10.1002/2016SW001593

Bjoland, L. M., Belyey, V., Løvhaug, U. P., & La Hoz, C. (2016). An evaluation of international reference ionosphere electron density in the polar cap and cusp using EISCAT Svalbard radar measurements. *Annales Geophysicae*, *34*, 751–758. https://doi.org/10.5194/angeo-34-751-2016

Brekke, A. (2013). *Physics of the upper polar atmosphere* (2nd Edition). Springer.

Buchert, S., Zangerl, F., Sust, M., André, M., Eriksson, A., Wahlund, J.-E., & Opgenoorth, H. (2015). Swarm observations of equatorial electron densities and topside GPS track losses. *Geophysical Research Letters*, *42*, 2088–2092. https://doi.org/10.1002/2015GL063121

Building on the success of Alouette with ISIS I and II - Canada.ca. (2020, June 4). Retrieved June 4, 2020, from https://www.asc-csa.gc.ca/eng/satellites/isis.asp

Chapman, S. (1931). The absorption and dissociative or ionizing effect of monochromatic radiation in an atmosphere on a rotating Earth. *Proceedings of the Physical Society*, *43*, 26–45. https://doi.org/10.1088/0959-5309/43/1/305

Chartier, A. T., Mitchell, C. N., & Miller, E. S. (2018). Annual occurrence rates of ionospheric polar cap patches observed using Swarm. *Journal of Geophysical Research: Space Physics*, *123*, 2327–2335. https://doi.org/10.1002/2017JA024811

Chisham, G., Lester, M., Milan, S. E., Freeman, M. P., Bristow, W. A., Grocott, A., McWilliams, K. A., Ruohoniemi, J. M., Yeoman, T. K., Dyson, P. L., Greenwald, R. A., Kikuchi, T., Pinnock, M., Rash, J. P. S., Sato, N., Sofko, G. J., Villain, J.-P., & Walker, A. D. M. (2007). A decade of the Super Dual Auroral Radar Network

(SuperDARN): Scientific achievements, new techniques and future directions. *Surveys in Geophysics*, *28*, 33–109. https://doi.org/10.1007/s10712-007-9017-8

Coïsson, P., Radicella, S., Leitinger, R., & Nava, B. (2006). Topside electron density in IRI and NeQuick: Features and limitations. *Advances in Space Research*, *37*, 937–942. https://doi.org/10.1016/j.asr.2005.09.015

Danilov, A. (2021). Behavior of F2-layer parameters and solar activity indices in the 24th cycle. *Advances in Space Research*, *67*, 102–110. https://doi.org/10.1016/j.asr.2020.09.042

Davis, K. (1990). *Ionospheric radio* [Issue 31 of IEE electromagnetic waves series]. Peter Peregrinus Ltd.

Defense Mapping Agency. (1991). *Department of defense world geodetic system 1984: Its definition and relationships with local geodetic systems.* (2nd ed.). https://apps.dtic.mil/sti/citations/ADA280358

Diego, P., Bertello, I., Candidi, M., Mura, A., Vannaroni, G., & Badoni, D. (2017). Plasma and fields evaluation at the Chinese seismo-electromagnetic satellite for electric field detector measurements. *IEEE Access*, *5*, 3824–3833. https://doi.org/10.1109/ACCESS.2017.2674019

Ding, Z., Wu, J., Xu, Z., Xu, B., & Dai, L. (2018). The Qujing incoherent scatter radar: System description and preliminary measurements. *Earth, Planets and Space*, *70*, 87. https://doi.org/10.1186/s40623-018-0859-8

Donovan, E. (2016). *Dept. of physics and astronomy* [Data from the CEDAR Madrigal database]. https://w3id.org/cedar?experiment_list=experiments/2016/ras/05mar16a&file_list=ras160305.002.hdf5

EFI instrument - Swarm - ESA Earth Explorer Missions - Earth Online - ESA. (2020, April 23). Retrieved April 23, 2020, from https://earth.esa.int/web/guest/missions/esa-eo-missions/swarm/instruments/efi

ESA. (2020, June 8). ESA - Swarm trio becomes a quartet. Retrieved June 8, 2020, from https://www.esa.int/Applications/Observing_the_Earth/Swarm/Swarm_trio_becomes_a_quartet

Feldstein, Y. I. (2016). The discovery and the first studies of the auroral oval: A review. *Geomagnetism and Aeronomy*, *56*, 129–142. https://doi.org/10.1134/S0016793216020043

Friis-Christensen, E., Lühr, H., Knudsen, D., & Haagmans, R. (2008). Swarm – an Earth observation mission investigating geospace. *Advances in Space Research*, *41*, 210–216. https://doi.org/10.1016/j.asr.2006.10.008

Gillies, R. G., Hussey, G. C., Sofko, G. J., McWilliams, K. A., Fiori, R. A. D., Ponomarenko, P., & St.-Maurice, J.-P. (2009). Improvement of SuperDARN velocity measurements by estimating the index of refraction in the scattering region using interferometry. *Journal of Geophysical Research: Space Physics*, *114*. https://doi.org/10.1029/2008JA013967

Gillies, R. G., van Eyken, A., Spanswick, E., Nicolls, M., Kelly, J., Greffen, M., Knudsen, D., Connors, M., Schutzer, M., Valentic, T., Malone, M., Buonocore, J., St.-Maurice, J.-P., & Donovan, E. (2016). First observations from the RISR-C incoherent scatter radar. *Radio Science*, *51*, 1645–1659. https://doi.org/10.1002/2016RS006062

Goodwin, L. V., Iserhienrhien, B., Miles, D. M., Patra, S., van der Meeren, C., Buchert, S. C., Burchill, J. K., Clausen, L. B. N., Knudsen, D. J., McWilliams, K. A., & Moen, J. (2015). Swarm in situ observations of F region polar cap patches created by cusp precipitation. *Geophysical Research Letters*, *42*, 996–1003. https://doi.org/10.1002/2014GL062610

Hargreaves, J. K. (1992). *The solar-terrestrial environment*. Cambridge University Press. https://doi.org/10.1017/CBO9780511628924

Hocke, K., & Igarashi, K. (2002). Electron density in the F region derived from GPS/MET radio occultation data and comparison with IRI. *Earth, Planets and Space*, *54*, 947–954. https://doi.org/10.1186/BF03352442

Huang, H., Chen, Y., Liu, L., Le, H., & Wan, W. (2015). An empirical model of the topside plasma density around 600 km based on ROCSAT-1 and Hinotori observations. *Journal of Geophysical Research: Space Physics*, *120*, 4052–4063. https://doi.org/10.1002/2014JA020940

Hunsucker, R. D. (1991). *Radio techniques for probing the terrestrial ionosphere*. Springer-Verlag.

Jin, Y., Spicher, A., Xiong, C., Clausen, L. B. N., Kervalishvili, G., Stolle, C., & Miloch, W. J. (2019). Ionospheric plasma irregularities characterized by the Swarm satellites: Statistics at high latitudes. *Journal of Geophysical Research: Space Physics*, *124*, 1262–1282. https://doi.org/10.1029/2018JA026063

Kakinami, Y., Watanabe, S., & Oyama, K.-I. (2008). An empirical model of electron density in low latitude at 600 km obtained by Hinotori satellite. *Advances in Space Research*, *41*, 1495–1499. https://doi.org/10.1016/j.asr.2007.09.031

Kelley, M. C. (Ed.). (2009). *The Earth's ionosphere* (2nd ed.). Academic Press.

Kivelson, M. G., & Russell, C. T. (Eds.). (1995). *Introduction to space physics*. Cambridge University Press. https://doi.org/10.1017/9781139878296

Knudsen, D. J., Burchill, J. K., Buchert, S. C., Eriksson, A. I., Gill, R., Wahlund, J.-E., Åhlen, L., Smith, M., & Moffat, B. (2017). Thermal ion imagers and Langmuir probes in the Swarm electric field instruments. *Journal of Geophysical Research: Space Physics*, *122*, 2655–2673. https://doi.org/10.1002/2016JA022571

Koustov, A. V., Luciuk, M. R., Gillies, R. G., Ullrich, S., Larson, B., McWilliams, K. A., & Schmidt, M. T. (2020). Velocity of SuperDARN echoes at intermediate radar ranges. *Radio Science*, *55*. https://doi.org/10.1029/2020RS007142

Koustov, A. V., Ullrich, S., Ponomarenko, P. V., Nishitani, N., Marcucci, F. M., & Bristow, W. A. (2019). Occurrence of F region echoes for the polar cap SuperDARN radars. *Earth, Planets and Space*, *71*, 112. https://doi.org/10.1186/s40623-019-1092-9

Kutiev, I. S., Marinov, P. G., & Watanabe, S. (2006). Model of topside ionosphere scale height based on topside sounder data. *Advances in Space Research*, *37*, 943–950. https://doi.org/10.1016/j.asr.2005.11.021

Kutiev, I. S., Tsagouri, I., Perrone, L., Pancheva, D., Mukhtarov, P., Mikhailov, A., Lastovicka, J., Jakowski, N., Buresova, D., Blanch, E., Andonov, B., Altadill, D., Magdaleno, S., Parisi, M., & Miquel Torta, J. (2013). Solar activity impact on the Earth's upper atmosphere. *J. Space Weather Space Clim.*, *3*, A06. https://doi.org/10.1051/swsc/2013028

Larson, B., Koustov, A. V., Kouznetsov, A. F., Lomidze, L., Gillies, R. G., & Reimer, A. S. (2021). A comparison of the topside electron density measured by the Swarm satellites and incoherent scatter radars over Resolute Bay, Canada. *Radio Science*, *56*. https://doi.org/https://doi.org/10.1029/2021RS007326

Laštovička, J. (2017). A review of recent progress in trends in the upper atmosphere [Long-term changes and trends in the upper atmosphere]. *Journal of Atmospheric and Solar-Terrestrial Physics*, *163*, 2–13. https://doi.org/https://doi.org/10.1016/j.jastp.2017.03.009

Lebreton, J.-P., Stverak, S., Travnicek, P., Maksimovic, M., Klinge, D., Merikallio, S., Lagoutte, D., Poirier, B., Blelly, P.-L., Kozacek, Z., & Salaquarda, M. (2006). The ISL Langmuir probe experiment processing onboard DEMETER: Scientific objectives, description and first results. *Planetary and Space Science*, *54*, 472–486. https://doi.org/10.1016/j.pss.2005.10.017

Lee, J., Min, K., Ham, J., Kim, H., Lee, J.-J., & Hong, S. (2013). Langmuir probe experiments on Korean satellites. *Current Applied Physics*, *13*, 846–849. https://doi.org/10.1016/j.cap.2012.12.011

Lomidze, L., Knudsen, D. J., Burchill, J., Kouznetsov, A., & Buchert, S. C. (2018). Calibration and validation of Swarm plasma densities and electron temperatures using ground-based radars and satellite radio occultation measurements. *Radio Science*, *53*, 15–36. https://doi.org/10.1002/2017RS006415

Markwardt, C. B. (2009). Non-linear Least-squares Fitting in IDL with MPFIT. In D. A. Bohlender, D. Durand, & P. Dowler (Eds.), *Astronomical data analysis software and systems xviii* (p. 251).

McNamara, L. F., Cooke, D. L., Valladares, C. E., & Reinisch, B. W. (2007). Comparison of CHAMP and Digisonde plasma frequencies at Jicamarca, Peru. *Radio Science*, *42*. https://doi.org/https://doi.org/10.1029/2006RS003491

Merlino, R. L. (2007). Understanding Langmuir probe current-voltage characteristics. *American Journal of Physics*, *75*, 1078–1085. https://doi.org/10.1119/1.2772282

Mission overview - ESA EO missions - Earth Online - ESA. (2020, May 25). Retrieved May 25, 2020, from https://earth.esa.int/web/guest/missions/esa-eo-missions/swarm/mission-overview

Moen, J., Gulbrandsen, N., Lorentzen, D. A., & Carlson, H. C. (2007). On the MLT distribution of F region polar cap patches at night. *Geophysical Research Letters*, *34*. https://doi.org/10.1029/2007GL029632

Moré, J. J. (1978). The Levenberg-Marquardt algorithm: Implementation and theory. In G. A. Watson (Ed.), *Numerical analysis* (pp. 105–116). Springer Berlin Heidelberg.

Mott-Smith, H. M., & Langmuir, I. (1926). The theory of collectors in gaseous discharges. *Phys. Rev.*, *28*, 727–763. https://doi.org/10.1103/PhysRev.28.727

National Research Council (U.S.) (2013). *Solar and space physics: A science for a technological society*. The National Academies Press. https://doi.org/10.17226/13060

Nava, B., Coïsson, P., & Radicella, S. (2008). A new version of the NeQuick ionosphere electron density model. *Journal of Atmospheric and Solar-Terrestrial Physics*, *70*, 1856–1862. https://doi.org/10.1016/j.jastp.2008.01.015

Nishitani, N., Ruohoniemi, J. M., Lester, M., Baker, J. B. H., Koustov, A. V., Shepherd, S. G., Chisham, G., Hori, T., Thomas, E. G., Makarevich, R. A., Marchaudon, A., Ponomarenko, P., Wild, J. A., Milan, S. E., Bristow, W. A., Devlin, J., Miller, E., Greenwald, R. A., Ogawa, T., & Kikuchi, T. (2019). Review of the accomplishments of mid-latitude Super Dual Auroral Radar Network (SuperDARN) HF radars. *Progress in Earth and Planetary Science*, *6*, 27. https://doi.org/10.1186/s40645-019-0270-5

Oyama, K.-I., & Hirao, K. (1976). Inaccuracies in electron density estimates due to surface contamination of Langmuir probes. *Planetary and Space Science*, *24*, 87–89. https://doi.org/https://doi.org/10.1016/0032-0633(76)90065-9

Papon, J., Cohen, M., Cotts, B., & Haque, N. (2010). Ionospheric Morphology. Retrieved October 26, 2021, from https://web.archive.org/web/20100726230749/http://nova.stanford.edu/~vlf/IHY_Test/Tutorials/TheIonosphere/IonosphericMorphology.pdf

Pignalberi, A., Pezzopane, M., & Rizzi, R. (2018). Modeling the lower part of the topside ionospheric vertical electron density profile over the European region by means

of Swarm satellites data and IRI UP method. *Space Weather*, *16*, 304–320. https://doi.org/10.1002/2017SW001790

Pignalberi, A., Pezzopane, M., Themens, D. R., Haralambous, H., Nava, B., & Coïsson, P. (2020). On the analytical description of the topside ionosphere by NeQuick: Modeling the scale height through COSMIC/FORMOSAT-3 selected data. *IEEE Journal of Selected Topics in Applied Earth Observations and Remote Sensing*, *13*, 1867–1878. https://doi.org/10.1109/JSTARS.2020.2986683

Pirjola, R., Viljanen, A., Pulkkinen, A., & Amm, O. (2000). Space weather risk in power systems and pipelines. *Physics and Chemistry of the Earth, Part C: Solar, Terrestrial & Planetary Science*, *25*, 333–337. https://doi.org/https://doi.org/10.1016/S1464-1917(00)00027-1

Ponomarenko, P. V., Koustov, A. V., St.-Maurice, J.-P., & Wiid, J. (2011). Monitoring the F-region peak electron density using HF backscatter interferometry. *Geophysical Research Letters*, *38*. https://doi.org/https://doi.org/10.1029/2011GL049675

Preliminary EFI LP data release notes. (2018, September 24). *Swedish Institute of Space Physics*. Retrieved May 27, 2020, from https://earth.esa.int/documents/10174/1514862/swarm-level-1B-plasma-processor-algorithm.pdf

Rawer, K. (2013). *Wave propagation in the ionosphere, developments in electromagnetic theory and applications*. Springer Science; Business Media.

Resendiz Lira, P. A., & Marchand, R. (2021). Simulation inference of plasma parameters from Langmuir probe measurements. *Earth and Space Science*, *8*, e2020EA001344. https://doi.org/10.1029/2020EA001344

RISR information. (2016, September 14). Retrieved June 4, 2020, from http://data.phys.ucalgary.ca/sort_by_project/RISR-C/documentation/RISR_information.pdf

Rousseeuw, P. J., & Croux, C. (1993). Alternatives to the median absolute deviation. *Journal of the American Statistical Association*, *88*, 1273–1283. https://doi.org/10.2307/2291267

Samaniego, J. I., Yeo, L. H., & Wang, X. (2020). A double hemispherical probe for characterizing and minimizing the self-wake effects on probe measurements. *Journal of Geophysical Research: Space Physics*, *125*. https://doi.org/10.1029/2020JA028508

Schunk, R. W., & Nagy, A. (2009). *Ionospheres : Physics, plasma physics, and chemistry* (2nd ed.). New York : Cambridge University Press.

Semeter, J., Butler, T., Heinselman, C., Nicolls, M., Kelly, J., & Hampton, D. (2009). Volumetric imaging of the auroral ionosphere: Initial results from PFISR. *Journal of Atmospheric and Solar-Terrestrial Physics*, *71*, 738–743. https://doi.org/10.1016/j.jastp.2008.08.014

Shaikh, M. M., Nava, B., & Haralambous, H. (2018). On the use of topside RO-derived electron density for model validation. *Journal of Geophysical Research: Space Physics*, *123*, 3943–3954. https://doi.org/https://doi.org/10.1029/2017JA025132

Shepherd, S. G. (2014). Altitude-adjusted corrected geomagnetic coordinates: Definition and functional approximations. *Journal of Geophysical Research: Space Physics*, *119*, 7501–7521. https://doi.org/https://doi.org/10.1002/2014JA020264

Shubin, V. (2015). Global median model of the f2-layer peak height based on ionospheric radio-occultation and ground-based digisonde observations. *Advances in Space Research*, *56*, 916–928. https://doi.org/10.1016/j.asr.2015.05.029

Siefring, C. L., Amatucci, W. E., & Rodriguez, P. (1998). Fast electron temperature measurements with langmuir probes: Considerations for space flight and initial laboratory tests. *Measurement techniques in space plasmas: Particles* (pp. 55–60). American Geophysical Union (AGU). https://doi.org/10.1029/GM102p0055

Spicher, A., Cameron, T., Grono, E. M., Yakymenko, K. N., Buchert, S. C., Clausen, L. B. N., Knudsen, D. J., McWilliams, K. A., & Moen, J. I. (2015). Observation of polar cap patches and calculation of gradient drift instability growth times: A Swarm case study. *Geophysical Research Letters*, *42*, 201–206. https://doi.org/10.1002/2014GL062590

Swarm Phase C/D - Swarm L1b product definition. (2019, May 6). *National Space Institute Technical University of Denmark*. Retrieved August 8, 2019, from https://earth.esa.int/documents/10174/1514862/Swarm%5C_L1b%5C_Product%5C_Definition

Swarm preliminary plasma dataset user note. (2015, May 13). *European Space Agency*. Retrieved May 27, 2020, from https://earth.esa.int/documents/10174/1514862/Swarm_Preliminary_Plasma_Dataset_User_Note

Themens, D. R. (2018). *Modeling electron density at high latitudes: Development of the Empirical Canadian High Arctic Ionospheric Model (E-CHAIM)* (Doctoral dissertation). University of New Brunswick. https://unbscholar.lib.unb.ca/islandora/object/unbscholar%3A9319

Themens, D. R., Jayachandran, P. T., Bilitza, D., Erickson, P. J., Häggström, I., Lyashenko, M. V., Reid, B., Varney, R. H., & Pustovalova, L. (2018). Topside electron density representations for middle and high latitudes: A topside parameterization for E-CHAIM based on the NeQuick. *Journal of Geophysical Research: Space Physics*, *123*, 1603–1617. https://doi.org/10.1002/2017JA024817

Themens, D. R., Jayachandran, P. T., Galkin, I., & Hall, C. (2017). The Empirical Canadian High Arctic Ionospheric Model (E-CHAIM): NmF2 and hmF2. *Journal of Geophysical Research: Space Physics*, *122*, 9015–9031. https://doi.org/10.1002/2017JA024398

Themens, D. R., Jayachandran, P. T., & McCaffrey, A. M. (2019). Validating the performance of the Empirical Canadian High Arctic Ionospheric Model (E-CHAIM) with in situ observations from DMSP and CHAMP. *J. Space Weather Space Clim.*, *9*, A21. https://doi.org/10.1051/swsc/2019021

Themens, D. R., Jayachandran, P. T., McCaffrey, A. M., Reid, B., & Varney, R. H. (2019). A bottomside parameterization for the Empirical Canadian High Arctic Ionospheric Model. *Radio Science*, *54*, 397–414. https://doi.org/10.1029/2018RS006748

Themens, D. R., Jayachandran, P. T., Nicolls, M. J., & MacDougall, J. W. (2014). A top to bottom evaluation of IRI 2007 within the polar cap. *Journal of Geophysical Research: Space Physics*, *119*, 6689–6703. https://doi.org/10.1002/2014JA020052

Themens, D. R., Reid, B., Jayachandran, P. T., Larson, B., Koustov, A. V., Elvidge, S., McCaffrey, A. M., & Watson, C. (2021). E-CHAIM as a model of total electron content: Performance and diagnostics. *Space Weather*, *19*, e2021SW002872. https://doi.org/https://doi.org/10.1029/2021SW002872

Torr, M. R., & Torr, D. (1973). The seasonal behaviour of the F2-layer of the ionosphere. *Journal of Atmospheric and Terrestrial Physics*, *35*, 2237–2251. https://doi.org/10.1016/0021-9169(73)90140-2

Ullrich, S. (2021). *Trends in occurrence of polar cap SuperDARN echoes and electron density variations in the ionosphere* (Master's thesis). University of Saskatchewan. http://hdl.handle.net/10388/13253

van den IJssel, J., Encarnação, J., Doornbos, E., & Visser, P. (2015). Precise science orbits for the Swarm satellite constellation. *Advances in Space Research*, *56*, 1042–1055. https://doi.org/10.1016/j.asr.2015.06.002

Virmont, J., & Godard, R. (1972). Spherical Langmuir probe: Complements to the 'classical' theory. *Plasma Physics*, *14*, 793–803. https://doi.org/10.1088/0032-1028/14/8/004

Wiltberger, M., Merkin, V., Zhang, B., Toffoletto, F., Oppenheim, M., Wang, W., Lyon, J. G., Liu, J., Dimant, Y., Sitnov, M. I., & Stephens, G. K. (2017). Effects of electrojet turbulence on a magnetosphere-ionosphere simulation of a geomagnetic storm. *Journal of Geophysical Research: Space Physics*, *122*, 5008–5027. https://doi.org/10.1002/2016JA023700

Wissing, J. M., Kallenrode, M.-B., Kieser, J., Schmidt, H., Rietveld, M. T., Strømme, A., & Erickson, P. J. (2011). Atmospheric Ionization Module Osnabrück (AIMOS): 3. comparison of electron density simulations by AIMOS-HAMMONIA and incoherent scatter radar measurements. *Journal of Geophysical Research: Space Physics*, *116*. https://doi.org/10.1029/2010JA016300

Yasyukevich, Y. V., Yasyukevich, A. S., Ratovsky, K. G., Klimenko, M. V., Klimenko, V. V., & Chirik, N. V. (2018). Winter anomaly in NmF2 and TEC: When and where it can occur. *J. Space Weather Space Clim.*, *8*, A45. https://doi.org/10.1051/swsc/2018036

Yau, A. W., & James, H. G. (2015). CASSIOPE Enhanced Polar Outflow Probe (e-POP) mission overview. *Space Science Reviews*, *189*, 3–14. https://doi.org/10.1007/s11214-015-0135-1

York, D., Evensen, N. M., Martińez, M. L., & De Basabe Delgado, J. (2004). Unified equations for the slope, intercept, and standard errors of the best straight line. *American Journal of Physics*, *72*, 367–375. https://doi.org/10.1119/1.1632486

Zou, L., Rishbeth, H., Müller-Wodarg, I. C. F., Aylward, A. D., Millward, G. H., Fuller-Rowell, T. J., Idenden, D. W., & Moffett, R. J. (2000). Annual and semiannual variations in the ionospheric F2-layer. I. Modelling. *Annales Geophysicae*, *18*, 927–944. https://doi.org/10.1007/s00585-000-0927-8

Appendix A

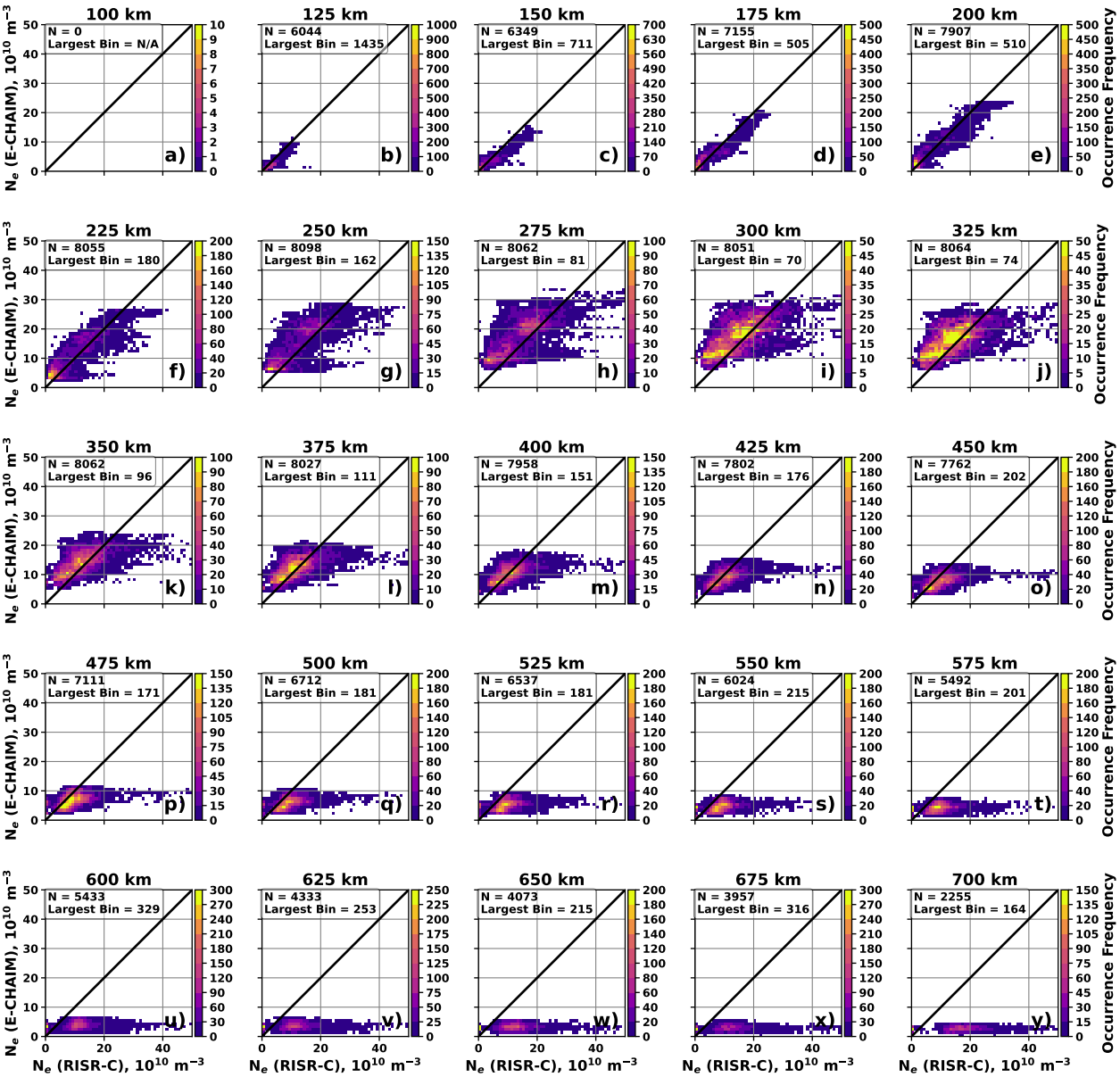

Figure A.1: Scatter plot of the electron density inferred from E-CHAIM model versus RISR-based electron density for matched moments and heights. 5-min RISR-C data in the World Day mode of operation in 2016-2018 were considered. The number of points in each pixel of the plot is coded according to the color bar to the right. The total number of available points N is shown at the top left corner of each panel.

Appendix B

Rights to Chapter 4

JOHN WILEY AND SONS LICENSE
TERMS AND CONDITIONS

Dec 16, 2021

This Agreement between Mr. Bion Larson ("You") and John Wiley and Sons ("John Wiley and Sons") consists of your license details and the terms and conditions provided by John Wiley and Sons and Copyright Clearance Center.

License Number	5210891398789
License date	Dec 16, 2021
Licensed Content Publisher	John Wiley and Sons
Licensed Content Publication	Radio Science
Licensed Content Title	A Comparison of the Topside Electron Density Measured by the Swarm Satellites and Incoherent Scatter Radars Over Resolute Bay, Canada
Licensed Content Author	B. Larson, A. V. Koustov, A. F. Kouznetsov, et al

Licensed Content Date	Oct 27, 2021
Licensed Content Volume	56
Licensed Content Issue	11
Licensed Content Pages	16
Type of use	Dissertation/Thesis
Requestor type	Author of this Wiley article
Format	Print and electronic
Portion	Full article
Will you be translating?	No
Title	Comparative study of polar-cap electron density using Swarm, RISR and E-CHAIM
Institution name	University of Saskatchewan

Expected presentation date	Jan 2022
Order reference number	0002
Requestor Location	Mr. Bion Larson Box 98 Love, SK S0J1P0 Canada Attn: Mr. Bion Larson
Publisher Tax ID	EU826007151
Total	0.00 CAD

Terms and Conditions

TERMS AND CONDITIONS

This copyrighted material is owned by or exclusively licensed to John Wiley & Sons, Inc. or one of its group companies (each a"Wiley Company") or handled on behalf of a society with which a Wiley Company has exclusive publishing rights in relation to a particular work (collectively "WILEY"). By clicking "accept" in connection with completing this licensing transaction, you agree that the following terms and conditions apply to this transaction (along with the billing and payment terms and conditions established by the Copyright Clearance Center Inc., ("CCC's Billing and Payment terms and conditions"), at the

time that you opened your RightsLink account (these are available at any time at http://myaccount.copyright.com).

Terms and Conditions

- The materials you have requested permission to reproduce or reuse (the "Wiley Materials") are protected by copyright.

- You are hereby granted a personal, non-exclusive, non-sub licensable (on a stand-alone basis), non-transferable, worldwide, limited license to reproduce the Wiley Materials for the purpose specified in the licensing process. This license, **and any CONTENT (PDF or image file) purchased as part of your order,** is for a one-time use only and limited to any maximum distribution number specified in the license. The first instance of republication or reuse granted by this license must be completed within two years of the date of the grant of this license (although copies prepared before the end date may be distributed thereafter). The Wiley Materials shall not be used in any other manner or for any other purpose, beyond what is granted in the license. Permission is granted subject to an appropriate acknowledgement given to the author, title of the material/book/journal and the publisher. You shall also duplicate the copyright notice that appears in the Wiley publication in your use of the Wiley Material. Permission is also granted on the understanding that nowhere in the text is a previously published source acknowledged for all or part of this Wiley Material. Any third party content is expressly excluded from this permission.

- With respect to the Wiley Materials, all rights are reserved. Except as expressly granted by the terms of the license, no part of the Wiley Materials may be copied, modified, adapted (except for minor reformatting required by the new Publication), translated, reproduced, transferred or distributed, in any form or by any means, and no derivative works may be made based on the Wiley Materials without the prior permission of the respective copyright owner.**For STM Signatory Publishers clearing permission under the terms of the STM Permissions Guidelines only, the terms of the license are extended to include subsequent editions and for editions in other languages, provided such editions are for the work as a whole in situ and does not involve the separate exploitation of the permitted figures or extracts,** You may not alter, remove or

suppress in any manner any copyright, trademark or other notices displayed by the Wiley Materials. You may not license, rent, sell, loan, lease, pledge, offer as security, transfer or assign the Wiley Materials on a stand-alone basis, or any of the rights granted to you hereunder to any other person.

- The Wiley Materials and all of the intellectual property rights therein shall at all times remain the exclusive property of John Wiley & Sons Inc, the Wiley Companies, or their respective licensors, and your interest therein is only that of having possession of and the right to reproduce the Wiley Materials pursuant to Section 2 herein during the continuance of this Agreement. You agree that you own no right, title or interest in or to the Wiley Materials or any of the intellectual property rights therein. You shall have no rights hereunder other than the license as provided for above in Section 2. No right, license or interest to any trademark, trade name, service mark or other branding ("Marks") of WILEY or its licensors is granted hereunder, and you agree that you shall not assert any such right, license or interest with respect thereto

- NEITHER WILEY NOR ITS LICENSORS MAKES ANY WARRANTY OR REPRESENTATION OF ANY KIND TO YOU OR ANY THIRD PARTY, EXPRESS, IMPLIED OR STATUTORY, WITH RESPECT TO THE MATERIALS OR THE ACCURACY OF ANY INFORMATION CONTAINED IN THE MATERIALS, INCLUDING, WITHOUT LIMITATION, ANY IMPLIED WARRANTY OF MERCHANTABILITY, ACCURACY, SATISFACTORY QUALITY, FITNESS FOR A PARTICULAR PURPOSE, USABILITY, INTEGRATION OR NON-INFRINGEMENT AND ALL SUCH WARRANTIES ARE HEREBY EXCLUDED BY WILEY AND ITS LICENSORS AND WAIVED BY YOU.

- WILEY shall have the right to terminate this Agreement immediately upon breach of this Agreement by you.

- You shall indemnify, defend and hold harmless WILEY, its Licensors and their respective directors, officers, agents and employees, from and against any actual or threatened claims, demands, causes of action or proceedings arising from any breach of this Agreement by you.

- IN NO EVENT SHALL WILEY OR ITS LICENSORS BE LIABLE TO YOU OR ANY OTHER PARTY OR ANY OTHER PERSON OR ENTITY FOR ANY SPECIAL, CONSEQUENTIAL, INCIDENTAL, INDIRECT, EXEMPLARY OR PUNITIVE DAMAGES, HOWEVER CAUSED, ARISING OUT OF OR IN CONNECTION WITH THE DOWNLOADING, PROVISIONING, VIEWING OR USE OF THE MATERIALS REGARDLESS OF THE FORM OF ACTION, WHETHER FOR BREACH OF CONTRACT, BREACH OF WARRANTY, TORT, NEGLIGENCE, INFRINGEMENT OR OTHERWISE (INCLUDING, WITHOUT LIMITATION, DAMAGES BASED ON LOSS OF PROFITS, DATA, FILES, USE, BUSINESS OPPORTUNITY OR CLAIMS OF THIRD PARTIES), AND WHETHER OR NOT THE PARTY HAS BEEN ADVISED OF THE POSSIBILITY OF SUCH DAMAGES. THIS LIMITATION SHALL APPLY NOTWITHSTANDING ANY FAILURE OF ESSENTIAL PURPOSE OF ANY LIMITED REMEDY PROVIDED HEREIN.

- Should any provision of this Agreement be held by a court of competent jurisdiction to be illegal, invalid, or unenforceable, that provision shall be deemed amended to achieve as nearly as possible the same economic effect as the original provision, and the legality, validity and enforceability of the remaining provisions of this Agreement shall not be affected or impaired thereby.

- The failure of either party to enforce any term or condition of this Agreement shall not constitute a waiver of either party's right to enforce each and every term and condition of this Agreement. No breach under this agreement shall be deemed waived or excused by either party unless such waiver or consent is in writing signed by the party granting such waiver or consent. The waiver by or consent of a party to a breach of any provision of this Agreement shall not operate or be construed as a waiver of or consent to any other or subsequent breach by such other party.

- This Agreement may not be assigned (including by operation of law or otherwise) by you without WILEY's prior written consent.

- Any fee required for this permission shall be non-refundable after thirty (30) days from receipt by the CCC.

- These terms and conditions together with CCC's Billing and Payment terms and conditions (which are incorporated herein) form the entire agreement between you and WILEY concerning this licensing transaction and (in the absence of fraud) supersedes all prior agreements and representations of the parties, oral or written. This Agreement may not be amended except in writing signed by both parties. This Agreement shall be binding upon and inure to the benefit of the parties' successors, legal representatives, and authorized assigns.

- In the event of any conflict between your obligations established by these terms and conditions and those established by CCC's Billing and Payment terms and conditions, these terms and conditions shall prevail.

- WILEY expressly reserves all rights not specifically granted in the combination of (i) the license details provided by you and accepted in the course of this licensing transaction, (ii) these terms and conditions and (iii) CCC's Billing and Payment terms and conditions.

- This Agreement will be void if the Type of Use, Format, Circulation, or Requestor Type was misrepresented during the licensing process.

- This Agreement shall be governed by and construed in accordance with the laws of the State of New York, USA, without regards to such state's conflict of law rules. Any legal action, suit or proceeding arising out of or relating to these Terms and Conditions or the breach thereof shall be instituted in a court of competent jurisdiction in New York County in the State of New York in the United States of America and each party hereby consents and submits to the personal jurisdiction of such court, waives any objection to venue in such court and consents to service of process by registered or certified mail, return receipt requested, at the last known address of such party.

WILEY OPEN ACCESS TERMS AND CONDITIONS

Wiley Publishes Open Access Articles in fully Open Access Journals and in Subscription journals offering Online Open. Although most of the fully Open Access journals publish open access articles under the terms of the Creative Commons Attribution (CC BY) License only, the subscription

journals and a few of the Open Access Journals offer a choice of Creative Commons Licenses. The license type is clearly identified on the article.

The Creative Commons Attribution License

The Creative Commons Attribution License (CC-BY) allows users to copy, distribute and transmit an article, adapt the article and make commercial use of the article. The CC-BY license permits commercial and non-

Creative Commons Attribution Non-Commercial License

The Creative Commons Attribution Non-Commercial (CC-BY-NC)License permits use, distribution and reproduction in any medium, provided the original work is properly cited and is not used for commercial purposes.(see below)

Creative Commons Attribution-Non-Commercial-NoDerivs License

The Creative Commons Attribution Non-Commercial-NoDerivs License (CC-BY-NC-ND) permits use, distribution and reproduction in any medium, provided the original work is properly cited, is not used for commercial purposes and no modifications or adaptations are made. (see below)

Use by commercial "for-profit" organizations

Use of Wiley Open Access articles for commercial, promotional, or marketing purposes requires further explicit permission from Wiley and will be subject to a fee.

Further details can be found on Wiley Online Library
http://olabout.wiley.com/WileyCDA/Section/id-410895.html

Other Terms and Conditions:

v1.10 Last updated September 2015